UNIVERSIDADE DE LISBOA

FACULDADE DE CIÊNCIAS

DEPARTAMENTO DE FÍSICA

Characterising Solar System planets' atmosphere using cloud tracking wind velocities retrieval method

Mestrado em Física

Especialização em Astrofísica e Cosmologia

José Eduardo Oliveira Silva

Dissertação orientada por:

Pedro Mota Machado

2017

Acknowledgments

This master's thesis, even though is subject to a particular thematic (namely planetary sciences and astrophysics) is the culmination of all my endeavours since I first arrived to college (and Lisbon) from a small town in the middle of Portugal. I must say it has been quite a ride since those days, and in just 5 years I feel like I learned a lot and I hope this is just the start of a bigger and more fulfilling life.

But I could not have gotten this far without any support and throughout these years, it has been huge. First of all I would like to thank my parents António Manuel Carvalho Silva and Maria José Garcez Pereira Oliveira for giving me so many opportunities to chase my dreams and showing me what the world has to offer, all the while guiding me through life's many obstacles. Their solid and caring education made me the young man I am today and I have always tried my best to deserve such priviledge and make them proud.

During my bachelor's I quickly realised how important it is to work hard if you want to achieve your goals but it took me a while to understand that those goals only matter if you are happy all the way through and that life is not only meant to be spent working, even if it is something you enjoy. For that I will always thank my brother João Pedro Oliveira Silva, for being a constant humane presence in my life, and that has helped me become a more caring and considerate person, even if I fight him at every step. I also thank him for daring me into believe in my own abilities and strengths when all I see, at times, are my weakest points. He makes me feel strong and confident whenever I drown in doubts.

I will always thank my dear friends Pedro Mendes, Francisco Guerreiro, Bernardo Alegria, David Oliveira, Marta Silva, João Peixoto and Duarte Valente for all their support, the way they helped me grow up and their constant challenge for me to become a better person for which I am truly grateful. I hope I also contributed somehow into their lives and that our relationships can last. I shall certainly see that they will.

And last but not least, I am grateful to my supervisor Pedro Mota Machado, which has taught me (and still does) from day one, what it means to be a scientist. I could not ask for a better person to guide me in my infancy as an astrophysicist, for his love for science, for his seriousness in his work and for how many doors he has already opened for me at such an early stage in my career. I also acknowledge the support from everyone who works in IA (Institute of Astrophysics and Space Sciences) for making me feel at home while I work and for being a nursery for interesting people and ideias. It truly has been an amazing experience to share my love for space sciences with everyone here and I hope that I can continue working here and give back to IA so that we might grow even bigger as a team of scientists and particularly our own planetary sciences group.

Abstract

Complete general circulation models for planetary atmospheres are one of the cornerstones of atmosphere dynamics in planetary sciences. These models take a great amount of observations for them to be accurate enough to properly describe circulation on our targets and also the possibility of application to other new worlds outside our solar system.

The bulk of this thesis reports the use of a cutting-edge, semi-automatic cloud tracking technique with a specifically designed software (Hueso, R. et al., 2010), that allows the retrieval of wind velocities on various targets of our solar system, namely Venus, Jupiter and Saturn. With data from Venus Express VMC (Venus Monitoring Camera) (Markiewicz, W.J. et al., 2007) and VIRTIS (Visual and Infrared Thermal Imaging Spectrometer) instruments for Venus, a zonal wind profile was retrieved for the cloud tops (67-70 km) with UV observations (Sanchez-Lavega, A., et al., 2008; Limaye, S.S., 2007; Peralta, J., et al., 2007) and on the base of the clouds (45-48 km) with IR observations also focusing on the south polar vortex. To study the zonal wind profile of Jupiter and Saturn, data from Cassini ISS (Imaging Science Subsystem) (Knowles, B., 2016) was used for cloud tracking on both global images of the planets but also on smaller, localized atmospheric features like the *Great Red Spot* storm system on Jupiter and the *North Polar Hexagon* and vortex on Saturn.

Some complementary work was carried out regarding the detection and characterisation of atmospheric gravity waves on Venus with VMC (Piccialli, A. et al., 2014) and VIRTIS (Peralta, J., et al., 2008) instruments, which is part of a continuous effort for a systematic study of these features whose role on Venus' atmosphere dynamics is yet to be fully understood.

I also present an introduction to SPICE, a planetary image navigation programming system widely used by the scientific community, stating its main uses and an example of the power of this tool. This is part of an effort to learn how to properly work with this system and is still a work in progress.

Keywords: Venus, Jupiter, Saturn, Cloud-Tracking, Zonal Winds, *Great Red Spot*, Vortex, Atmospheric Gravity Waves, Image Navigation.

Resumo

Embora tenhamos todos a mesma origem, os planetas do sistema solar evoluíram todos de forma bastante distinta, criando um palco de estudo de ambientes bastante diversificados num lugar bastante acessível do Universo. Dentro dos planetas que possuem uma atmosfera estável, o comportamento dinâmico de cada um é especialmente singular.

Vénus é, à primeira vista um planeta bastante semelhante à Terra, tendo origens semelhantes e dimensões, densidades, massas, composições químicas e distância ao Sol muito próximas, no entanto as condições que se verificam à superfície dos dois planetas são bastantes díspares. Ao passo que na Terra testemunhamos condições ideais para a existência de vida, na superfície de Vénus assistimos a temperaturas que podem ultrapassar os 460°C, uma pressão atmosférica 90 vezes mais intensa que na Terra ao nível do mar (próximo à pressão a 1 km de profundidade no oceano) e nuvens de ácido sulfúrico. Estes aspectos devem-se, em grande parte ao papel da atmosfera de Vénus, em particular o efeito de estufa descontrolado que se verifica, responsável pelas temperaturas altíssimas à superfície tanto no lado diurno como no lado nocturno, sendo portanto um caso extremo das alterações climáticas no nosso planeta.

Outro aspecto importante da atmosfera de Vénus é que esta está em regime de super-rotação em volta do globo terrestre pois o gás envolvente percorre todo o globo em cerca de 4.4 dias enquanto que o período de rotação da superfície rochosa é mais longo que o ano venusiano, indo até aos 243 dias. Os ventos na região equatorial podem chegar a velocidades superiores a 100 m/s ($>$ 360 km/h). Estes valores de velocidade podem ser calculados através da observação do deslocamento de padrões de nuvens em imagens sucessivas através da técnica de seguimento de nuvens abordada nesta dissertação, sendo possível obter perfis latitudinais do vento zonal (ventos com direcções paralelas ao equador). Com imagens obtidas através dos instrumentos VMC e VIRTIS a bordo da sonda Venus Express da Agência Espacial Europeia (ESA) o topo (57-70 km de altitude) e a base da camada de nuvens em Vénus foram observados a comprimentos de onda que rondam o ultravioleta próximo e no infravermelho respectivamente, bem como o vórtice polar no hemisfério sul também no infravermelho. Com ambos os instrumentos foram ainda detectadas e caracterizadas ondas atmosféricas de gravidade em ambos os níveis da camada de nuvens, fazendo parte de um estudo sistemático no seguimento dos trabalhos realizados em (Peralta, J., et al., 2008) e (Piccialli, A. et al., 2014).

Júpiter e Saturno são mundos completamente diferentes da realidade que estamos habituados num planeta rochoso. Estes são compostos maioritariamente por gases (hidrogénio e hélio) e uma pequena percentagem para todos os outros elementos da tabela periódica a que chamamos de 'metais' e são bastante maiores que os planetas telúricos (por exemplo o diâmetro de Júpiter perfaz mais de 11 Terras alinhadas) o que lhes confere massas bastante superiores às dos planetas rochosos.

Sendo gigantes gasosos, a noção de superfície para estes corpos torna-se algo bastante difuso, pois à medida que descemos para maiores profundidades nestes planetas, a temperatura e pressão aumentam significativamente, levando os gases a estados físicos mais exóticos (como o *hidrogénio*

metálico). No entanto, modelos científicos existentes (Irwin, 2009; Ingersol, A.P et al., 2004) mostram que as alterações de temperatura e pressão são graduais e que as transições de estado físico também devem ocorrer de forma gradual no interior dos planetas gasosos, pelo que é plausível que uma superfície clássica rochosa não exista a não ser somente no núcleo do planeta cuja existência ainda não foi confirmada.

Na "superfície"observável de ambos os planetas, principalmente em Júpiter é possível verificar a forte dinâmica atmosférica, com bandas latitudinais a fluir em direcções opostas a grande velocidade (dado o período de rotação dos planetas de aproximadamente 10h e vários mecanismos de geração de energia que alimentam a atmosfera) que no caso de Saturno chegam mesmo acima dos 400 m/s (1440 km/h). Para além destes, movimentos turbulentos complexos e sistemas de tempestades colossais que podem viver até vários anos são uma realidade constante nos gigantes gasosos. De facto, a famosa *Grande Mancha Vermelha* tem mais de 150 anos.

Com dados do instrumento ISS (Imaging Science Subsystem) da sonda Cassini, foi possível obter imagens globais a vários comprimentos de onda, dos dois planetas por forma a aplicar o mesmo método de seguimento de nuvens já usado para Vénus e obter perfis latitudinais completos do vento zonal ao nível das nuvens de Júpiter e Saturno (camada de nuvens ao nível de pressão próximo dos 0.7 bar). Dada a elevada resolução dos dados obtidos por este instrumento, também foi possível estudar fenómenos locais em ambos os corpos como a já mencionada *Grande Mancha Vermelha*, a estrutura hexagonal na região polar e o vórtice no hemisfério norte de Saturno, sendo obtidas as velocidades dos ventos nestas regiões.

As imagens de Vénus captadas pelo instrumento VIRTIS e seleccionadas neste trabalho foram obtidas directamente através dos arquivos públicos PSA (Planetary Science Archive) da ESA da missão Venus Express. As restantes imagens usados foram providenciadas pelo orientador (Pedro Machado), no entanto todas as imagens usadas já constam em arquivos públicos das diferentes missões. Imagens Cassini/ISS foram seleccionadas com auxílio da ferramenta PVOL (Planetary Virtua Observatory Laboratory) que permite uma pré-visualização da imagem e de várias informações sobre a mesma, incluindo filtros usados e a data da captura, o que é extremamente relevante para o seguimento de nuvens.

Após a selecção, de forma a que as imagens fossem úteis tanto para a detecção de ondas atmosféricas de gravidade como para a técnica de seguimento de nuvens, estas foram sujeitas a um processo de tratamento de imagem com a ajuda do PLIA (*Planetary Laboratory for Image Analysis*), um software fornecido ao nosso grupo pela equipa de ciências planetárias de Bilbau (Hueso, R. et al., 2010). O processo passa essencialmente pela tentativa de eliminação de artefactos e aberrações na imagem que dificultem a análise da mesma e por um aumento do contraste dos detalhes presentes na imagem. Para as imagens Cassini/ISS, o PLIA foi também essencial na navegação das mesmas, atribuindo coordenadas de latitude e longitude apropriadas, a cada pixel da imagem.

O método de seguimento de nuvens foi empregue com uma ferramenta auxiliar do PLIA, PICV2 (*Planetary Image Correlation Velocimetry*) que usa um algoritmo de correlação de imagem de forma a identificar padrões de nuvens contrastantes com o fundo que sejam similares dentro de um par de imagens. Com isso, o desfasamento em píxeis do padrão entre imagens é calculado e sabendo o intervalo de tempo entre as imagens, com as imagens navegadas, é possível calcular a velocidade do padrão de nuvens. Desta forma, vários vectores de ventos foram obtidos para os três alvos para produzir perfis latitudinais do vento zonal.

Destacam-se, no hemisfério sul de Vénus na base das nuvens (com observações no infravermelho, 1.74 μm e 2.3 μm) ventos que chegam aos 60 m/s (216 km/h) para médias e baixas latitudes e no topo das nuvens (observações no ultravioleta próximo, 360-400 nm e no visível a 540 nm) ventos que chegam acima dos 100 m/s ($>$ 360 km/h) também a médias e baixas latitudes. Para Júpiter, um perfil latitudinal do vento zonal de ambos os hemisférios foi recuperado com os ven-

tos na zona equatorial a atingir os 150 m/s (540 km/h) e ainda foi obtido um perfil de ventos na *Grande Mancha Vermelha* que mostra o fluxo do gás ao longo da tempestade. No caso de Saturno, o perfil de vento zonal obtido mostrou o jacto equatorial proeminente deste planeta, cujas velocidades podem atingir os 450 m/s (1620 km/h). Também foram recuperados os ventos na região polar do hemisfério norte com especial relevância para a dinâmica do hexágono e a sua vizinhança bem como o vórtice no pólo norte de Saturno.

Nesta dissertação também é abordada de forma resumida, um sistema de navegação de imagens planetárias chamado SPICE, sendo uma ferramenta desenvolvida pelo NAIF (*Navigation and Ancillary Information Facility*) da NASA, amplamente usada pela comunidade científica de ciências planetárias que oferece uma precisão sem precedentes na navegação planetária. O trabalho desenvolvido ao longo destes meses neste âmbito foi principalmente a aprendizagem da programação inerente a este sistema para posterior aplicação em imagens reais de sondas espaciais e também é apresentado um exemplo das aplicações de navegação SPICE.

Palavras-Chave: Vénus, Júpiter, Saturno, vento zonal, vórtice, ondas atmosféricas, navegação planetária.

Contents

List of Figures

List of Tables

Chapter 1

Introduction

1.1 Venus - Earth's Sister

Venus is often regarded as a "twin" planet of Earth. As with the other telluric planets, Earth and Venus were most likely formed from the same original "cloud" of gas and dust at approximately the same time. Both planets have similar densities, size, mass and bulk chemical composition (Svedhem et al., 2007). However, a closer look reveals where those similarities end and despite formation arguments that sustain equivalent initial atmospheric conditions for Venus and Earth, they evolved in drastically different ways (Grinspoon, 1997).

The motions of this planet outright show some of its peculiarities. Venus is the only planet in the solar system with retrograde rotation and has an axis tilt of 177°. This means that its rotational axis is almost perpendicular to the ecliptic albeit being inverted. As both hemispheres receive approximately the same amount of radiation throughout the year, seasons are thereby negligible (Bougher et al., 1997).

The atmosphere of Venus is extremely dense. The total mass of the atmosphere on Venus is close to 92 times the mass of Earths' gaseous envelopment, which leads to a surface atmospheric pressure that reaches 90 bar (90 times the atmospheric pressure on Earth or at about 1 km beneath the surface of the ocean). Along with surface temperatures that reach 735° K due to the inherent runaway greenhouse effect that takes place in the venusian atmosphere caused mainly by the massive concentration of CO_2 and a visual horizon that does not extend 400 meters in a truly deserted, yellowish world. Hence, thermodynamically speaking, the pressure and temperature at surface lead the atmospheric properties to be closer to the liquid phase than a gaseous one (Gonçalves, R., 2016).

1.1.1 Venus' Atmosphere

Composition

Even though all telluric planets must have shared a similar atmosphere at the very beginning of the solar system, their evolution pathways diverged significantly.

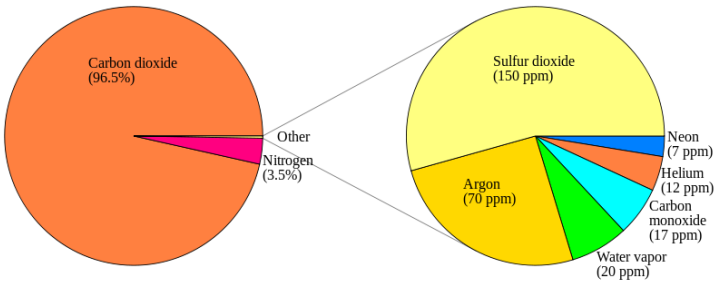

Figure 1.1.1: Venus atmosphere relative composition. Residual species' relative abundance are given on the magnified portion on the right side of this figure. From (Machado, P., 2013)

Carbon dioxide, which as stated earlier, is the dominant species in the venusian atmosphere (1.1.1) in contrast with Earth which has most of its CO_2 buried in the crust in the form of carbonated rocks and dissolved in the oceans. Interestingly, Venus' atmosphere and its runaway greenhouse effect makes it an extreme case study of the possible consequences of climate change on Earth, given today's problems of anthropogenic excess emission of greenhouse gases (Machado, P., 2013). SO_2 (sulphur dioxide), one of the minor components of the atmosphere has a significant role in the atmosphere/surface coupling and, along with other chemical species like carbon monoxide (CO) and in trace amounts H_2O contribute to cloud formation and composition. In fact, its high bond-albedo ($\sim$ 90 %) is probably related to the sulphuric acid (H_2SO_4) cloud layer that covers the entire globe which efficiently reflects most of the visible light emitted by the sun. So just as the Earth's atmosphere is primarily composed by N_2 (78%) and O_2 (20%) with water vapour as a condensable, in Venus, CO_2 dominates the atmosphere and H_2SO_4 acts as a condensable (Gonçalves, R., 2016).

Structure

The relationship between temperature, pressure and density in a planetary atmosphere is governed by a balance between gravity and pressure, represented in the *hydrostatic equilibrium* equation (Pater, I., Lissauer, J., 2007):

$$\frac{dP}{dz} = -g(z)\rho(z) \tag{1.1}$$

Where **P** is the air pressure, **g(z)** is the gravitational acceleration, $\rho(z)$ is the air density and **z** represents the altitude, relative to the surface of the planet.

All targets concerned in this thesis have their atmospheres in equilibrium and their equation of state can be well approximated by the *ideal gas law*:

$$P = NkT = \frac{\rho R_{gas} T}{\mu_a} = \frac{\rho k T}{\mu_a m_{au}} \tag{1.2}$$

where **N** is the particle number density, R_{gas} the universal gas constant, μ_a the mean molecular weight (in atomic mass units) and $m_{au} \approx 1.67 \times 10^{-24}$ the mass of an atomic weight unit, which is slightly less than the mass of a hydrogen atom (Pater, I., Lissauer, J., 2007) (p.58).

Using both the equations for hydrostatic equilibrium 1.1 and the ideal gas law 1.2, one can express the atmospheric pressure as function of altitude:

$$P(z) = P_0 e^{-\int_0^z dr/H(r)} \tag{1.3}$$

where **H(r)** is the scale height.

The vertical temperature profile divides the venusian atmosphere in three main layers:

– **Troposphere** (0-65 km): Extending from the surface to the top of the clouds and where the temperature decreases with altitude with the thermal gradient ratio of about 9 K·km^{-1} (close to the adiabatic lapse rate: $\Gamma_d = \frac{g}{C_p} = 7.39\ K \cdot km^{-1}$), which shows that convection is not significant in this region);

– **Mesosphere** (65-100 km) Characterized by a less pronounced vertical thermal gradient, but a relevant horizontal variability with latitude, increasing from the equator to the poles, which is consistent with the existence of a *hadley* circulation cell (Taylor et al., 1980);

– **Thermosphere** (100-200 km): A less dense environment subject to the ionizing radiation from the sun, day and night side thermal differences become significant as thermal conductivity is less efficient than on the lower layers. This brings a thermal asymmetry between the day and night hemispheres, as the day-time temperature tend to increase with altitude in the 100-140 km range, while on the night hemisphere it tends to decrease along the same altitude range. Above 140 km the temperature profiles at both hemispheres become isothermal(Machado, P., 2013).

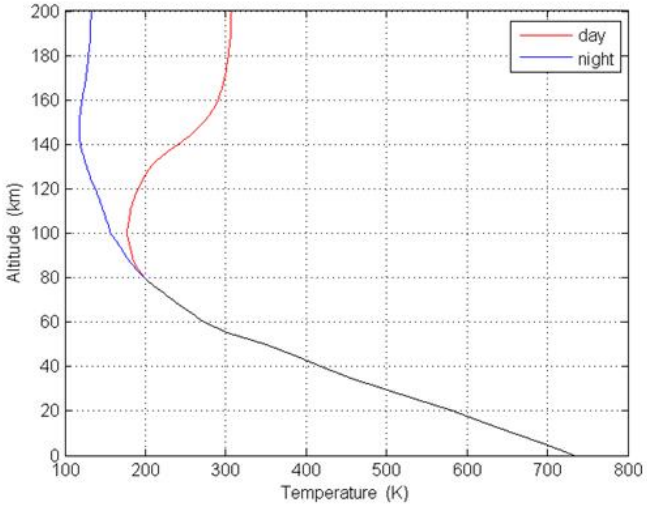

Figure 1.1.2: VIRA model for the evolution of temperature as function of altitude in the venusian atmosphere. Credits: Belgian Institute for Space Aeronomy.

The cloud deck on Venus has a determining influence on the planet's albedo, thermal structure and energy balance. The cloud layer that covers the planet consists mainly of H_2SO_4 droplets (which is 85% of an aqueous solution) and other aerosols of a still unknown composition (Gonçalves, R., 2016). The cloud layer is extended approximately in the 48-70 km range, with thin hazes up until 90 km and below the main cloud deck, starting roughly at 30 km (Esposito et al., 1983), with average size of aerosol particles changing from cloud to cloud. As with the overall atmospheric structure, the cloud deck can also be divided into three layers (Knollenberg and Hunten, 1980): An upper layer, ranging between 57-68 km with an averaged particle radius of 0.3 μm, and a total optical depth of 7 at a wavelength of 0.63 μm; a middle layer (51-56 km) where particle sizes are mainly between 1-1.4 μm and greater optical depths at the same wavelength as before; and the lowermost layer which begins in the base of the cloud deck at 48 km and where the optical depth continues to increase due to the increasing size of buoyant particles (3.65 μm).

Various polarimetric and spectroscopic observations point to a general composition ratio of 25% H_2O and 75% H_2SO_4 in cloud particles. The sulphuric acid in the cloud tops is synthesized from a photolysis and recombination process of H_2O and SO_2 that reacts with CO_2 in the following

chain reaction:

$$CO_2 + SO_2 + h\nu \longrightarrow CO + SO_3, \tag{1.4}$$

$$SO_3 + H_2O \longrightarrow H_2SO_4. \tag{1.5}$$

A representation of Venus' cloud deck follows in the next figure.

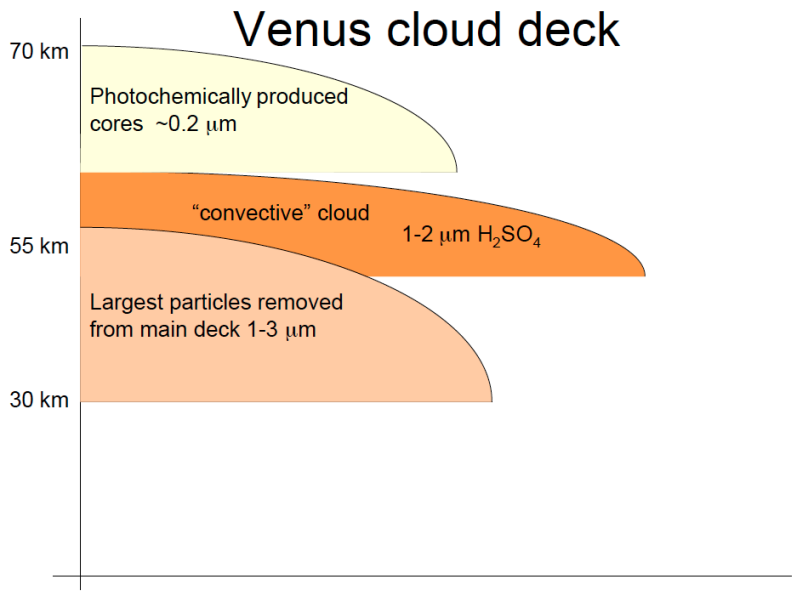

Figure 1.1.3: Venus' sulphuric acid cloud deck and hazes extension in altitude. Regarding the averaged aerosol particles size, the cloud deck can be divided in the three layers shown in this scheme. Figure: Titov, D., private communication.

Dynamics

Venus' characteristic motions and peculiarities drive many interesting atmosphere dynamics which drastically differ from those seen on Earth, despite the already seen similarities. The solid globe of Venus rotates once in every 243 terrestrial days (Pater, I., Lissauer, J., 2007) whereas its cloud system rotates much faster (closer to 4.4 days at the upper cloud layer and about 6 days at the lower clouds). Atmospheric dynamics on Venus are mainly driven by thermal heating and by the low rotation rate of the surface.
We define two wind velocity components, being them the zonal wind **u** (along isolatitudinal lines), meridional wind **v** (along the meridians) and a third vertical wind **w** (upwards). We can distinguish three main global circulation processes that characterize Venus' atmosphere dynamics:

– **Retrograde zonal wind with super-rotation**: Wind flow at great speed ($\approx$ 55 times the rotation speed of the globe) parallel to the equator in quasi-laminar bands, between the altitudes of 60-100 km and stretching between mid-latitudes. This retrograde zonal wind (RZW) is accompanied by a Hadley-type meridional circulation cell which extends from the equator to the poles on both hemispheres and converge to an unique polar vortex circulation.

– **Sub-solar to anti-solar circulation**: High in the thermosphere (above 120 km of altitude) the lower density and greater exposure to solar radiation drive this characteristic motion which highlights the contrast between the day and night sides on Venus, regarding density and

temperature. This difference between both daylight hemispheres gives rise to horizontal pressure gradients. On a general note, the flow pattern seems axisymmetric about the Sun-Venus line, with dayside upwelling centered on the subsolar point, strong cross-terminator flow and subsidence centered on the antisolar point. A return flow at lower altitudes would then complete the circuit (Fox and Bougher, 1991).

– **Meridional Circulation (Hadley Cell)**: Characterized by an air cell on each hemisphere, responsible for the transport of the heat excess from low latitudes, polewards to cooler high latitudinal regions. The Hadley circulation cell consists of rising air near the equator and submersion at the poles, converging in a polar vortex circulation. The net upward transport of angular momentum by the Hadley cell is able to maintain an excess of angular momentum in the upper atmosphere, balanced by equatorward transport by planetary waves. However this Hadley circulation has not been clearly characterized observationally and remains more of a theoretical construct in dire need of quantitative support (Gonçalves, R., 2016).

Still diving in the dynamical aspects of the atmosphere of Venus, and for the purpose of this work, we also address the polar vortex motions and small scale atmospheric gravity waves in this introduction:

– **Polar Vortex**: This three dimensional feature is highly variable and has been seen as a monopole, dipole and triple pole shape and it has been observed to change fairly quickly. The vortex eye rotates around the polar axis faster than the RZW of the mid latitudinal range. The south pole vortex was observed recently (Luz et al., 2011; Garate-Lopez et al., 2013) showing a period of about 2.7 terrestrial days and remarkable shape variability. There is yet to be established a relationship between the super-rotation of the atmosphere and dynamics and variability of the polar vortex, being a major topic in current scientific research.

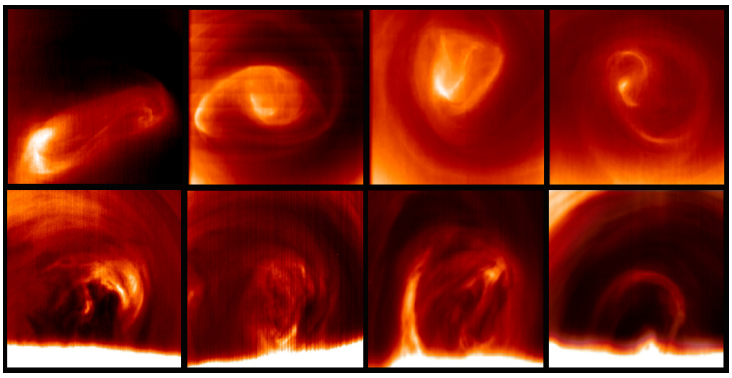

Figure 1.1.4: The south polar vortex as seen by the VIRTIS instrument onboard Venus Express ESA's mission. The images at the top of the figure show the upper cloud of Venus at 65 km. The images on the bottom depict the polar vortex at lower altitudes (close to the bottom of the cloud at 48 km) showing the vertical extension and variability of the vortex. Credits: (Garate-Lopez et al., 2013)

– **Atmospheric Gravity Waves**: A gravity wave is a wave-like disturbance on the atmosphere in which buoyancy acts as the restoring force. It can only exist in a stably stratified atmosphere and are possibly triggered by horizontal flow passing an obstacle (Alexander, M.J. & Holton, J.R., 2004), convection below or some kind of Kelvin-Helmoltz instability. These features are very important since they can transport energy and momentum by propagating both horizontally and vertically within the atmosphere and they could be playing an important role in the maintenance of the atmospheric circulation of Venus.
On Earth, atmospheric gravity waves frequently reveal their presence through cloud formations and are often generated in the troposphere by the clash of two different weather fronts or by airflow over mountains. Then they tend to propagate to higher altitudes where they are usually broken by nonlinear effects, transferring their momentum and energy to the mean flow of the

atmosphere (Sanchez-Lavega, A., 2011).

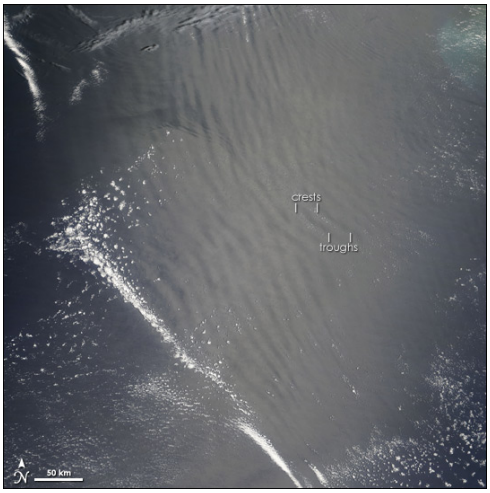

Figure 1.1.5: Atmospheric gravity waves on earth's atmosphere.

On a recent study (Piccialli, A. et al., 2014) periodic structures interpreted as gravity waves are observed in high resolution images acquired by the Venus Monitoring Camera (VMC) at the cloud tops at high latitudes in the Northern hemisphere. Vertical displacement of waves estimated by solar incidence angle is of the order of 3-70 m. Wave properties seem not to vary with latitude or local time however this information is biased by the constraint of observation by VMC (could not observe latitudes lower than $\sim 45°S$ or on the nightside with enough resolution to observe these features clearly, during the period of observations in the paper (Piccialli, A. et al., 2014)). Wave activity was mostly found in the cold collar region ($60° - 80°N$) and concentrated above a continental highland in Venus (Piccialli, A. et al., 2014).

Another systematic gravity wave search was carried out by (Peralta, J., et al., 2008) with observations performed with the Visible and InfraRed Thermal Imaging Spectrometer (VIRTIS), detecting mesoscale gravity waves in the upper cloud tops ($\sim$ 66 km altitude) using reflected ultraviolet light (380 nm) on the dayside hemisphere and in the lower cloud ($\sim$ 47 km altitude) using thermal radiation (1.74 μm) from the night side hemisphere. Observable properties of the waves were also measured such as packet length and width, orientation and geographical position on Venus.

1.1.2 Exploration of Venus

History of Venus Space Exploration

Venus has always been a shining beacon in the evening sky for entire civilizations. It has been the subject of many myth and legend and even ascended to godhood in different cultures. Early observation of this body provided insight which supported the, at the time, controversial hypothesis of *heliocentrism* opposing conventional beliefs. Since the beginning of the space age, more than 30 different spacecraft have been launched toward Venus and it was the first successful planetary target for human space exploration (Mariner 2, 1962). The measurements made with its magnetometer confirmed the high surface temperatures of $\sim 460°$C.

The *Venera* program (1961-1984) achieved important milestones on the research of this planet

as some of its probes were able to survive the extreme conditions on the surface long enough to collect and send data back to earth.

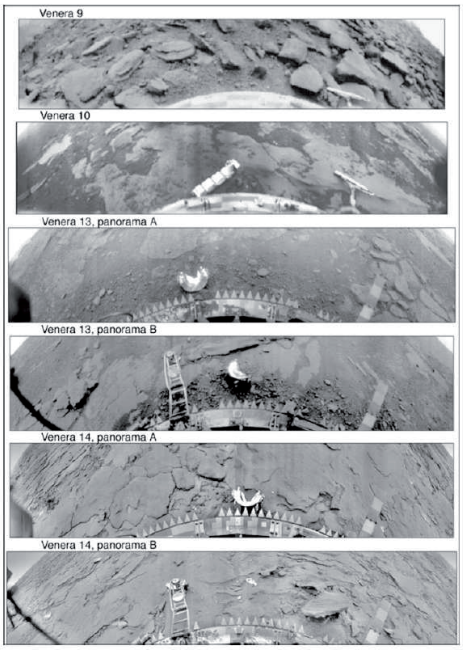

Figure 1.1.6: Surface images of Venus, taken from the Venera landers which were among the first images taken by man inside another planet. Credits: Russian Academy of Sciences.

The following russian mission *Vega* and the american *Pioneer* mission were essential for the study of atmospheric chemistry and physical description in Venus and they showed evidence of an extremely active atmosphere with corrosive gases (sulfuric acid as we have seen earlier). The Galileo spacecraft, during a Venus fly-by gravity assist (1990) on its way to the jovian system, provided high resolution observation on the infrared which improved our knowledge on cloud properties and variability.
In 1992, the Magellan orbiter was able to construct a comprehensive radar-mapping of nearly all the planet's surface with a resolution of close to 200 meters. The mission also contributed with gravity data, surface topography and electrical characteristics.

Figure 1.1.7: Venus' surface obtained through radar data from the Magellan Orbiter in 1992. It is still one of the most complete topographical maps of this planet to date. Credits: NASA, JPL, Magellan Project.

Venus Express

Venus Express (VEx) is a spacecraft that was launched on the 9^{th} of November of 2005 by the European Space Agency (ESA) with the primary mission of performing a global investigation of the venusian atmosphere after a long period without any space missions to this planet. VEx highly eccentric orbit (250 km at pericenter and 66 000 km at apocenter) allows scientist both global, large scale investigations and smaller scale but with high spatial resolution, detailed studies of localized phenomena like the atmospheric gravity waves.

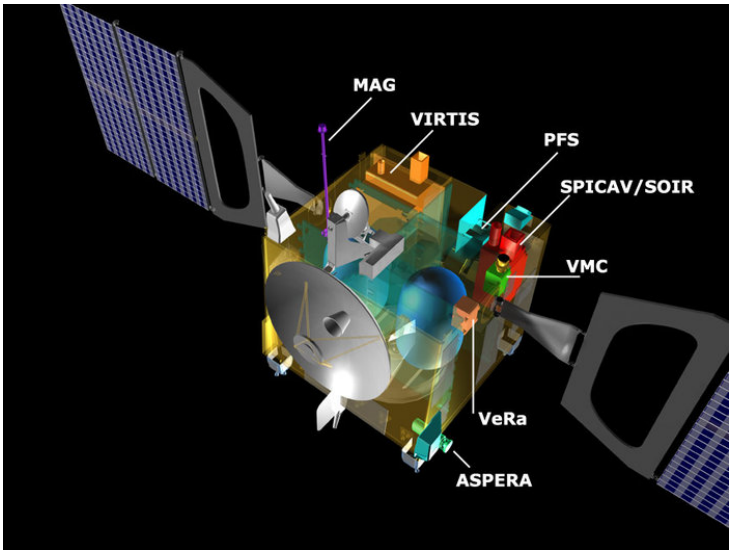

Figure 1.1.8: Venus Express cutaway diagram, showing the size and location of the onboard instruments. Credits: ESA.

On board the spacecraft, the following instruments were packaged in order to retrieve the best possible scientific data. See figure 1.1.8 for their location within the spacecraft:

•**ASPERA (Analyser of Space Plasma and Energetic Atoms)** – ASPERA was designed to investigate the interaction between the solar wind and the atmosphere of Venus and study how the molecules and ions escape the planet.

•**MAG (Venus Express Magnetometer)** – Venus has no detectable internal magnetic field, and the field that is detected is generated by the interaction between the solar wind and the atmosphere. This magnetometer studied this process and helped in our understanding of the effect it has on the atmosphere.

•**PFS (Planetary Fourier Spectrometer)** – This instrument was able to measure the temperature of the atmosphere between the altitudes of 55-100 km with high resolution. It also performed a thorough search for volcanic activity and made some composition measurements of the atmosphere.

•**SPICAV/SOIR (Ultraviolet and Infrared Atmospheric Spectrometer)** – SPICAV was designed to search for water in the venusian atmosphere. It also allowed the determination of the density and temperature in the thermosphere, at 80-180 km.

•**VeRa (Venus Radio Science Experiment)** – Using the required powerful radio link between the spacecraft and Earth, VeRa investigated the conditions in the ionosphere of Venus and the solar wind in the inner part of the solar system.

•**VIRTIS (Ultraviolet/Visible/Near-Infrared mapping spectrometer)** – VIRTIS was an imaging spectrometer that combines three observing channels in one instrument. Its data can be used for cloud tracking in both ultraviolet and infrared wavelengths to allow for the study of atmospheric dynamics at different altitudes.

•**VMC (Venus Monitoring Camera)** – The VMC camera contains a 1032 × 1024 pixel CCD detector which captures light through four separate objective lens systems, each of which images a different, filter selected, wavelength range. As it is allowed by the eccentric orbit of VEx, the VMC instrument was able to gather global images and localized features in Venus and assists in the identification of phenomena seen by other instruments.

By November 2014, the science mission would come to a close after an aerobraking maneuver

VMC filter parameters				
Filter	**Centre wavelength (µm)**	**Bandwidth (µm, FWHP)**	**Observation goals**	
			Dayside	**Nightside**
F3 (UV)	0.365	0.04	Unknown UV absorber	O_2 nightglow at 0.356 & 0.376 µm
F4 (VIS)	0.513	0.05	Visible light imaging	O_2 nightglow at 0.376 µm
F5 (NIR1)	0.965	0.07	H_2O at ~70 km	H_2O below 70 km, clouds
F6 (NIR2)	1.01	0.02	H_2O below 70 km	Surface, clouds

Figure 1.1.9: VMC filter parameters. Credits: ESA.

Summary of VIRTIS Characteristics			
	Mapper subsystem		**High resolution subsystem**
	Visible channel	**Infrared channel**	**Infrared channel**
Spectral range (µm)	0.25 - 1.0	1 - 5	2 - 5
Maximum Spectral resolution (nm)	~2	~10	~3
Spectral resolving power (λ/Δλ)	100 - 200	100 - 200	1000 - 2000
Field of view (mrad) - "pushbroom" mode	64×0.25	64×0.25	0.45×2.25
Field of view (mrad) - scan mode	64×64	64×64	-
Spatial resolution (mrad)	1.0 (default) 0.25 (high)	1.0 (default) 0.25 (high)	1.0

Figure 1.1.10: Summary of VIRTIS characteristics. Credits: ESA.

and through its years of probing the atmosphere of Venus it stumbled upon fantastic discoveries including the possibility of recent volcanism, atmosphere's super-rotation speeding up, spinning of Venus slowing down and that Venus is losing water and probably has been losing it through millions of years since it's formation.

1.2 Jupiter - King Planet of the Solar System

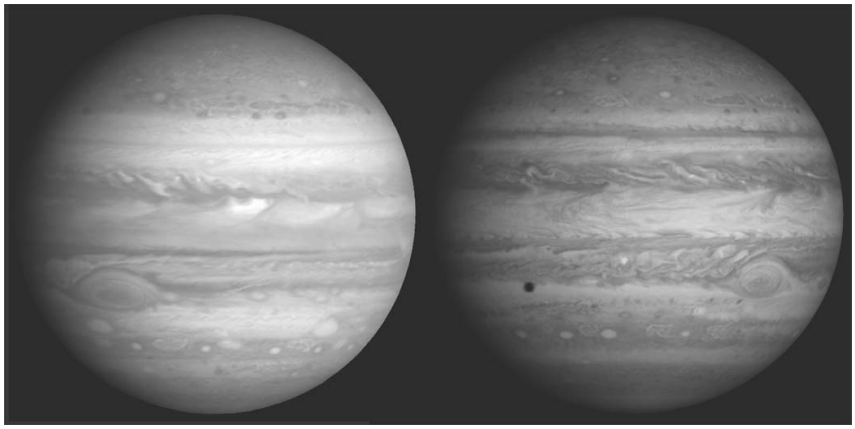

Figure 1.2.1: Whole disk views of Jupiter. The left image is from *Voyager* 2 in June 1979 while the right image is taken from *Cassini* in November 2000. The shadow on the right image is caused by Jupiter's moon Europa which has an orbit with an average radius of 67,000 km (close to 9.4 Jupiter radii). Credits (Ingersol, A.P et al., 2004)

As it is well known, Jupiter is the largest, most massive planetary object in the solar system. In fact it has more than twice the mass of all the other planets combined (Irwin, 2009), which has a noticeable influence on the orbits of all the other bodies of the solar system, in particular its numerous moons and thousands of other smaller bodies like the *trojans* and *centaurs*.

In contrast with Earth or Venus, the interior structure and the 'surface' are much more puzzling to comprehend for the gas giants. For one, all giants are mainly composed of hydrogen and helium with trace amounts of other *metals* (every other element heavier than helium) whose abundances are several times the solar value, increasing the further we travel from the Sun regarding all four giants (Jupiter, Saturn, Uranus and Neptune). The generally favoured interpretation for this, along with size and density measurements, is that the outer planets accreted originally from icy planetesimals and became massive enough to gravitationally attract hydrogen and helium from the solar nebula. The difference in heavy element abundance possibly comes from Jupiter and Saturn growing large enough to rapidly capture copious amounts of gas whereas Uranus and Neptune, being farther away, where the nebula is less dense, were left with fewer material for accretion (Irwin, 2009).

As for the 'surface' of these planets, since the internal structure is poorly known due to the fact that the only way to probe deeper regions is by calculating interior models that match observed gravitational and magnetic fields, so this only yields information on quantities that are averaged over a significant fraction of the planetary radius (Guillot, T., 1999). Having said this, there is no indication for the existence of a surface as we know it, for the gas giants. As we dive deeper in the atmosphere of Jupiter for example, both temperature and pressure rise which leads to exotic physical state transitions in the interior of the planet. One of these states, concerns the point where hydrogen is thought to change to an electron-degenerate state of pressure-ionized protons and electrons called *metallic hydrogen* (Irwin, 2009). As most of these transitions appear to be continuous rather than having a sharp boundary since they depend on rising temperature and pressure conditions, any kind of surface is not expected in Jupiter, the only possible boundary being where the outer edges of the putative core in Jupiter is located.

1.2.1 Jupiter's Atmosphere

Composition

As I previously mentioned, there is no sharp boundary between the atmosphere and the internal regions of Jupiter where thermodynamic conditions do not allow the existence of an atmosphere as we know it on Earth or Venus (with a predominantly gaseous phase with several condensable species). As it is quite challenging to describe the altitude of layers on the atmosphere of Jupiter (since there is no surface) we will refer to layers by atmospheric pressure that is expected or measured in each region, assuming that all of the jovian atmosphere is in hydrostatic equilibrium.

Species	Jupiter
Mixing ratios relative to H_2	
Major Species	
H_2	1.0
He	0.157 ± 0.0036
Minor Species	
H_2O	Global: 6.0 $(+3.9,-2.8)\times 10^{-3}$, $(2\text{-}20)\times 10^{-9}$(upper stratosphere), $\leqslant 10^{-6}$ (below 4 , hotspot) , $(5.6 \pm 2.5)\times 10^{-5}$(12 bar, hotspot)
CH_4	$(2.1 \pm 0.4)\times 10^{-3}$
CH_3	Detection (polar region)
C_2H_6	$(1\text{-}5)\times 10^{-6}$ (stratosphere)
C_2H_2	$(3\text{-}10)\times 10^{-8}$ (stratosphere), $< 2.5\times 10^{-6}$(1-10 μbar)
C_2H_4	$(7\ pm\ 3)\times 10^{-9}$ (north polar region)
C_3H_4	$2.5(+2,-1)\times 10^{-9}$ (north polar region)
C_3H_8, C_4H_2	Detection
C_6H_6	$2(+2,-1)\times 10^{-9}$(north polar region-stratosphere)
NH_3	$\sim(0.2\text{-}1)\times 10^{-5}$ (0.5-2bar, hotspot), $(3.3pm1.5)\times 10^{-4}$ (4 bar, hotspot), $(8.1pm1.16)\times 10^{-4}$ (8 bar, hotspot), $(7.1pm3.2)\times 10^{-4}$ (9-12 bar, hotspot)
H_2S	$<2\times 10^{-8}$($<$0.7 bar, global), $< 1\times 10^{-7}$($\leqslant$ 4 bar, hotspot), 7×10^{-6}(8.7 bar, hotspot), $(7.7pm0.5)\times 10^{-5}$(16 bar, hotspot)

Table 1.1: Composition of the Atmosphere of Jupiter. Table taken from (Atreya, S.K, et al., 2003)

In table 1.1 we can find the composition of the atmosphere of Jupiter, which is the most comprehensively known gas giant, partially due to the *Galileo* entry probe which plunged into the jovian atmosphere (on a hotspot region) and was able to collect and send data back to Earth until the 20 bar level, beyond which the probe was presumably crushed by atmospheric pressure.

Jupiter's atmospheric chemistry is closely related to that of the Sun in terms of molecular and atomic hydrogen and partially helium being the dominant species, with minor abundances of heavy elements and as previously stated, heavy element abundance is much higher in the giants than in the Sun (the very least being Jupiter, with 3-5 times the solar heavy element abundance). Taking a closer look at the sprawling variety of chemical species in the jovian atmosphere re-

veals many aspects of the primordial solar nebula (from which we come from) as well as several dynamical features ongoing in Jupiter.

The stability of different chemical forms on which several elements exist in the atmosphere is highly dependable upon temperature and on the abundance of other molecules and atoms with which reactions may occur. Hence, some species are designated as *disequilibrium species*. Two of these are the molecular forms of carbon and nitrogen. The chemical form of both these elements that is observed depends upon the following equilibrium reactions:

$$CH_4 + H_2O \rightleftharpoons CO + 3H_2 \tag{1.6}$$

$$2NH_3 \rightleftharpoons N_2 + 3H_2 \tag{1.7}$$

Above the temperature of 1000°K, the right-hand side of these reactions dominate, whereas the other dominates at lower temperatures. Given this, as we are only able to see the top regions of atmosphere, we do not expect to see much CO or N_2 unless vertical transport is vigorous enough (Irwin, 2009). This mirrors how the measurement of the abundances of these particular species might provide information on the circulation of the giant planet atmospheres. Other important disequilibrium species include germane, arsine and phosphine, regarding the following reactions:

$$GeH_4 + H_2S \rightleftharpoons GeS + 3H_2 \tag{1.8}$$

$$4PH_3 + 6H_2O \rightleftharpoons P_4O_6 + 12H_2 \tag{1.9}$$

$$4AsH_3 \rightleftharpoons As_4 + 6H_2 \tag{1.10}$$

The chemical equations in 1.8,1.9 and 1.10 are simplifications of a much complicated tree of reactions, with more intermediate steps, however I only presented these for the sake of simplicity. Again, measurements of the vertical profiles of these species provide constraints in the eddy-mixing coefficient and mapping the spatial abundance of these materials provides more information on vertical motions of the atmosphere.

Another important mechanism in giant planetary atmospheres is **photolysis** which is the photodissociation of molecules by solar UV radiation in the upper parts of the atmosphere. I highlight the three most important photo-active gases in the upper troposphere and stratosphere of Jupiter: ammonia, phosphine and methane.

Photodissociation is of great influence in the abundance of these elements in certain parts of the atmosphere of Jupiter. For ammonia (NH_3), if it reaches high altitudes (approximately where pressures are of the order of 100 mbar) it starts to be broken to form hydrazine (N_2H_4) via the reactions:

$$\begin{aligned} NH_3 + h\nu &\rightleftharpoons NH_2 + H \\ NH_2 + NH_2 + M &\rightleftharpoons N_2H_4 + M \end{aligned} \tag{1.11}$$

Here, **M** is any other molecule. According to this, the abundance of ammonia should decrease above the 100 mbar level, which partially agrees with observations. Hydrazine should condense at temperatures found in Jupiter's upper troposphere and the resultant ice particles are a component of the haze layer on Jupiter's upper atmosphere. At this stage, ammonia can react with H_2S to form ammonium hydrossulfide (NH_4SH) which is found in the cloud decks of Jupiter and also on Saturn. At even upper levels, unbroken ammonia molecules can also freeze to form icy ammonia.

Photolysis of phosphine leads to the formation of diphosphine P_2H_4 by the reactions:

$$\begin{aligned} PH_3 + h\nu &\rightleftharpoons PH_2 + H \\ PH_2 + PH_2 + M &\rightleftharpoons P_2H_4 + M \end{aligned} \tag{1.12}$$

As with ammonia, photodissociation is expected to occur at the 100 mbar pressure level and if temperatures get low enough, diphosphine condenses and becomes another component of the cloud deck. However if it does not condense, further reactions are allowed which can produce the solid phosphorus allotrope P_4 which is bright red. This may suggest that the red coloration of the *Great Red Spot* is brought by a concentration of this chemical compound but this assumption is still unproven (Irwin, 2009).

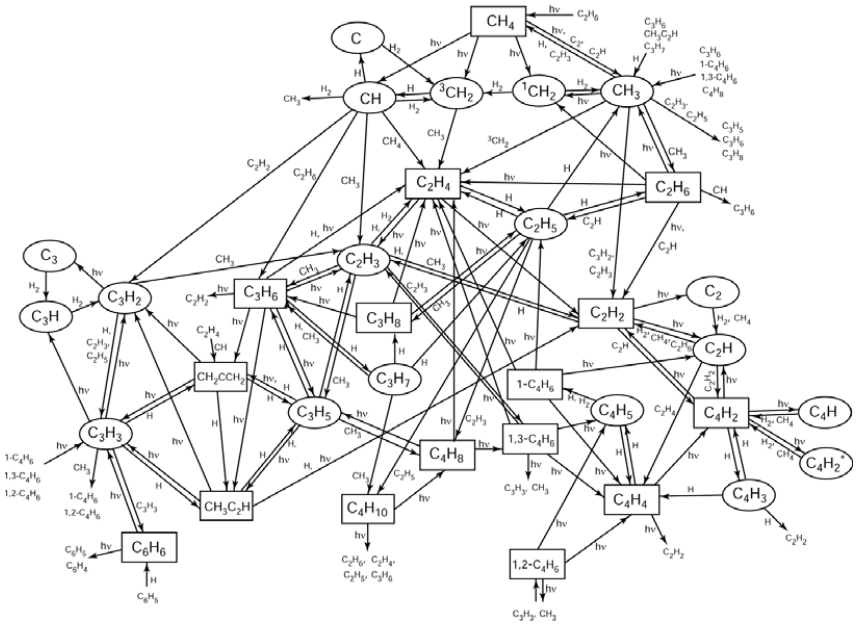

Figure 1.2.2: Methane photochemistry paths. From (Moses, J. et al., 2000).

As we noticed from table 1.1, several hydrocarbons are present in Jupiter's atmosphere mirroring the complicated chemistry involving methane photochemistry, illustrated in figure 1.2.2.

Photolysis of methane takes predominantly at higher levels in the atmosphere, with a peak level of photodissociation between 0.1 μbar and 0.1 mbar. While this may be the main region for methane photodissociation, to produce the observed hydrocarbons, other reactions are needed which are only efficient at higher pressures ($>$ 0.1 mbar). The main products of photodissociation are C_2H_2, C_2H_6 and several other molecules of the form $C_{2n}H_2$. These products will compose hazes which spread vertically through eddy mixing. The products that eventually descend into the atmosphere to warmer areas are pyrolyzed (decomposition of organic material in the absence of an halogen) back into methane again and possibly starting another cycle if methane is brought to higher layers of the atmosphere (Irwin, 2009).

Structure

As previously referred, a notion of vertical structure in Jupiter is quite challenging to define since our sense of 'surface' disappears in the gas giant along with our inability to accurately discriminate layers in the atmosphere. In spite of these difficulties, *Galileo's* entry probe data along with several radio occultation experiments and Infrared (IR) observations from other spacecraft instrument and ground-based observations have all contributed for a better understanding of the inner workings of Jupiter.

In a very rough approximation, the jovian atmosphere may be divided in three sections: tro-

posphere, stratosphere and thermosphere. A reference point could be taken at the 1 bar level in the atmosphere however significant cloud structure has been detected in deeper areas where pressure reaches at least 10 bar, hence this is often regarded as the base of the troposphere (Seiff et al., 1998).

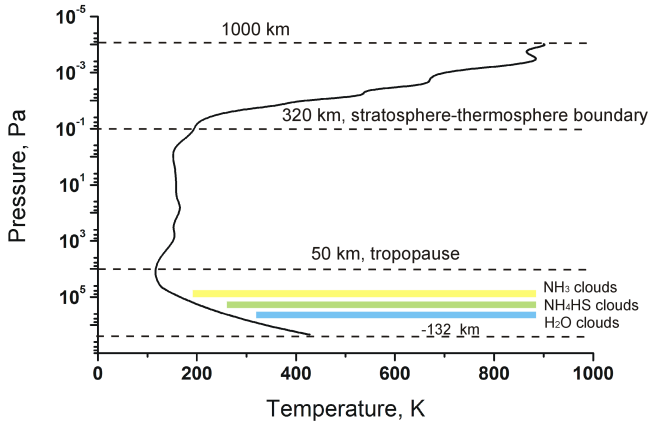

Figure 1.2.3: Vertical structure of the jovian atmosphere. Data obtained by the Galileo atmospheric probe which stopped transmitting at a depth of 132 km below the 1 bar layer of Jupiter. Credits to (Seiff et al., 1998).

As we can see from figure 1.2.3, the tropospheric region below 1 bar level is mainly characterised by several cloud decks dominated by different chemical species. Both NH_3 and NH_4SH cloud decks have been subject to extensive debate as it is largely unknown how these species condense in these regions, clearly influenced by vertical circulation which is still poorly understood. However there is a good deal of evidence approving the existence of the water cloud deck close to the 5 bar level and a base in the 6-7 bar layer (Irwin, 2009; Ingersol, A.P et al., 2004). Below this level, the bulk of Jupiter's interior is expected to be convective and the simplest model tells of a dry adiabatic profile, at least until the 1 bar pressure level (Seiff et al., 1998; Ingersol, A.P et al., 2004).

Above 300 mbar there seems to be a statically stable atmosphere and upwards into the stratosphere, haze layers seem to settle and combine with an ammonia cloud contaminated with hydrocarbons and possibly the phosphorus allotrope mentioned earlier which could give a reddish colour to this layer of clouds in some regions. These contaminators are believed to be generated in the upper stratosphere (1-100 mubar) from the photolysis of methane described earlier. However it has already been pointed out that our colour perception in low light intensity conditions is quite poor and all Jupiter images we are accustomed to are severely colour-stretched and Jupiter's atmosphere appears much more bland in reality (Irwin, 2009).

Above the stratosphere, close to 1 μbar we find the thermosphere, which forms the boundary between the lower atmosphere and interplanetary space. Being, the top-most layer, it absorbs solar ultraviolet radiation with full force and charged particles of the magnetosphere, which cause dissociation and ionization of the present molecules. In this region, densities are low, which leads to large mean free paths between collisions. As a consequence of this property, molecular diffusion becomes dominant over convective mixing. Given this interaction with charged particles, powerful aurorae are triggered in the polar regions. The jovian thermosphere, along all other upper atmospheres of the giant planets, is also characterised by high temperatures as seen in figure 1.2.3, although there is yet to be an explanation for the observed temperatures (800-1000 K) (Yelle, R.V., et al., 2004).

Dynamics

Jupiter has one of the most mesmerizing atmospheric patterns in the solar system and its famous, high contrast banded structure is easily seen on Earth with a small telescope. Even though, according to (Ingersol, A.P et al., 2004), models of Jupiter's atmosphere tend to be less complex than models of Earth's atmosphere they are no less interesting and intriguing, starting from the fact that they symbolise a reality far from the one we know on our home in the Universe.

As referred before, Jupiter's visible atmosphere is dominated by a banded structure with bright white regions (zones) and darker brown/reddish bands (belts) with prominent zonal jets (latitudinal currents in the atmosphere) between zones and belts. Both band types flow in different directions with zonal winds that reach 150 m/s, with greater intensity towards the equatorial zones and belts. Individual features like the *Great Red Spot*(GRS) tend to have the same vorticity (sense of rotation) as the band in which they are placed.

As discussed before, the origin of the colour in the belts is uncertain as the major cloud constituents (NH_3, H_2S, H_2O) are colorless but elemental sulphur, phosphorous and some hydrocarbons could combine in trace amounts to trigger the observed coloration.

Belts are seen as more variable regions than zones, since small and large scale features have short lifespans in these bands, as opposed to the bright zones which are generally steadier in time. Clouds also have predominantly different heights, being higher in zones, where gaseous ammonia condenses and/or freezes due to the lower temperatures while belts are located deeper in the atmosphere. The hot spots mentioned earlier (as in the descent of the *Galileo* entry probe) appear to be holes in the visible cloud deck that allow radiation to escape from lower, warmer regions below. As this radiation is more intense around $5 - \mu$m, since there are less gaseous absorptions lines which halt emission in this wavelength, these holes were baptized as 5-μm hot spots.

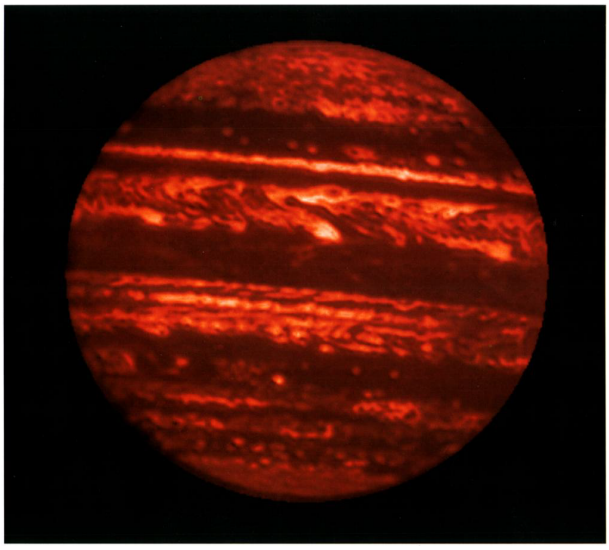

Figure 1.2.4: A high resolution view of Jupiter in the M narrowband (IR - 5 μm). This image is shown in false color and has been stretched logarithmically. Jupiter is a prominent emitter in the IR, since lower visible layers (belts) glow brightly in these wavelenghths and hotspots are seen here as the brightest areas, which sometimes exceed 273 K in brightness temperature (Ingersol, A.P et al., 2004; Ortiz, J., et al., 1998).

.

Despite the banded structure being globally stable over centuries of observation, the variable

nature of the belts sometimes results in small convective events that grow to great heights and encircle the planet and the boundaries between bands and belts may change slightly in latitudinal extent (Ingersol, A.P et al., 2004).

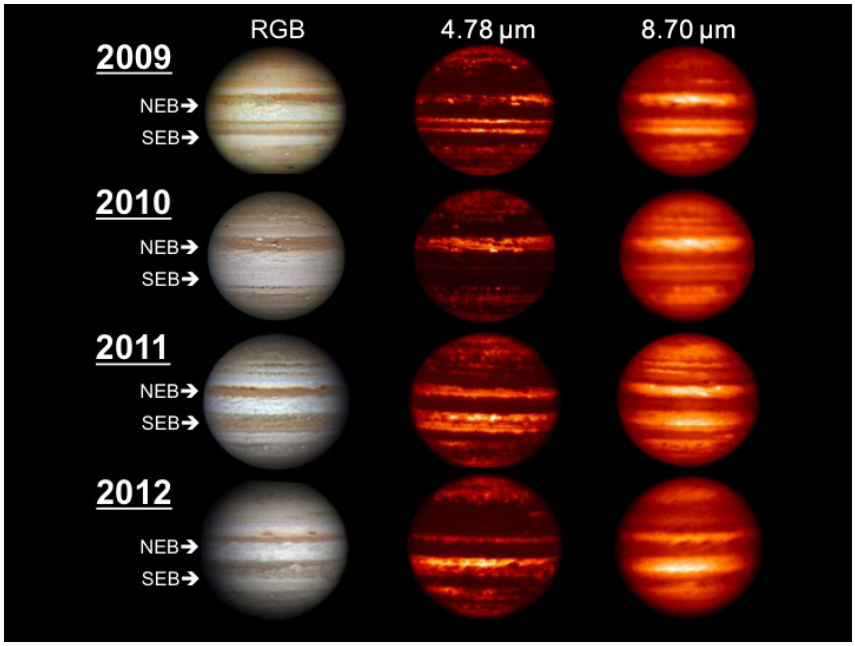

Figure 1.2.5: Images of the jovian disk during a remarkable upheaval event of the south equatorial belt in 2010 both in the visible and infrared range. We can also notice a thinner north equatorial belt by 2012. Credits: NASA.

Inside the zones are the major anticyclonic systems like the GRS, the White Ovals and smaller storms. These often extend beyond the width of their host zones and sometimes completely block off neighbouring belts, leading to turbulence in these regions, as can be observed close to the GRS for example. Even though cyclonic features in Jupiter seem to last several years and the most famous one (GRS) has been around since more than 150 years, the GRS has been observed to significantly decrease in longitudinal extent compared with first measurements made in 1880 which showed an east-west length of 39,000 km while present observations reveal that it now presents only approximately 17,000 km width.

The large-scale motions of the jovian winds are in approximate geostrophic balance. This comes from several first approximations to the equations of motions on general planetary atmospheres (Navier Stokes equation - momentum equations) described below:

$$\frac{du}{dt} - fv + \frac{1}{\rho}\frac{\partial p}{\partial x} = F^{(x)} \tag{1.13}$$

$$\frac{dv}{dt} + fu + \frac{1}{\rho}\frac{\partial p}{\partial y} = F^{(y)} \tag{1.14}$$

Where u and v are the zonal and meridional winds respectively (wind velocity in the east-west direction and wind velocity in the north-south direction), f is called the Coriolis parameter,p is the pressure and F represents a friction force in both x and y directions. For the large scale motions of Jupiter, frictional forces and variations in wind speed with time are negligible, reducing equations 1.13 and 1.14 to the geostrophic equations:

$$fv = \frac{1}{\rho}\frac{\partial p}{\partial x} \tag{1.15}$$

$$fu = \frac{1}{\rho}\frac{\partial p}{\partial y} \tag{1.16}$$

These lead to anticyclones like the GRS and White Ovals being high-pressure centers while cyclones have low-pressures in their cores (Irwin, 2009; Ingersol, A.P et al., 2004). The traditional view for Jupiter holds that as in the deep oceans on Earth, winds are weak in the deep atmosphere and the strong winds we see on the visible atmosphere are quite shallow. This implies that the zones and anticyclonic features are warmer than their surroundings. Since warm air tends to rise and cold air tends to sink, it is natural to assume that the air in the zones is slowly rising while air in the belts is sinking. As clouds have a tendency to form on updrafts, this view is consistent with observations of the visible cloud deck in zones, which has been reported to be higher as previously mentioned (Terrile and Westphal, 1977).

Another theory holds that the winds are just as strong in the deep atmosphere as they are in the observable cloud deck. If the fluid is barotropic, meaning that the temperature is constant at constant pressures, the zonal jets would be a surface manifestation of rotating cylinders concentric with the planet's rotation axis and the fluid would move in columns throughout the globe. However, if the fluid is baroclinic (temperature varies at constant pressure) the fluid could not move in columns. The distinction between these two behaviours of the shallow/deep rivalry, requires knowledge of both winds and temperatures in the deep atmosphere which is extremely challenging as explained above (Poincaré, 1910; Ingersol, A.P et al., 2004).

Regarding some discrete features in the jovian visible atmosphere, I will focus some part of this discussion on the GRS itself and similar anticyclonic (White Ovals) and cyclonic features on the turbulent atmosphere of Jupiter.

Jupiter's GRS is the most dominant and long-lived feature in the jovian atmosphere which has been observed to be acquiring a more circular shape and is also shrinking, displaying the lowest size ever recorded (Parisi et al., 2015).

Although it shows the behaviour of a 2D vortex similar to the anticyclonic storms on Earth,

Figure 1.2.6: Jupiter's Great Red Spot close-up by *Voyager 1*. This image was assembled from three black & white negatives with colour greatly enhanced. Credits: NASA.

the fact that this storm is at least more than 150 years old leaves the question whether or not this is a shallow atmospheric feature or a deeply rooted vortex. As stated before, measurements of deep wind dynamics were only performed with good accuracy with *Galileo* entry probe which

detected strong eastward zonal winds characterized by velocities of up to 160 m/s. However, the pressure level reached (22 bar) only represents about 0.2% of the average planetary radius and *Galileo's* entry site (a 5 μm hotspot) might not give a representative view of deeper layers of Jupiter's atmosphere. As the question surrounding the storm's depth is tied to important dynamic behaviour in Jupiter, particularly for the deeper layers of the atmosphere, the key to this question might come from studying the gravitational signature of the cyclone with precise gravity measurements from *Juno's* gravity experiment (Parisi et al., 2015).

White Ovals are other remarkable anticyclonic features which have been seen to merge with one another to create bigger storms which remain white or change to a more reddish colour. They can form in several ways, including an updraft whose spreading motion produces anticyclonic vorticity or when an anticyclonic zone breaks up. The rotation of the largest white ovals is well defined by their interior cloud texture, and tangential velocity has been observed to increase approximately linearly with radial distance out to the visual frontier. Like the GRS, these ovals are cold at upper tropospheric levels which along with coloration and observed increased altitude of overlying hazes all suggest moderate upwelling within white ovals.

Cyclonic regions tend to be more spread out in the zonal direction than the anticyclonic ovals which can be seen in figure 1.2.6 to the right of the anticyclonic ovals as a more chaotic, filamentary feature. However the shape of cyclonic feature is more varied than that of anticyclonic ones and do not last nearly as long. As I mentioned before, some anticyclones invade neighbouring belts which can break it into a series of closed cyclonic cells. This behaviour has been reproduced in the laboratory and can also be seen in nature where such configurations form in wakes behind blunt obstacles (partially obstructed rivers) leading to small, fairly stable perturbations.

1.2.2 History of Jupiter's Exploration

As chief planet of the solar system and the closest of the giants to the Sun, Jupiter can easily be seen on the night sky in the northern hemisphere. The first observations through a telescope were performed by Galileo Galilei in 1610 who discovered its four largest moons (Io, Europa, Ganymede and Callisto). In the advent of the space age came the first fly-by missions to the outer solar system, starring *Pioneer 10* which flew past Jupiter in December 1973 followed by *Pioneer 11* a year later. These missions not only provided the first ever close-up images of the visible layers of the atmosphere but also gave greater insight into the harsh radiation environment that involves the jovian system which helped prepare succeeding missions to the planet.

In 1979 the *Voyager* program flew past the jovian system and both missions (*Voyagers 1 and 2*) vastly improved our understanding of the Galilean moons, observing volcanic activity for the first time outside the Earth, discovered two satellites (Adrastea and Metis) and the Jupiter ring system.

In 1992, the *Ulysses* solar probe flew past Jupiter's north pole as part of swing maneuver to attain the desired high inclination orbit the probe was to perform around the Sun. During its time in jupiter's system, the probe performed several measurements of the planet's magnetosphere.

The first orbiter mission to Jupiter came with the already mentioned *Galileo* orbiter which arrived in orbit on December 7, 1995 and encircled the planet until 2003 when it was destroyed in a controlled impact with Jupiter. During its life-time, *Galileo* witnessed the impact of the Comet Shoemaker-Levy 9 as the spacecraft approached the Jovian system in 1994 and pioneered by sending the aforementioned entry probe in 1995.
Among major scientific discoveries, several can be highlighted: First observation of ammonia clouds in another planet's atmosphere; observation of complex plasma interactions in Io's at-

mosphere; provided evidence which supports the existence of liquid oceans under Europa's icy surface; first detection of a substantial magnetic field around Ganymede.

In 2000 the *Cassini* probe drifted past Jupiter on its way to Saturn and provided the highest resolution images of the jovian atmosphere to date (at that time). A more in depth analysis of this mission follows on the next chapter.

As Jupiter is the gateway to the outer solar system, since its incredible size and 'proximity' to the Sun allows the performance of gravity assists which help save energy and fuel, crucial to spacecraft survival in outer space, this to was the strategy of NASA's *New Horizons* mission to Pluto which flew by Jupiter in 2007 studying the less known moons like Amalthea, Himalia and Elara which are much more distant to Jupiter than the galilean moons.

Juno, the latest mission to Jupiter is still active, having been launched in 2011 and entered Jupiter's orbit in July 2016. This particular orbit takes the spacecraft within 5000 km above the jovian cloud tops to avoid the hazardous radiation environment during the mission and also to study with unprecedent detail the interior structure of Jupiter.

1.3 Saturn - Jupiter's Ringed Cousin

Saturn is a planet that has always caught our attention and curiosity, mostly caused by the presence of a massive and majestic ring system that surrounds the planet and is easily seen with a small telescope. This ring which is mainly composed of water ice is the biggest ring system of all gas giants and may have formed from tidal disruption of a captured satellite, where a smaller body got to close to the planet and through tidal forces was ripped apart, with contributions by sputtering of particles from other moons. Since the ring system appears to be significantly younger than the average age of the solar system (hence the planets) it must not be a remnant of the solar nebula which became gravitationally bound to the planet (Irwin, 2009).

1.3.1 Saturnian Atmosphere

Regarding the atmosphere in terms of structure, composition and dynamics, Saturn is similar to its cousin Jupiter in many aspects. As is the case of its cousin, Saturn is mainly composed of hydrogen and helium and trace amounts metals, with special relevance to nitrogen, oxygen, carbon and phosphorous. As this planet accreted less mass than Jupiter, it has a higher heavy element abundance ratio than its cousin and having less mass than Jupiter while being also farther away from the Sun, leads to a much deeper level for conditions for creation of '*metallic hydrogen*' to be met, which could explain the overall weaker magnetic field.

Element	Main Carrier	Abundance Ratio/H
He/H	He	$(6.75\ pm\ 1.25)\times10^{-2}$
C/H	CH_4	$(2.67\ pm\ 0.11)\times\ 10^{-3}$,
N/H	NH_3	$(2.27\ pm\ 0.57)\ \times10^{-4}$
S/H	H_2S	$(1.25\ pm\ 0.17)\times10^{-4}$
P/H	PH_3	$(4.65\ pm\ 0.32)\ \times10^{-6}$
Ge/H	GeH_4	$(2.3\ pm\ 2.3)\ \times10^{-10}$
As/H	AsH_3	$(1.25\ pm\ 0.17)\ \times10^{-9}$

Table 1.2: Elemental abundances measured in the troposphere of Saturn. Table excerpt taken from (Guillot, T., Gautier, D., 2015)

Looking at table 1.2 two aspects must be taken into consideration. One is that some of the carrier species presented condense or are in chemical disequilibrium, i.e., they may present altitude/geographical variations of their concentrations. The abundances presented are estimated from the maximum measured mixing ratio. Another is that abundance ratios r in this table are measured with respect to atomic hydrogen, while these atmospheres are dominated by molecular hydrogen and helium. Mole fractions f can be found with the expression $f = 2r/(1+f_{He})$ where r_{He} is the He/H abundance ratio (Guillot, T., Gautier, D., 2015).

The structure of the saturnian atmosphere is fairly similar to the one seen on the previous chapter. However, being a colder environment overall, gases condense at deeper levels and clouds are located in lower regions. The much more bland appearance of the planet comes mainly from this very reason. The cloud deck is located past an increased number of haze layers which block and scatter sunlight giving us a much more clouded view of the banded system.

Another noticeable difference is related to wind dynamics. In the equatorial region of Saturn, winds that exceeded 500 m/s when *Voyager 1* flew past the ringed planet revealed an even more

super rotating atmosphere than the one seen in Jupiter, despite of it being less internally heated than its cousin.

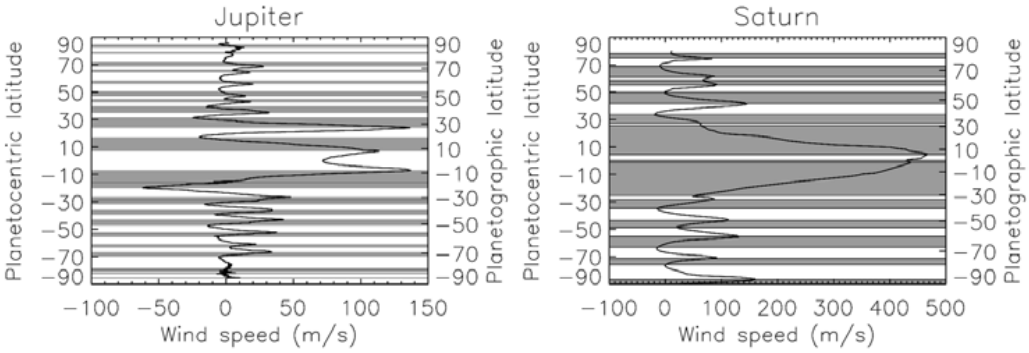

Figure 1.3.1: Zonal wind structure of Jupiter and Saturn with regions of cyclonic vorticity (winds that flow in the same direction as the planet's rotation, which for the case of Jupiter represents mainly belts) shaded in gray. Credits (Irwin, 2009)

Seasonal Variations

Opposing Jupiter, Saturn has considerable tilting of the equator to the orbital plane (26.7° (Fletcher et al., 2010)). Adding the presence of the ring system and elongation of the orbit around the Sun, Saturn is strongly affected by seasonal changes in solar radiation influx (Vidmachenko, A.P., 2015). As several structural, chemical and dynamical properties of the cronian's upper troposphere and stratosphere are determined by the energy distribution from multiple sources including radiative heating, seasonal variations have measurable effects on the atmosphere, particularly large-scale global circulation, photochemistry and aerosol production.

As noted before, the methane and ammonia present on the atmospheres of both Jupiter and Saturn take part in photochemical processes, hence are highly influenced by the amount of solar radiation that reaches the atmosphere. As seasons in Saturn can last roughly 15 years, this represents a substantial asymmetry on the irradiated hemispheres of Saturn throughout a whole season. Methane for one, has absorption lines both in the visible and IR wavelengths and its presence in the atmospheres of several gas giants gives a distinct bluish tone, characteristic of Uranus and Neptune's atmosphere. However as methane endures photolysis which breaks down this molecule into several other hydrocarbons, its abundance in the higher layers of the atmosphere might decrease in summer years. At the beginning of Cassini's mission in 2004, the northern hemisphere (which was enduring cronian winter) appeared with a shade of blue in visible light.

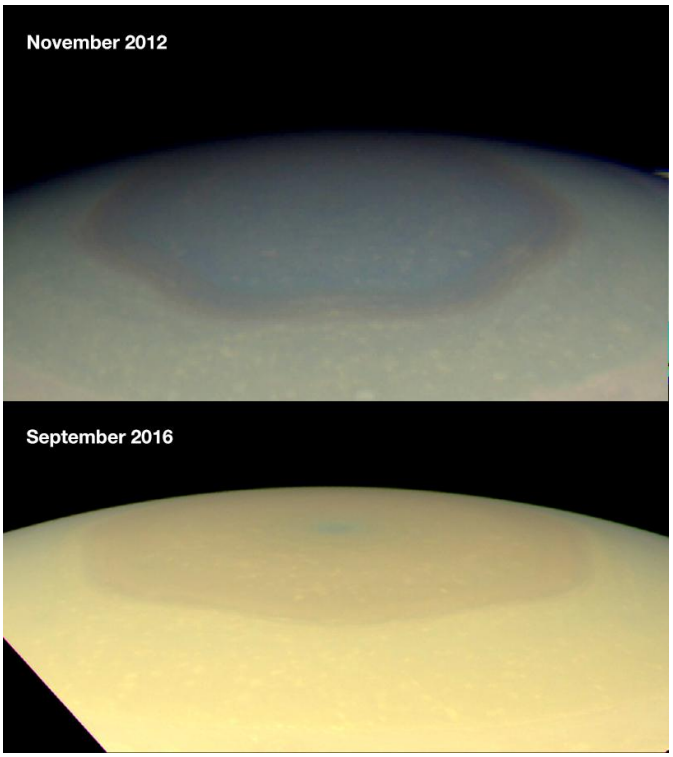

Figure 1.3.2: Seasonal variations of the appearance of the north polar region of Saturn in visible light. Note that in 2012 the poles still displayed a blueish tone whereas in 2016 this was replaced with the familiar yellow coloration of the equatorial regions of the planet. Credits: NASA.

As Saturn approached its equinox in 2007-2008, the northern blue hues progressively began to be eroded away and replaced with the familiar yellowish colour as time went by (see fig 1.3.2), consistent with increased haze production in the spring hemisphere (Fletcher et al., 2010). A possible explanation is that methane absorption is stronger in the winter which can be related to thinner or deeper tropospheric hazes in this season (Vidmachenko, A.P., 2015; Fletcher et al., 2010).
The shadow on the planet's mid latitudes further decreases the solar radiation influx on the surface. Obviously, less solar incoming radiation will mean a cooler atmosphere during winter seasons. However it was observed both in models by *Greathouse* and Cassini/CIRS observations that the temperature response to seasonal changes lags behind changes in solar heating, and the lag is increased with pressure.

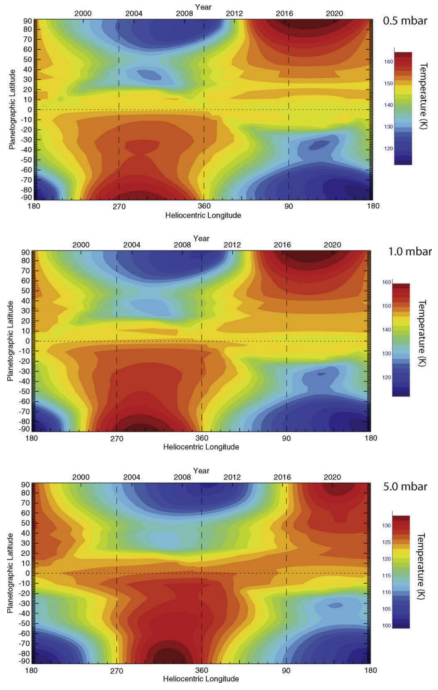

Figure 1.3.3: Predictions from the radiative climate model of Greathouse, showing expected thermal changes in the troposphere which have already been observed by Cassini/CIRS. The dashed vertical lines show the temporal location of equinoxes and solstices, demonstrating the lagged temperature response to higher/lower insolation. Credits: (Fletcher et al., 2010).

Polar Regions

The polar regions of the giant planets exhibit some of the most complex environmental conditions found in the outer solar system. They are the culmination of a planet-wide circulation system and are the meeting point between the neutral atmosphere and the magnetosphere via auroral activity (Fletcher, et al., 2014).

The hexagonal cloud pattern that encircles the north pole of Saturn is a unique feature in the solar system which was discovered by Godfrey in images taken during the *Voyager 2* flyby of Saturn in 1981. However the hexagonal shape was only noticed years later since the spacecraft has poor views of the poles and was only acknowledged when several images were mosaicked and mapped in polar projection. This shape is approximately 30,000 km across and centered on the north pole and the geometric shape is thought as a pattern in the atmospheric reflectivity (Sayanagi, K.M., et al., 2016).

In a latitude-longitude cylindrical projection the hexagon's outline resembles a simple sinusoidal function with zonal wavenumber-6 that meanders between 75.3° and 76.3° PC (planetocentric) latitude. The interior of the hexagon is filled with vortices of varying sizes, from the limit of image resolution to several thousand km that are visible in near infrared continuum filters.

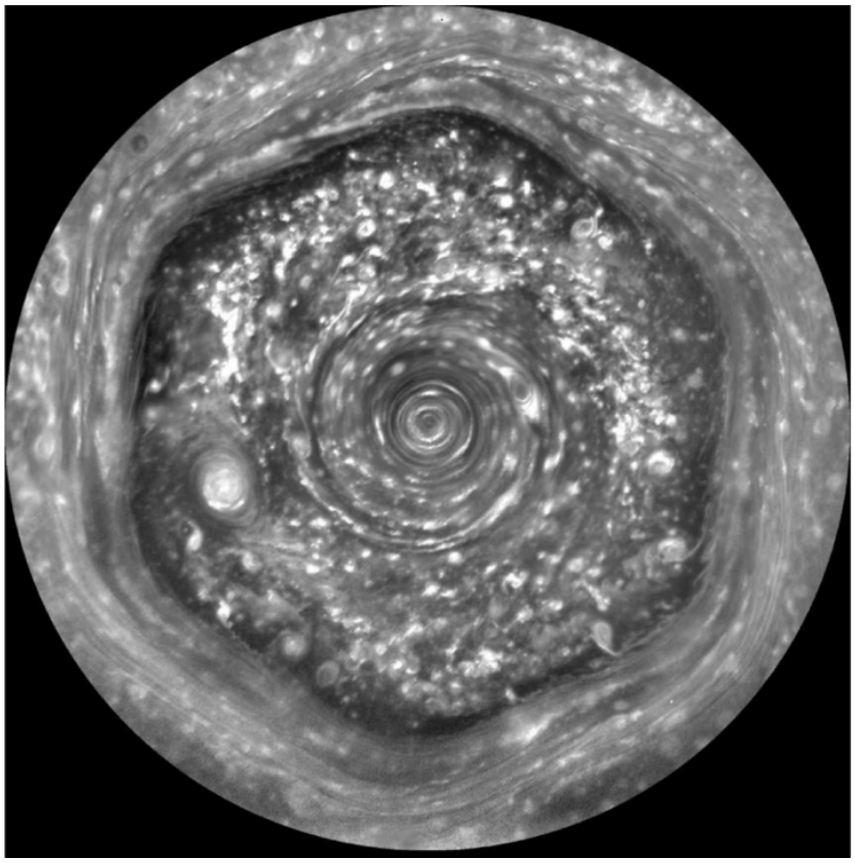

Figure 1.3.4: Polar projection of a mosaic of Saturn's north pole captured by Cassii ISS camera in 2012. The smallest resolved features have horizontal scales close to 30 km. Credits: (Sayanagi, K.M., et al., 2016).

Long term tracking of the hexagon's vertices shows that the hexagon is nearly stationary, with its rotation only slightly delayed from Saturn's average rotation period by a 0.036 m/s zonal velocity difference. Voyager images revealed small clouds moving alongside the outline of the hexagon, showing that the it is associated with a strong eastward jet. Images at visible to near infrared continuum wavelengths show abundant small-scale convective clouds and vortices at the 2 bar layer or deeper in the atmosphere. However the real challenge is to sort out the various contributions from the complex different structures in the polar region and understand how they influence data in various degrees and then attribute the observed features into atmospheric processes (Sayanagi, K.M., et al., 2016).

The main dynamical regimes both on Jupiter and Saturn are somewhat similar except in the po-

lar region. Up to 60° the characteristic banded structure on Jupiter fades way, being populated by countless small vortices. However on Saturn, the organized banded structure is kept up until the very poles and lacks the dynamical regime seen in Jupiter's high latitudinal regions.

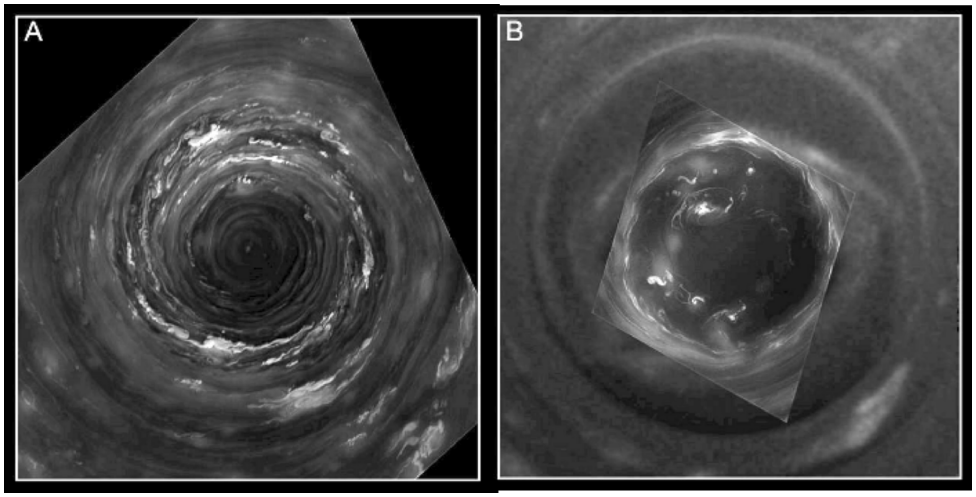

Figure 1.3.5: Polar projections of the north polar region from 87.5 to 90 degrees in 2013 Using an IR continuum filter. Image A is the north polar vortex and image B is the south polar vortex. Credits: (Sayanagi, K.M., et al., 2016).

At the center of the hexagon and on the southern polar region are the cyclonic polar vortices which have been observed to extend down to the 2-bar pressure level and maybe reach even deeper. These polar vortices share morphological and dynamical behaviours to terrestrial hurricanes and tropospheric winds in both vortices exceed 120 m/s within 1 degree of the pole, decreasing steeply to calm winds at the poles. Even though seasons on Saturn means close to 15 years of winter/summer in the polar regions which leads to thermal variations in the atmosphere in these regions, the classical latitudinal thermal structure of cyclonic polar vortices has persisted over each pole since the beginning of the Cassini mission when they were discovered. Although these were incredible breakthroughs brought mainly by the observation from the Cassini spacecraft some questions still remain as to why Saturn displays such intense polar vortices on both poles and what exactly maintains the hexagonal pattern in the north polar region (Sayanagi, K.M., et al., 2016).

1.3.2 History of Saturn's Exploration

Although space exploration of this majestic planet might be shadowed by the famous *Cassini-Huygens* mission, at least three other unmanned probes have made their way past the king of the gods into the realm of Saturn and its numerous moons. Past Jupiter, space exploration becomes increasingly challenging as power supply, communications with Earth facilities and the sheer length of the journey pose some difficulties.

Greater distances from the Sun naturally imply less radiative energy from this source, so solar power is ultimately discarded for far off missions, since the panels would have to be enormous, which would not be efficient for launch costs and overall maneuverability of the spacecraft. A possible solution which has already been implemented in spacecrafts like the Cassini, Pioneers and Voyagers is the use of a *radioisotope thermoelectric generator* which generates power through

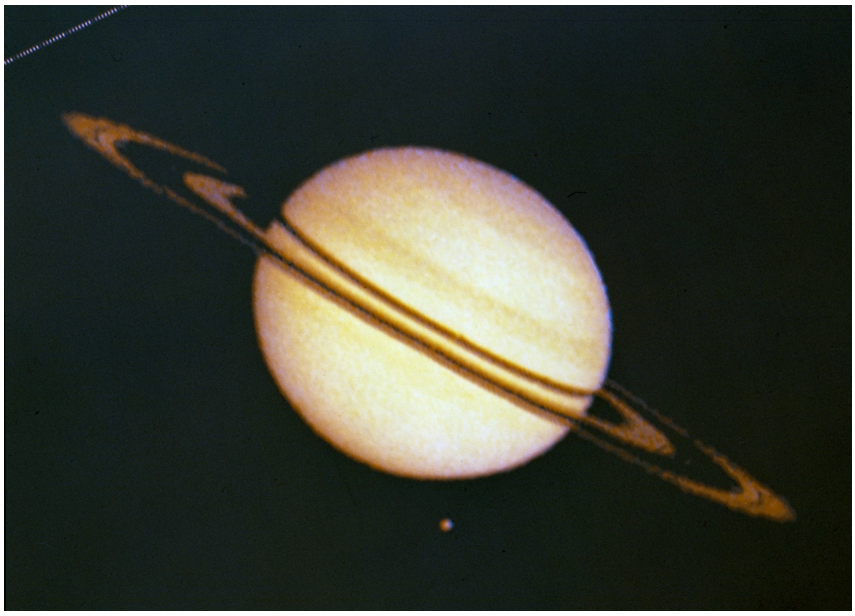

Figure 1.3.6: A global view of Saturn and 'tiny' Titan below it, taken by *Pioneer 11* at a distance of 2,846,000 km from Saturn, in 1979.

the heat released by the decay of a radioactive compound. Despite providing a reliable and long-lasting energy generator the fact that the source is radioactive poses some security issues regarding contamination and interference with the spacecraft's instruments if proper shielding is not provided.

Pioneer 11 was the first man made machine that reached the cronian system in 1979, and provided us with several images, although with low resolution (see fig 1.3.6). The *Voyager* missions also flew past Saturn in 1980 and 1981 returning high-resolution pictures of the planet, its rings and several of its moons. Among their discoveries, gaps between the rings were observed and several new satellites orbiting near or within the rings. The passage of *Voyager 2* through this system was necessary for the spacecraft to reach its next target, Uranus.

The Cassini-Huygens mission

The *Cassini-Huygens* mission is a joint endeavour of NASA, ESA and the Italian Space Agency that was launched in 1997 and it is still running today in its second extension of the nominal mission. Passing through Venus, Earth and Jupiter for gravity assists in order to increase speed and save fuel, the journey to Saturn took approximately 7 years, reaching the cronian system in 2004. Along the journey, in 2000 passing Jupiter, Cassini strongly collaborated with the *Galileo* mission, for the rare opportunity to study the jovian system from two different nearby perspectives at the same time. This cooperation allowed for double monitoring of the magnetosphere interaction with the solar wind.

Approximately six months after orbit insertion around Saturn, it makes its first fly-by of the saturnian moon Titan and releases the Huygens probe for the descent through Titan's atmosphere in which it sampled the chemical composition and surface properties, even taking some pictures when landed on Titan.

This sophisticated spacecraft counts with a number of science instruments:

Imaging Science Subsystem (ISS) – Consists of a wide-angle and a narrow angle digital camera. Takes pictures in visible, near-UV and near-IR light and is equipped with several filters which allow the selection of specific wavelenghths.

Composite Infrared Spectrometer (CIRS) – A spectrometer which collects infrared data to build an infrared spectra of Saturn globally, locally and its moons. Its wavelength range is located between 7.16 and 1000 μm along three different focal planes.

Ultraviolet Imaging Spectrograph (UVIS) – Capturing reflected ultraviolet light in the 55.8 - 190 nm window to study the composition, distribution and aerosol particle content and temperatures of the atmosphere of Saturn.

Visible and Infrared Mapping Spectrometer (VIMS) – Helps in the identification of the chemical composition of the surfaces, atmospheres and rings of Saturn and its moons, by measuring and building a spectre in visible (0.35-1.07 μm) and infrared (0.85 - 5.1 μm) light.

Cassini Plasma Spectrometer (CAPS) – Explores the highly ionized gas near and within the kronian magnetosphere through an electron sensor, an ion mass spectrometer and the ion beam sensor.

Cosmic Dust Analyzer (CDA) – A dust particle detector capable of analyzing dust particles with size similar to that of a red blood cell or smoke particles (μm or smaller). Thus, the instrument is able to determine particle's charge, size and velocity vector.

Figure 1.3.7: This is a coloured image of Titan's surface taken by the Huygens probe after it landed. The two rock-like objects on the bottom of the image are less than 1 metre away from the probe's camera. Credits: NASA.

Ion and Neutral Mass Spectrometer (INMS) – This instrument is mainly concerned with neutral and low energy particles detection to help tracing the chemical composition of the volatile components in Titan's atmosphere and Saturn's magnetosphere and ring environment.

Magnetometer (MAG) – A magnetometer that records the varying strength and direction of the magnetic field throughout the saturnian system. This enables the assembly of 3D models of the magnetosphere of the planet and how it affects its vicinity.

Magnetospheric Imaging Instrument (MIMI) – Equipped with three sensors to detect energetic charged particles (protons, electrons and ions) in the excited gas around Saturn and neutral particles to determine the populations of these species in the kronian magnetosphere and how it interacts with the solar wind.

Radio and Plasma Wave Science (RPWS) – An instrument to cover the emission of Saturn at radio wavelengths and also detect plasma waves. The RPWS enables scientists to detect lightning storms and auroras without imaging them.

Radar – Primarily built to study the surface of Titan, since its thick atmosphere renders visible light imaging obsolete to study the surface of the moon. The radar instrument works much like a sonar and was paramount in the confirmation of the existence of lakes of methane in Titan's surface.

Radio Science Subsystem (RSS) – Using Cassini's high-gain antenna this subsystem sends radio signals back to Earth that, en route, interact with Saturn's atmosphere, its moons or the rings. The received signals are then received on Earth carrying information regarding gravity

fields, atmospheric and ring structure, surface properties, etc.

Cassini's primary mission ended in 2008 but was extended twice to cover a full seasonal cycle of the planet to study the seasonal variability of the planet which is due to end on September 2017 when it will be plunged into Saturn's atmosphere.

Chapter 2

Methods & Tools

2.1 PLIA - Planetary Laboratory Image Analysis

PLIA is an integrated set of programs written in IDL (Interactive Data Language) with a fully operational Graphic User Interface (GUI), developed at the University of the Basque Country which was generously shared with our research group in Lisbon by the Bilbao team, further emphasizing an effort for international collaborations for our studies. It runs on any operating system supported by IDL, although it has only been tested thoroughly on Windows XP and was already extensively used to analyze images retrieved by the Galileo Solid Stage Imaging (Belton et al., 1992) of Jupiter and Venus, Cassini Image Science Subsystem (Porco et al., 2004) of Jupiter and Saturn and hyperspectral cube images obtained by VIRTIS-M (Drossart et al., 2007) onboard Venus Express (Hueso, R. et al., 2010).

The prime focus of this software is the study of atmosphere dynamics by processing astronomical images. This includes, to some extent, planetary navigation which is the assignment of latitude and longitude values to each pixel in an image and it is crucial to almost every scientific measurement in planetary sciences since only with this information we are able to ascertain the position and velocity of atmospheric and surface features on planets and moons. PLIA also enables a number of image correction tools, some dedicated to certain instruments like VIRTIS/VEx, photometric scans and is also capable to compute geometric projection of images into polar or cylindrical maps, which are most useful for cloud-tracking.

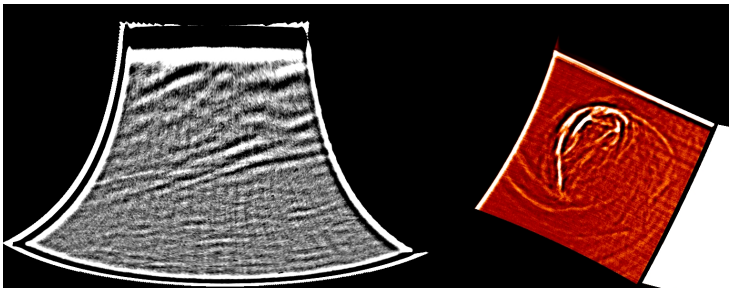

Figure 2.1.1: Examples of the result of geometrical projection calculation on two VIRTIS images. The left image is a cylindrical projection while the image on the right is a polar projection.

It is noticeable in figure 2.1.1 that both images do not show complete maps of Venus, but only a small section, inherited by the original limits of the unprocessed image. This is a necessary step

for cloud tracking which is performed by using another tool of PLIA, both in terms of planetary navigation and image format, which I will discuss in a later section.

Image correction is of the utmost importance, even on calibrated data, to extract useful features for our study. Most images in their 'original' form, that is, untouched by the software do not allow the identification of subtle features as cloud formations and some treatment is required. Often, images contain bad lines and other artificial features of the detector that are removed or diminished when possible. The wavelength range of VIRTIS observations also allows us to select, inside our range of interest, optimal wavelengths where image aberrations are least present. The most common treatment is contrast enhancement which makes most features in VIRTIS images visible and is accomplished mostly with an unsharp mask filter, however more filters are available and sometimes used when appropriate. In addition to the unsharp mask filter, a type of *Butterworth* frequency filter was used mostly for Cassini images of both Jupiter and Saturn, which after verification worked better to increase the contrast in the image without sacrificing image quality.

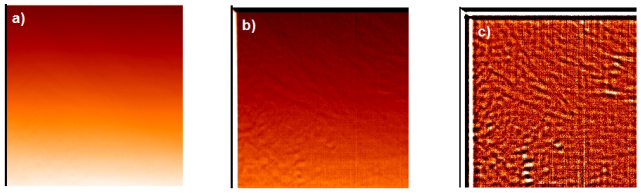

Figure 2.1.2: VIRTIS calibrated images with the 1.74 μm data plane selected. a): Untreated image loaded into PLIA; b): The same image after an unsharp mask filter for contrast enhancement has been used. The visualization range is also narrowed down and some features are starting to be revealed; c): With contrast severely enhanced after several unsharp mask processes, we have an image in which we can properly discern different features.

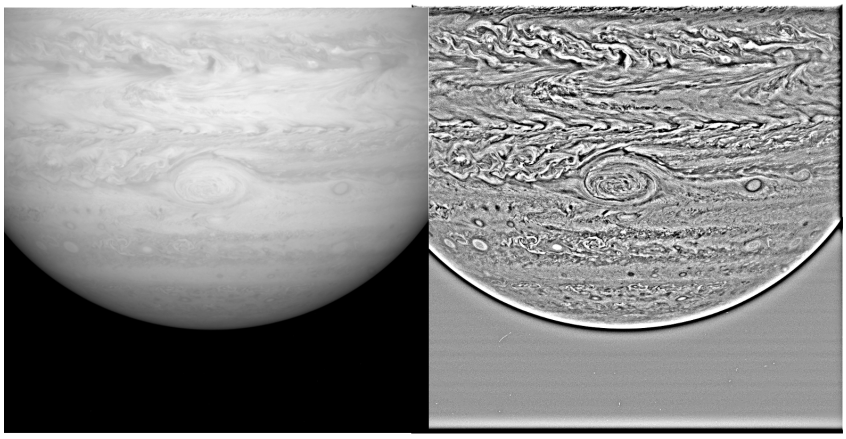

Figure 2.1.3: Cassini ISS images taken with CL1;CB2 filters. On the left we have a raw cassini image of Jupiter. Even though several features are recognizable as Jupiter's atmosphere allows for a clearer observation than Venus or Saturn, we can still improve the image for cloud tracking as is shown on the right image, which has been subject to several butterworth filters while narrowing the visualization range.

2.1.1 VEx/VIRTIS-M

The Visible and Infrared Thermal Imaging Spectrometer onboard Venus Express is an imaging spectrometer directly inherited from a similar instrument onboard the Rosetta mission, with separate telescopes supplying two channels: VIRTIS-M which is a mapping spectrometer working in the visible and in the infrared with a wavelength range specified in figure 1.1.10; VIRTIS-H, a high-resolution spectrometer with spectral range also in the infrared. Another version of the VIRTIS instrument will be part of the payload for the future ESA's mission Bepi-Colombo (Drossart et al., 2007).

VIRTIS-M has the remarkable capability of capturing images simultaneously at different wavelengths and compresses this information in a three dimensional 'data cube'. This way we are provided with a vertical profile of the cloud structure of Venus at different wavelenghts and are able to study the dynamics of the clouds at different altitudes. The VIRTIS data used for this work were gathered in the PSA (Planetary Science Archive) of ESA and are divided in three types: *RAW*, *GEOMETRY* and *CALIBRATED* images.

–*RAW* images are, as the name implies, the raw non-navigated VIRTIS images which have only been subjected to preliminary processing from the telemetry data that comes from the spacecraft that is analyzed by the ground segment of the spacecraft which is tasked with writing the data files that would be made available in ESA's archive as PDS files (Planetary Data System).

–*GEOMETRY* data comprises the geometrical information of the image at hand. It is the file that stores navigation measurements and other geometrical calculations performed during calibration.

–*CALIBRATED* images which have been processed in terms of navigation and some image correction for instrument defects. The data in calibrated images is in physical units (in radiance) and also provide a description of viewing configurations (viewing angles, location, local time and season)

In this study the calibrated data was mostly used since it has already geographical information provided by geometry data and is already corrected for some defects present in the raw images, both in gravity wave detection and in cloud tracking.

2.1.2 VEx/VMC

Images gathered through the VMC instrument onboard Venus Express allowed a complementary study of similar phenomena observed with VIRTIS. However as VMC is more tuned to visible light wavelengths it was mainly used to study the upper clouds of Venus. Regarding particular cases, UV-Blue absorption of the top cloud layers produces distinct features that can be tracked for wind velocity measurements, produced by sulphur dioxide and a still unidentified absorber (Markiewicz, W.J. et al., 2007). VMC images also allow visualization of atmospheric mesoscale gravity waves from which a data base was built and is still being completed as there are still more than 300.000 diferent images to be analyzed from this instrument. Images with positive detections of gravity waves also allow some degree of characterization of the waves, by measuring wavelengths, width, length and altitude (Piccialli, A. et al., 2014).

Unfortunately our analysis of VMC images with PLIA was limited since the built-in navigation algorithm in PLIA is not able to compute latitude-longitude coordinates for each pixel in the image. However we can still extract some information, namely the time associated with each image and the date. For cloud tracking this can be troublesome since image navigation is required for our image correlation software to function. As such, navigated images were provided through

the courtesy of Ricardo Hueso and Javier Peralta so we could perform our studies with different instruments, all the while learning more about the software.

Figure 2.1.4: This is a cylindrical projection of the south hemisphere of Venus as captured by the VMC instrument on the 21^{st} of May of 2006 using the UV window of the camera. The image has a substantial amount of space without any appreciable content. This relates to the entire globe of Venus that is projected in a planisphere but wasn't visible on the real image captured by VMC.

2.1.3 Cassini/ISS

The Imaging Science Subsystem (ISS) is a high resolution 2D imaging instrument. As previously referred, the ISS consists of two separate cameras, the Narrow-Angle Camera (NAC) and Wide-Angle Camera (WAC) which have their boresights aligned, that is, they are pointing in the same direction, parallel to each other, and have distinct *fields-of-view* (FOV) of 0.35 degrees and 3.5 degrees, respectively, to allow a global view of the target (Jupiter and Saturn) and observation of smaller features in detail such as the GRS and Saturn's northern hexagon. Both cameras feature filter wheels with 9 different filters. Some of these are broken down in different wavelengths for a broader selection of wavelength ranges, to track different features in the atmosphere of Jupiter, Saturn and Titan.

During an observation, two filters can be used simultaneously to capture some target wavelength range. In the appendix (tables 7.1, 7.2), the reader can find a detailed list of all the filters of the ISS, filter combinations and specific wavelength ranges.

ISS images from the archive need to be loaded with a specific software called PVOL++. Even though this is an extra step, it is quite useful, since it allows for a quick preview of the images before processing begins, showing relevant information regarding pointing, time and filters used.

With this programme we can choose the image pairs for cloud tracking with greater ease since skipping through the images is much faster than in the planetary science archive of ESA. However the time intervals between images cannot be the same as in Venus. Both Jupiter and Saturn rotate at an incredibly fast rate (∼10h sidereal period). As such, the observable area by Cassini is quite different in successive hours (as the planet rotates we see distinct longitudinal regions) and less than a 30 minutes interval is not enough for our software to perform cloud tracking. Thus we have to extend this period to be as close as a full rotation of the planet, so we can probe the average wind velocity on a jovian 'daily' basis.

After selection, PVOL builds the image files so that they can be loaded with PLIA for image processing. This follows the same directive as in VEx images, where we are primarily interested in removing all the image aberrations we can and maximize the contrast, for the cloud features to be clearly traceable with the cloud tracking software. This is accomplished, as mentioned earlier, with butterworth filters instead of unsharp masking since it proved to yield better results.

Contrary to the VIRTIS images, ISS images were not yet navigated though they have all the pointing information required by PLIA to measure the image.

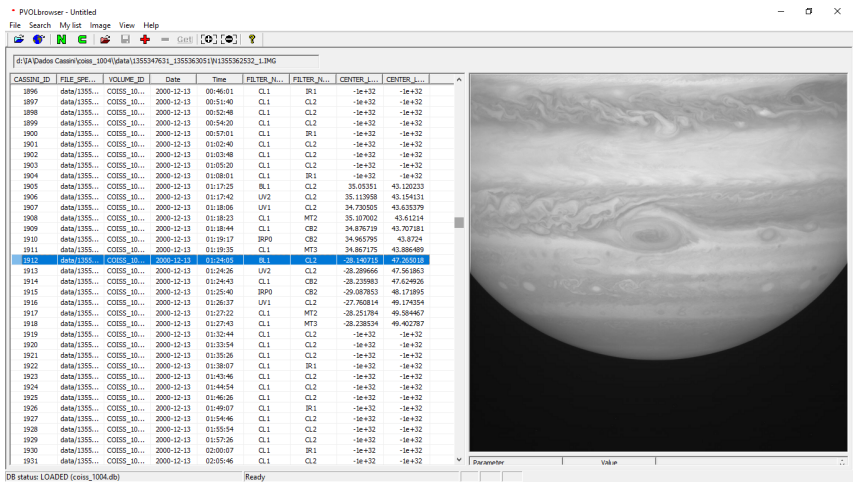

Figure 2.1.5: Display of PVOL++ showing the list of images in the data volume selected. On the right side we have a preview of the image (in this case Jupiter, featuring the GRS) and on the left, useful information about the image. We can also have a quick look at the *Planetary Data System* label of the image, which has a complete list of the image details.

Measuring an image in PLIA produces a grid with latitude and longitude values, computed with a built-in algorithm that performs image navigation. However, as you can see from figure 2.1.6 there's a slight offset between the grid and the planet's outline. The grid offset is irregular, changing with each image. Fortunately this grid is moveable and we can amend this error by moving the grid the required number of pixels. We get this information by zooming in close to the outline, as shown in the crop on the top right corner of figure 2.1.6. Processing with PLIA is then complete after enhancing the contrast and computing the adequate projection to build the image for cloud tracking.

2.2 Cloud Tracking

As a focus point for this work, the image processing steps described above are required, for the most part, to allow us to clearly observe the movement of cloud features on Venus, Jupiter and Saturn.

By analysing a pair of navigated images and knowing the time interval between both images, we are able to probe the movement of cloud features from the first to the second image, thus retrieving a measure for average velocity within that time interval for specific cloud features. By measuring the velocity of several features we can deduct the average velocity of a specific layer of the atmosphere which is selected by the wavelength range of our observations.

The methods for cloud tracking used, allow us to retrieve two wind velocity measurements: zonal wind **u** and meridional wind **v**. Cloud tracking is performed with the aid of a designated software and may be completely performed automatically by some computer algorithm. However, it has been noticed by several planetary sciences research groups that such automatization may lead to some untrustworthy wind velocity results even if they produce many wind measurements (Hueso, R. et al., 2013). Thus, our methods rely on supervised and manual procedures that evaluate wind tracers that are calculated by the software. One such software is an auxiliary tool of PLIA called PICV2.

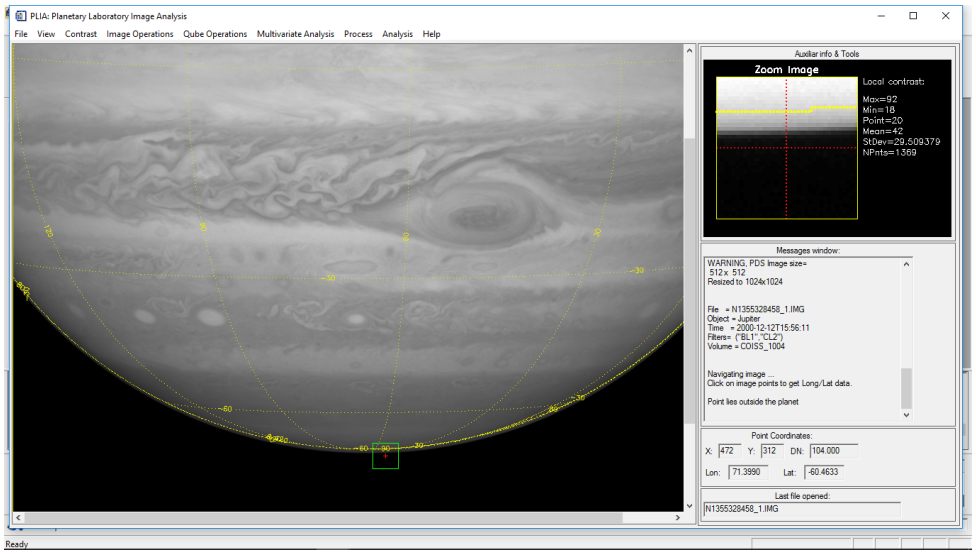

Figure 2.1.6: Navigation of Cassini images with PLIA. After measuring the image, an outline with geographical coordinates is drawn on top of the image and each pixel has a longitude and latitude associated with it. However there's a noticeable offset between the outline of the grid and the planet which needs to be corrected.

2.2.1 PICV2 - PLIA's Auxiliary Tool for Cloud Tracking

The Planetary Image Correlation Velocimetry is, as PLIA, an IDL based program that is housed inside PLIA's repertoire. Below we can see an example of the software interface at startup after loading an image pair.

The images must be navigated, properly named and spaced in a time interval between 30 min-

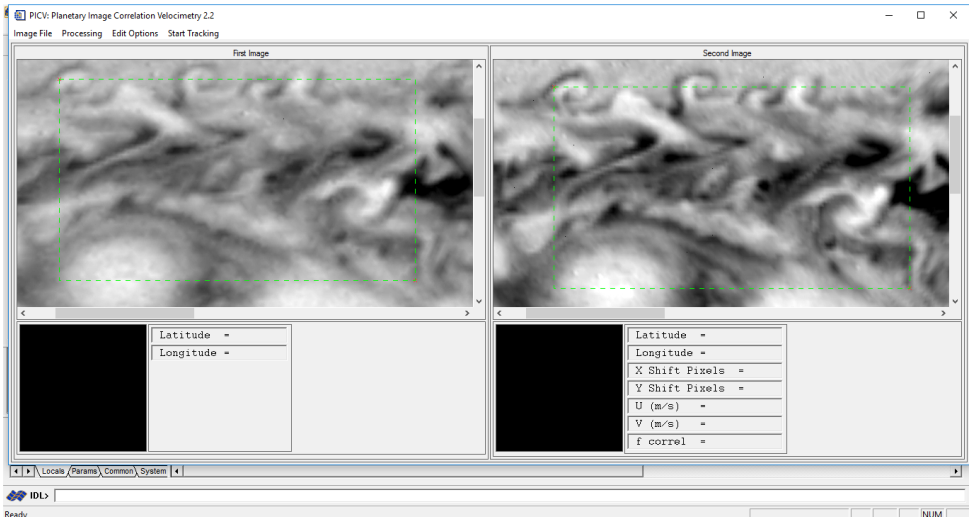

Figure 2.2.1: The interface of PICV2 after loading an image pair. A green outline is also visible which is the area box selected in which cloud tracking will be performed. The image pair selected is a close-up of Jupiter by Cassini during its flyby in 2000.

utes to 2 hours (for Venus images) in order for PICV2 to calculate wind vectors correctly. For the giants, as they rotate faster, an interval with the full rotation period is required to trace cloud movement in similar longitudinal regions of the observable 'surface'. Image processing and contrast enhancement performed previously by PLIA is essential for PICV2 to adequately

recognize different atmospheric patterns in the clouds to allow the image correlation algorithm to associate the cloud patterns appropriately.

This software operates by applying an image correlation algorithm between both images to recognize cloud patterns (through image contrast shapes) and measures the pixel displacement of these features from the first image to the second. Using the information provided regarding the time and geometry associated within each image, PICV is able to compute the component of winds described above and draw wind vectors in the second image.

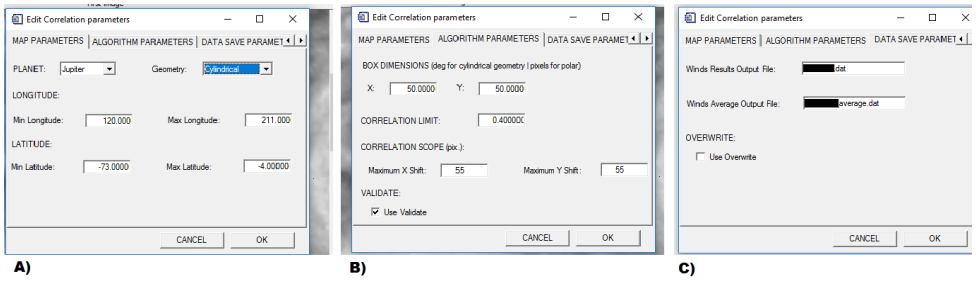

Figure 2.2.2: Showcase of PICV2 correlation options to fine tune before performing cloud tracking. Each of these features is carefully selected for optimal results. Panel A lets the user provide information regarding mapping of the image and the target planet. Panel B allows the user to choose an appropriate correlation box size along with a correlation limit for validation of wind vector and the maximum feature displacement (in pixels) between the image pair that can be measured. Panel C manages where the results of cloud tracking will be exported to. PICV produces two files, one with every wind vector measure and another with a statistical average along a latitudinal line.

The area box (green outline in figure 2.2.1) will be filled with correlation boxes with a customisable size that should be appropriate for the cloud features present in the area selected during cloud tracking, until all available space in the area is occupied. For PICV to produce reliable values, we must provide the cartographic limitation of the image (latitude and longitude range of the image) and if the images are projected in a cylindrical or a polar perspective as this changes how the software's algorithm works (as seen in panel A of figure 2.2.2).

As the study area is filled with correlation boxes we must be sure that their sizes are suitable for the shapes present in the images. For example, if the cloud features in the area selected have mostly elongated shapes we ought to establish more rectangular (stretched) boxes to completely capture such cloud features. Also, depending on the typical wind velocity of the target we can select the correlation scope for cloud tracking by applying limits to the horizontal and vertical shift (displacement) that is recognized as cloud movement (see in panel B of figure 2.2.2). Note that the values inserted have different meanings depending on the geometry chosen, where we selected the size of the boxes in degrees if we are taking the cylindrical projection and in pixels if we are dealing with images with polar projections.

Finally we must manage where the wind results will go to. They are stored in data files that are readable by a standard text editor software. The wind average output file (panel C of figure 2.2.2) is a statistical average of the wind velocities obtained along an horizontal line, thus representing the average wind in a latitudinal zone. In spite of the usefulness of this file for a more comprehensive view of zonal wind velocity of that latitudinal region, the data in this file has not any value for cloud tracking using polar geometry since the winds along an horizontal line in this projection are not statistically relatable due to the constant change in latitude in this direction.

As we begin cloud tracking, another window shows up which will allows us to supervise every wind vector that is measured by PICV.

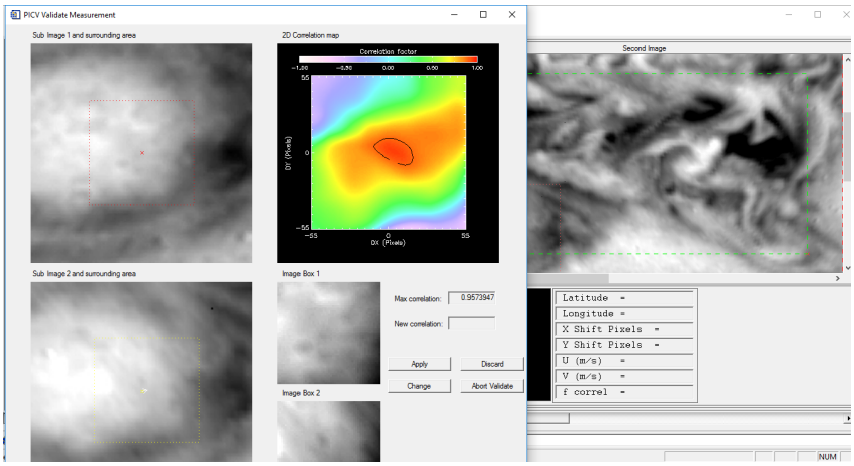

Figure 2.2.3: PICV2 interface during cloud tracking. The program offers information on each correlation box and their surrounding areas with wind vector drawn, a correlation colour map and the highest correlation value found.

This interface (see figure 2.2.3) shows the relative correlation boxes on each image and their surrounding areas and enables us to evaluate which cloud features are being compared by the algorithm and where. Along with a cropped section of the images there is also a color map showing how the correlation values vary within the images. A good wind measurement is obtained when this correlation map shows a sharply localized zone where the correlation values are high (between 0.7 or better depending on the images' quality). Given all the information as seen in figure 2.2.3 we can validate the wind vector measure or decline if we are not satisfied. Either way the process may continue with our supervision in every measurement or we can 'abort validation' and let PICV perform cloud tracking validating measurements based on our previous validation choices and on the criteria selected before starting cloud tracking.

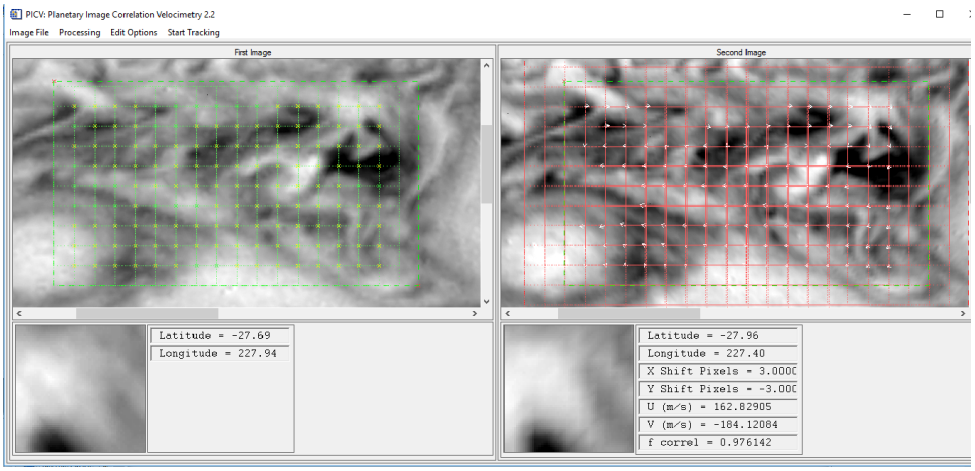

Figure 2.2.4: The final result of cloud tracking performed by PICV2. The small white arrows in the red grid are the calculated wind vectors. Note that the study area is not fully occupied with boxes as the area is filled until there's not enough room for another row of correlation boxes of the chosen size.

As cloud tracking in the selected area is finished, the program looks something like figure 2.2.4. The wind results are stored in the appointed data files that can be used for plot building. It is possible to perform cloud tracking again in the same image pair, focusing on a diferent zone to cover other features in more locations or on the same area with different parameters selected for cloud tracking.

2.2.2 Error Handling

Measurements performed with PICV2 have, like all measurements, errors associated with them. Ignoring instrumental errors that are inherent to each image and completely unpredictable, there are still some sources that require careful attention so that our results are scientifically accurate.

Image navigation is performed individually on each image and the precision of these calculations has increased over the years, with the help of SPICE kernels which I will discuss later on this chapter. But as these intricate calculations rely on previous information on planetary body shapes, sizes and time values, navigation of our targets might be inaccurate by some pixels in the image and more importantly, generate a 'mapping' difference when both images in the pair are navigated and geometrically projected. This error in geographical coordinates between both images in a pair naturally induces an error when PICV2 computes the displacement of atmospheric features to measure the velocity components not to mention the error in the position of these features.

The time interval between the images selected for cloud tracking is computed as the difference between the time dates registered on both images which come from a calculation based on the onboard spacecraft clock. Even though most spacecrafts are equipped with atomic clocks which are extremely regular, the transformation to other time coordinates can also generate some temporal error. This will translate in a slight deviation on the velocity values, since PICV2 uses the date and time provided on the name of both image files to compute appropriate velocity measurements for each target.

As described above, PICV uses correlation boxes on which it recognizes cloud patterns and their displacement from the first to the second image. The size of the boxes is chosen by the user and can be adjusted to different dimensions within the same image pair that is being analysed. As the image correlation algorithm is dependant on the size of this box and on the vertical and horizontal displacement in each measurement, tied to image resolution, it is also a source of errors on wind vectors that are calculated.

Given these general considerations on the main contributers for the errors in wind velocity measurements, we now look closely to how the error can be computed. In an approximation, PICV computes the wind velocity vectors, as pointed out, by measuring the displacement of cloud features within the given time interval between the image pair:

$$u = \frac{\Delta X}{\Delta t} \tag{2.1}$$

$$v = \frac{\Delta Y}{\Delta t} \tag{2.2}$$

Where ΔX and ΔY are the longitudinal and latitudinal displacements of the feature (in meters) and Δt is the time interval between images (in seconds). So the error of our measurements are dependant on the latitude and longitude coordinates attributed to the projected images used for cloud tracking and the precision of the time keeping between the images. When a cylindrical or polar projection is performed with PLIA, we are able to choose the resolution with which the projection will be carried out which is given in degrees/pixel. As we required this error to be in meters, some simple conversions are required like passing the degrees to radian units and then accounting for the radius of the target observed plus the height of the atmospheric layer of interest:

$$\delta s = \delta\theta \ \cdot \ (R + h) \tag{2.3}$$

Where $\delta\theta$ is the resolution of the projected image in radians, R is the radius of planet and h is the height of the atmospheric layer. As the precision of the clocks onboard the space missions from which data was retrieved is on the order of the milisecond, we can discard the temporal error as insignificant compared to the displacement error brought by the spatial resolution. Hence the errors in wind velocity δw_v are calculated according to (Peralta, J., 2008):

$$\delta w_v = \frac{\delta s}{\Delta t} \tag{2.4}$$

To handle these fluctuation sources in our results one simple but effective technique that can be used is the application of data binning through a weighted average of the data points generated within some latitudinal range. Given, for example, all the data points retrieved with PICV2 between $22.5° - 27.5°$ latitude and perform the following calculation to get the weighted average within the selected latitude interval ($WA(V^{obs})$):

$$WA(V^{obs}) = \frac{\sum_{i=1}^{n} V_i^{obs} \sigma_i^{-2}}{\sum_{i=1}^{n} \sigma_i^{-2}} \tag{2.5}$$

Where V_i^{obs} is the i^{th} data value we want to average, σ is the error associated with each individual point. Though quite simple, this procedure is powerful as it negates the effect of obvious outliers in our data, leading to better results. Examples of data binning are presented on the results section of this thesis.

2.3 Atmospheric Gravity Waves

2.3.1 Gravity Waves Detection

During observations carried out by both VMC and VIRTIS instruments onboard VEx, many atmospheric gravity waves were observed. Their detection and further characterisation is another useful tool for analysing the dynamics of the venusian atmosphere and to understand how these waves are created and how they influence the atmosphere.

This work intends to follow up on the studies performed by (Peralta, J., et al., 2008) and (Piccialli, A. et al., 2014) by detecting atmospheric gravity waves in non-previously observed VIRTIS and VMC images acquired for this purpose.

Images obtained from VMC allowed the visualization of the global upper cloud formations in Venus and a detailed look at smaller, localized features in the clouds through the different filters of the camera (UV, VIS, NIR1 and NIR2). Each image was manually analyzed with three main concerns: the existence of atmospheric gravity waves, whether or not the images had any defects and how severe they were. A data base was then built in excel to comprise this information in a clear, easily readable way, along with a preliminary statistical analysis of atmospheric gravity wave detection on each data volume.

Atmospheric gravity waves appeared in the images as a sequence of crests above the cloud layer with various morphologies and lengths. Images with at least 3 visible crests in a row were positively classified as having atmospheric gravity waves.

However, such features were not so clear in some images or had another unrecognised but interesting feature. As a trustworthy confirmation was not possible, these images were tagged with a 'doubt' flag classification in the excel sheet. All doubts are registered in a text file, stating very briefly where the uncertainty arises, in order for an easier verification as to whether or not the

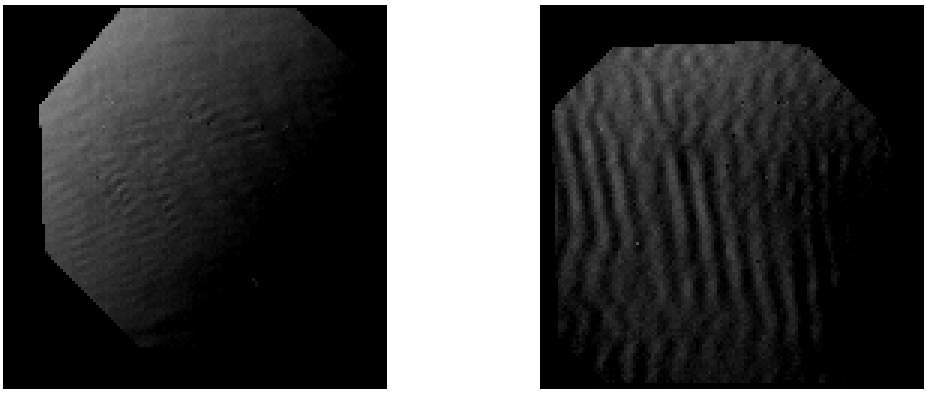

Figure 2.3.1: Atmospheric gravity waves on Venus as observed by the VMC instrument. The left image was taken with the VIS filter and the right image was taken with the NIR2 filter, showing the appearance of atmospheric gravity waves at different wavelengths.

image actually shows waves. Unique features were also highlighted in the same file for further reference and study. And of course, images without any distinctive feature beared a negative classification for atmospheric gravity waves.

To enhance the data base, a section describing image artifacts and aberrations was added and each image was also given a defect classification based on how much the aberration affected the overall image. This would range from no artifacts in the image to a completely corrupted one where only noise was observable.

The terms used were:

– "No" where the image presented no visible imperfections or nothing stood out in the image as an aberration (Figure 2.3.2);

– "Mild" where the image demonstrated small artifacts or incorrections that didn't influence the overall examination of the image for the detection of gravity waves (Figure 2.3.3);

– "Moderate" where the image showed an overall noise signature throughout the image that degraded image quality and made the detection of waves harder or a higher amount of artifacts compared with "Mild" defect classified images (Figure 2.3.4);

– "Strong" where the image was completely or almost completely covered with noise or artifacts that significantly degraded its quality. From these images it was impossible to detect any kind of feature on the atmosphere of Venus (Figure 2.3.5);

Detection of atmospheric gravity waves with VIRTIS required a more careful approach since much more wavelengths are available and gathering the images is a much slower process along with a required contrast enhancing step, opposing VMC images, which no image treatment was required for the purpose of atmospheric gravity wave detection.

As the PSA allows us to browse the images that were subject to some treatment, a preliminary screening was performed without the need to download the images since VIRTIS data cubes have to be gathered individually, which can potentially waste a lot of time. By scanning the images within the archive, those which showed signs of a possible existence of atmospheric gravity waves were collected for further processing with PLIA, using the same steps as described above for a confirmation on the existence of such suspected wave packet on selected wavelengths (1.74 μm, (2.2 - 2.3)μm and 300-800 nm).

As with the VMC images, it was also included an image defect classification with equal qualita-

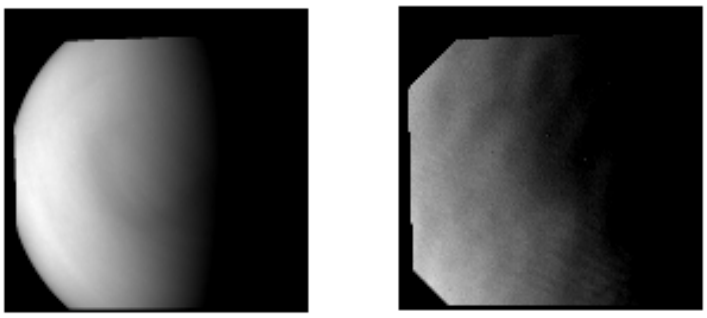

Figure 2.3.2: VMC images with no noticeable defections or aberrations.

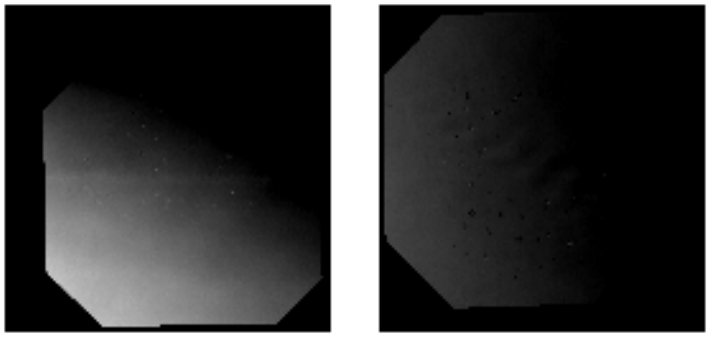

Figure 2.3.3: VMC images with a mild defections or aberrations.

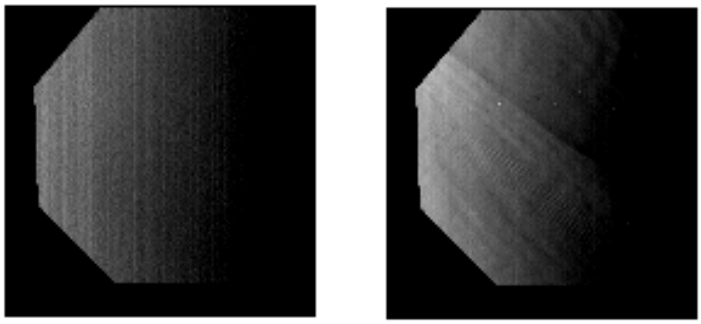

Figure 2.3.4: VMC images with a moderate defections or aberrations.

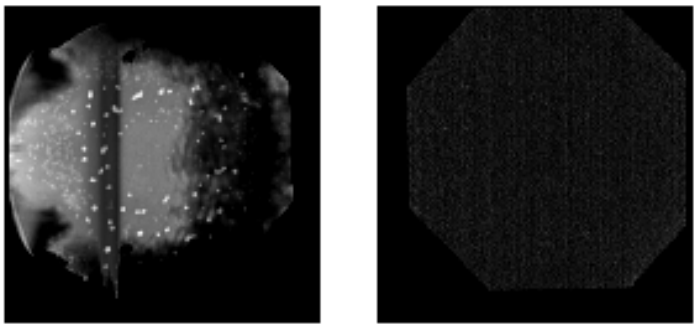

Figure 2.3.5: VMC images with a strong defections or aberrations.

tive classes (No, Mild, Moderate, Strong). However, please note that since we are dealing with distinct instruments, image aberrations produced by it will not be exactly the same.

Frequently, one of the target wavelengths, both in the IR and visible channels, only shows noise

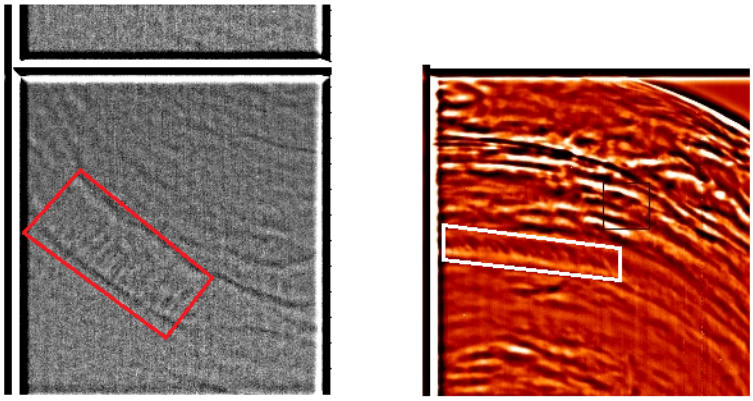

Figure 2.3.6: Examples of atmospheric gravity waves on VIRTIS images. The left image was captured using VIRTIS-V channel and is centered at a wavelength close to 500 nm. The right image is from the VIRTIS-IR channel at a wavelength of 1.74 microns. Both features were highlighted for easier visualization.

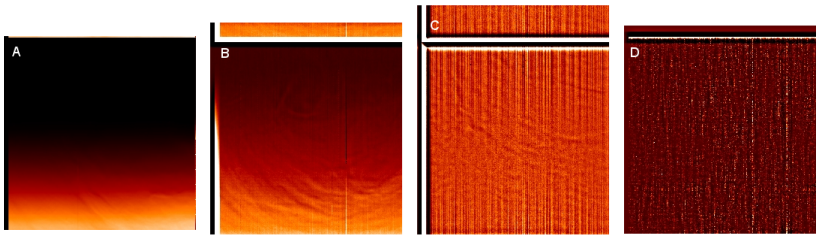

Figure 2.3.7: A: VIRTIS image example without defects. However, different wavelengths within this data cube might shape differently in terms of aberrations, hence our classification apply only to our target wavelengths; B: VIRTIS image classified with 'mild' image defects.; C: VIRTIS image classified with moderate aberrations.; D: If a VIRTIS image behaves like this example, showing only noise or suffers from other instrumental failures in all our target wavelengths, it is classified with strong defect classification since no analysis can be performed.

while at another wavelength we clearly observe features in the atmosphere of Venus. At such times the classification is attributed to the worst case observed.

2.3.2 Gravity Waves Characterisation

Once atmospheric gravity waves have been identified, the best candidates were chosen for wavelength and phase velocity measurements. To accomplish this, image navigation is required in order to measure the distance between two points on the observable cloud layer. This rendered wave characterisation impossible for VMC images in this thesis, even though a much larger number of waves were identified. However this was possible with VIRTIS imagery since the geometry file which provided proper navigation was attached to the images used.

Wavelengths of atmospheric gravity waves are measured, as illustrated in figure 2.3.8, by selecting two consecutive crests of a wave-train, determine their latitude-longitude coordinates and then performing the calculation above. In the equation in figure 2.3.8 is important to note that for a correct measurement of the wavelength of gravity waves on the atmosphere of Venus, we

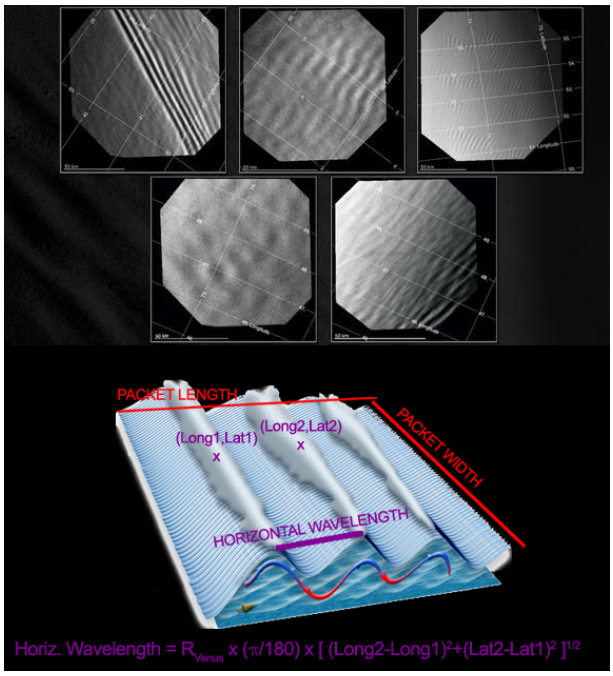

Figure 2.3.8: Schematic that illustrates how wavelengths of atmospheric gravity waves can be measured, provided the image is navigated. It also shows some examples of wave features on which these calculations can be performed. Credits: Private communication, Javier Peralta (JAXA - Japanese Aerospace Exploration Agency).

need to account for not only the radius of the planet but also the height at which we are probing. That ranged from 48 km for the lower clouds and 66-70 km for the upper clouds. This equation is a general formula to measure the distance between two points on the surface of a planetary body and was also used to compute a preliminary phase velocity of the wave-trains observed with VIRTIS.

For an accurate measure we must ensure that the line that separates both points is perpendicular to the crests in order to guarantee that we are measuring the smallest distance between the crests. As this was performed manually and by eye, special care had to be taken to ensure that the measurements were performed as thoroughly as possible. Hence, various measurements were made across a line that followed the second crest, from which the smallest wavelength value was taken (see figure 2.3.9). This is highly reliant on image resolution as visual distinction of the wave crests must be clear, leaving some images aside, where gravity waves were spotted but measuring conditions were inadequate.

To calculate the (general) phase velocity, latitude-longitude values were measured for notable points on the wave trains within a pair of images, preferably with one hour time interval between them. The image points selected need to target the exact same feature on both images otherwise phase velocity calculation won't be correct. As this is limited by image resolution and the ability to select the right pixel in each image which target the same feature, several points of interest are selected on each image and then an average of all measurements within the same wave train is carried out for a more comprehensive phase velocity result.

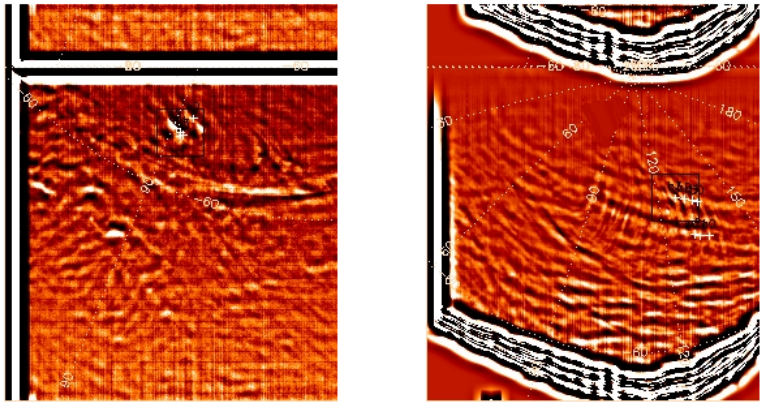

Figure 2.3.9: VIRTIS navigated images with measured points in observable atmospheric gravity waves. The location of the points measured is associated with wavelength and general phase velocity measurements for the left and right images respectively.

2.4 SPICE - An Observation Geometry System for Space Science Missions

For cloud tracking to adequately perform and give out useful results, high precision navigation is absolutely necessary so we can properly trace the dynamics of the different bodies of our solar system and study the evolution of their atmospheres with great precision. As on Earth, all planets have a geographical, latitude-longitude coordinate system, each with a specific definition of the origin of that reference frame (the 0 point in latitude and longitude).

A reliable method to do this is to have some feature on the observable surface of the planet that rotates synchronous with planet's rotation period. This is easily achievable if we can locate some surface feature and use it as the origin of our reference frame as in the case of Mars where the its prime meridian (meridian with 0°) is defined as the center a 500 m diameter crater called *Airy-0* on Mars' surface, (Archinal, B. & Caplinger, M., 2002).

However for a planet completely covered in a gaseous and fluid envelope, choosing a static feature on the atmosphere is an almost impossible task, even in long lived structures like the GRS since it drifts continuously in spite of its latitude remaining remarkably stable over its years of observation.

As such, there's an established coordinate system for the gas giant, namely the System III coordinates for Jupiter and Saturn. In short this system rotates with the planet at an agreed upon spin period (sidereal System III spin period, 1965) and the prime meridian in Jupiter is defined in terms of the central meridian longitude (i.e. Earth-Jupiter vector) on a specific date in 1965.

If we have the basics for the coordinate system of the planets, we can then map every point on the observable surface of the planet. This can prove quite challenging since all kinds of images are available, being them close-ups on small local regions or a global view where the outline of the planet is visible. Thus we have to know the exact position of both the planet and the spacecraft both in space and time in order to adequately assign latitude-longitude coordinates to the image at hand. One system that helps in this regard is SPICE.

SPICE is a system developed by NASA's Navigation and Ancillary Information Facility (NAIF) to assist scientists in planning and interpreting scientific observations from space based instruments onboard planetary spacecraft like VEx or Galileo and it is also used in engineering tasks

associated with space missions.

Though it can be acknowledged as a programming language on itself, it was originally built around a FORTRAN work frame and then adapted to C, IDL and MATLAB programming languages and is currently being expanded to a Python-like language. Hence, it uses these four widely known forms of code as a benchmark for its own specific functions and structures. This aspect makes SPICE a highly adaptable and even customisable system to the user's needs, widening its usefulness for the scientific community.

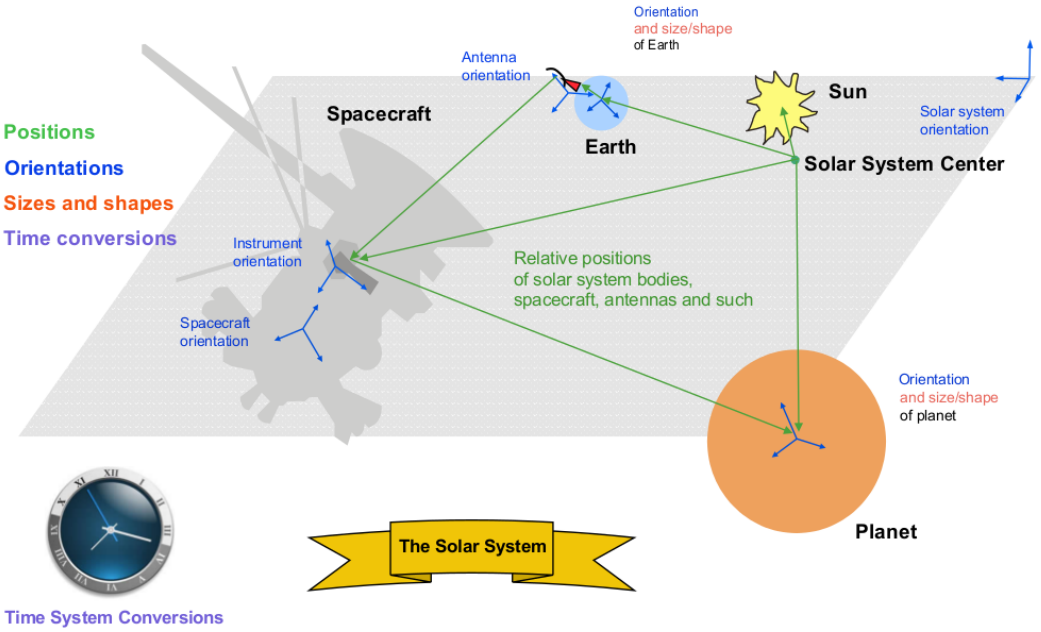

Figure 2.4.1: Solar System Geometry schematic showing all the reference frame in play when we account for the different coordinate systems of the target (planet or moon) and observer (ground-based or spacecraft)

This system's main focus is on solar system geometry, concerning with aspects illustrated in figure 2.4.1. Knowing with great accuracy where and when a specific object is in outer space is no easy task. The position of all astronomical objects constantly changes and is subject to many different interactions that most of the time don't follow simple models and for precision's sake, common approximations astronomers perform in their calculation cannot be applied.

The position of all objects concerned is then, the first aspect we need to address, namely the relative positions between solar system bodies, spacecrafts and their instruments, antennas and other ground-based observation sites and standard reference frames for the solar system as a whole (such as the J2000 frame). Orientations of some of these object come next as they comprise pointing information of telescopes, antennas, spacecrafts and instruments onboard so we may know what we are looking at exactly, from a captured picture of a spacecraft instrument for example. For planetary science studies, most objects are extended sources, i.e they have dimensions and shapes, which is particularly important for image navigation to correctly obtain geographical coordinates on a planet/moon's surface. Finally all this information has to be on the same time frame, or the time lapses between different objects needs to be accounted for. For example, if we are taking the position of Jupiter as observed from Earth the light time from the target to the observer is significant in some precision measurements and various time systems like UTC or ephemeris seconds past J2000 have been tweaked over the years as Earth's orbit and rotation periods are perturbed by other movements (nutation and precession for example).

SPICE is able to gather all this information and perform calculations using all this data to retrieve important information such as altitudes, planetary coordinates, lightning angles, local times, etc. To perform said calculations, SPICE makes use of *kernels* which are a type of file written specifically to be read by SPICE's functions and application programs and have all the necessary data such and planetary bodies radii, instrument orientations, ephemeris data and more. Some are more generic which have basic information regarding leapseconds (seconds added or removed when keeping time throughout the years) while others are specific to an instrument onboard a spacecraft, namely frames and pointing data.

This system was born in 1982, when better archival treatment for space science missions data was necessary for scientists to fully and correctly interpret data returned from spacecraft instruments. Though a primeval form of SPICE was attempted for *Voyager* data, the first official, even if partial, use of SPICE technology took place on the Magellan mission to Venus and due to its success, the SPICE approach was tested on the Mars Observer and Galileo mission projects to verify if this system should replace the tools available at the time (Supplemental Experiment Data Records system). Although the SPICE system was focused on assisting scientists with data analysis tasks and archival purposes, the space exploration community realised that this system could also be used for mission design, operations and observation planning. Thus, SPICE has become the number one tool for managing data for space science missions as well as planning for future missions, (Data Management and Computation,, 1982; Greenbelt Md. & Kieffer, H., 1983).

As SPICE kernels are continuously being updated and the planetary sciences community routinely makes use of this system and keeps it reliable, planetary image navigation is achieved with unprecedented accuracy when using SPICE data. The only drawback of such a powerful system is that it requires some non-trivial programming which demands familiarity with SPICE. Fortunately, the NAIF team offers at least once every year a three-day SPICE training class which covers all basic aspects of SPICE, all the while giving tools for each student to carry on on their own after training. Also, every function, application program and almost all aspects regarding SPICE systems are carefully and thoroughly documented so even complex tasks can be performed once the user goes through the necessary guides. On September of 2016 we were given the opportunity to attend one of these classes at ESAC (European Space Agency Center), near Madrid where we were given a SPICE hands-on experience. Much of the lessons given during this class were carried out in greater detail in the following months after training. The next step was then to apply those skills to perform image navigation at IA using our own programs, contributing to our team's strength.

2.4.1 Applications of SPICE

As previously stated, the true power of SPICE comes from the precision in which image navigation is performed, which in turn allows scientists to obtain much better results for their measurements, even from ground-based observations.

With good navigation, we can perform accurate geometrical projection, since every pixel has an appointed latitude and longitude coordinate with SPICE.

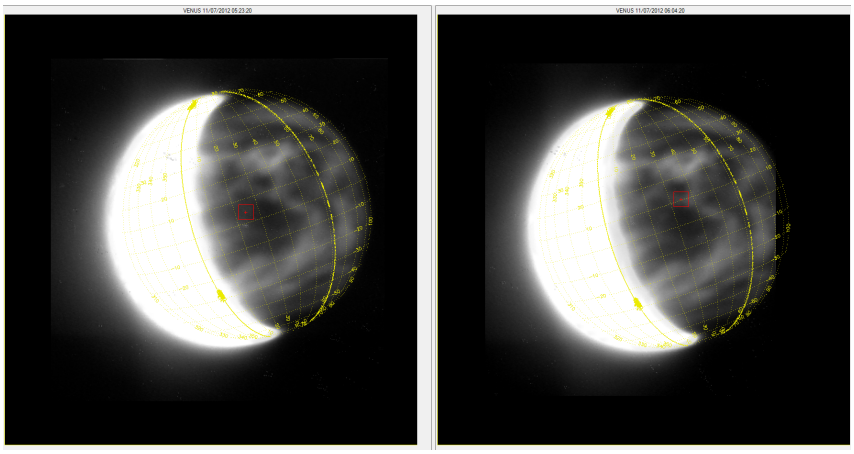

Figure 2.4.2: An image pair of ground-based observations of Venus that have been navigated with SPICE kernels, forming a grid which assigns proper geographical coordinates to each point in the image with great precision.

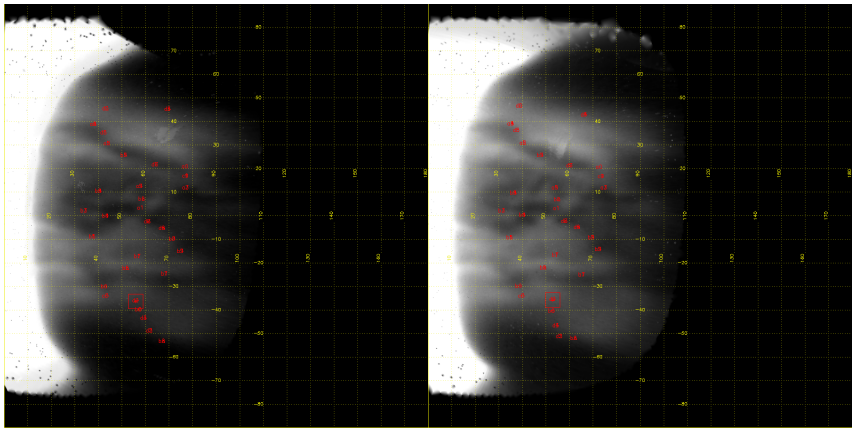

Figure 2.4.3: Cylindrical projection of the images in figure 2.4.2 with manually marked tracers and the SPICE navigation grid.

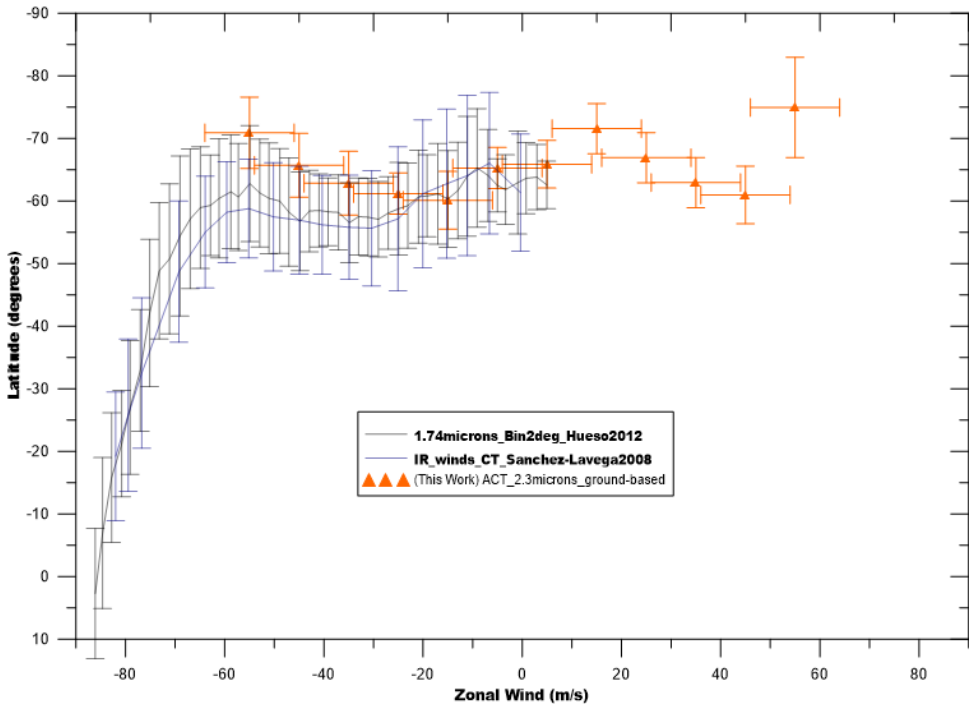

Figure 2.4.5: Cloud tracking results compared with manual cloud tracking on ground-based images of Venus navigated with SPICE. The level of precision between ground and space based observation is quite similar and with SPICE navigation we are also capable of capturing wind variability.

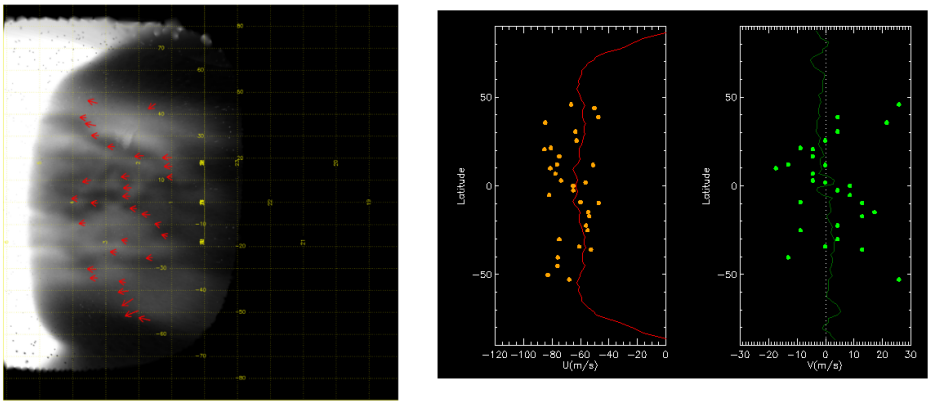

Figure 2.4.4: Wind vectors, tracked with a manual cloud tracking software that uses SPICE kernels for navigation and on the right, the zonal and meridional wind values obtained from the manually tracked tracers. The continuous line on both graphics is model of the average wind velocity for each component.

From figures 2.4.4, 2.4.5 we can see that our zonal wind points calculated from the tracers, capture the variability of the winds on Venus and follow to some extent previous, spacecraft results, showing that with SPICE navigation it is possible to retrieve trustworthy results for ground-based observation which are much easier and cheaper to obtain than any planetary space mission.

Chapter 3

Observations

3.1 Venus Express

3.1.1 VIRTIS

VEx orbit	Qubes pairs	Date (yyyy-mm-dd)	Time Interval (min)	Latitude Range
352	VI0352_06 / VI0352_07	2007-04-07	30	60°S-80°S
473	VI0473_07 / VI0473_09	2007-08-06	60	60°S-90°S
474	VI0474_00 / VI0474_02	2007-08-07	60	60°S-90°S
793	VI0793_02 / VI0793_04	2008-06-21	50	60°S-10°N
2705	VV2705_06 / VV2705_08	2013-09-15	60	35°S-90°S
2927	VV2927_04 / VV2927_07	2014-04-25	60	70°S-5°S
2936	VV2936_00 / VV2936_02	2014-05-04	60	60°S-90°S
2939	VV2939_05 / VV2939_07	2014-05-07	60	70°S-5°S
2944	VV2944_00 / VV2944_02	2014-05-12	60	30°S-90°S
2944	VV2944_01 / VV2944_03	2014-05-12	60	90°S-30°S
2944	VV2944_04 / VV2944_06	2014-05-12	60	90°S-30°S
2944	VV2944_05 / VV2944_07	2014-05-12	60	90°S-30°S
3034	VV3034_00 / VV3034_01	2014-08-07	30	70°S-10°S
3094	VV3094_00 / VV3094_01	2014-10-02	30	75°S-5°S

Table 3.1: VEx/VIRTIS observations whose image pairs contained suitable features for valuable wind vector measurements with PICV2. Listed in this table are the number associated with the VEx orbit, the name of the data cube, date, time interval and an approximate latitude range of the pair. Several wavelengths were targeted including UV (close to 365 nm), 400 nm, 540 nm, 1.74 μm and 3.7 μm.

For Venus, we were interested in specific wavelengths in the IR range, mainly 1.74 μm, 2.3 μm, 5 μm for polar regions and the entire VIRTIS-M channel with a wavelength range illustrated in figure 1.1.10. Because of the highly elliptical orbit of the VEx spacecraft, reaching pericenter close to 80°N of Venus, and since the integration time of the hyperspectral images from VIRTIS is substantial (10-15 min), only the south hemisphere could be covered by this instrument (Peralta,

J., et al., 2008). For the purpose of this work, as we were interested in retrieving latitudinal profiles of the zonal wind, images from many different dates were selected, which also allows us to pursue results for the average winds on Venus over an extended period of time.

One aspect worth noting here is that, shorter wavelengths were used for the poles than expected because the frames in these data cubes close to $5\mu m$ only contained noise, hence only frames that maximized the contrasting features of the southern polar vortex were chosen.

Regarding gravity wave detection for the reasons explained earlier in section 2.3, only a month of observations with this instrument could be covered. As this was intended as a continuation of the work by (Peralta, J., et al., 2008), all images within August of 2007 were analysed, spanning 16 orbits and over 370 different images. Atmospheric gravity waves were observed at our target wavelengths in both VIRTIS channels and other extra wavelengths that provided a more clear view of the feature.

3.1.2 VMC

Although the complete collection of data from VMC is available in PSA, these images are not navigated and PLIA cannot perform navigation on these images with its algorithm. Though a program was developed based on SPICE that computes geographical coordinates of the center and corners of the VMC frame observed at a designated time, it is not enough to appoint a latitude and longitude coordinate to each pixel in the image, giving us limited information of the picture. Fortunately, two pairs of VMC images that cover the entire southern hemisphere were navigated and granted to us by Ricardo Hueso which were then cloud tracked with PICV2:

VEx orbit	Image pairs	Date (yyyy-mm-dd)	Time Interval (min)	Latitude Range
V0030	V0030_0099_UV2 V0030_0117_UV2	2006-05-20	47	90°S - 0°S
V0031	V0031_0000_UV2 V0031_0040_UV2	2006-05-21	58	90°S - 0°S

Table 3.2: VEx/VMC observations in the UV (365 nm) were cloud tracking was performed. Image navigation and cyllindrical projections performed by Ricardo Hueso.

As opposed to the detection of gravity waves with VIRTIS, a facilitated access to a large number of VMC images was possible, hence almost a full year of observations was monitored for atmospheric gravity waves, starting in orbit 2448 (2013-01-01) all the way to orbit 2799 (2013-12-19). These include observations on all four VMC filters at the designated wavelengths (figure 1.1.9).

3.2 Cassini/ISS

3.2.1 Jupiter

As Cassini flew past Jupiter for a gravity assist in order to reach its destination, sparing precious fuel, scientists seized this opportunity to not only test some of the instruments on board the

spacecraft but to also briefly study the giant planet, allowing for some of the sharpest views of the jovian atmosphere before the ongoing *Juno* mission by NASA. Cassini's ISS instrument, with its great number of different filters, shows how the different bands react and reflect light at distinct wavelengths, all the while contributing with some intrinsic emission as well at longer wavelengths.

Along its path, Cassini was able to capture global views of Jupiter for a few months with the best compromise between spatial resolution and latitude range being achieved between December 2000 and January 2001 where we could perform cloud tracking with PICV2 for a complete latitudinal profile of the zonal winds, capturing jet streams flowing in different directions in the jovian atmosphere.

Data Volume	Image pairs	Filters	Date (yyyy-mm-dd)	Time Int.	Latitude Range
1004	N1354886098_1 N1354921390_1	CL1;CB2	2000-12-07	9h48m	75°S - 15°N
1004	N1355237264_1 N1355275124_1	CL1;MT2	2000-12-11	9h31m	20°S - 90°N
1004	N1355298277_1 N1355332351_1	CL1;MT3	2000-12-12	9h32m	80°S - 40°N
1004	N1355328495_1 N1355362570_1	CL1;CB2	2000-12-12	9h28m	30°S - 10°S
1004	N1355328458_1 N1355362532_1	BL1;CL2	2000-12-12	9h28m	80°S - 25°N

Table 3.3: Observed image pairs of Jupiter from Cassini/ISS. The name of each image file in the ISS catalogue has a letter where 'N' refers to the narrow angle camera and the 'W' refers to the wide angle camera. The filter combination used for each image assign different wavelengths ranges. These were used to maximise the contrast between cloud features in the images and they mainly located in the visible and near-infrared spectrum.

Some of the observations referenced in table 3.3 also allowed a close up view of the *Great Red Spot* storm system and cloud tracking was performed to study the circulation in this complex feature.

3.2.2 Saturn

Observations of Saturn with the ISS camera provided, as in Jupiter, a global view of the planet and much more data of this system was available than for Jupiter since for the former we could only rely on a couple of months of observation (as it flew past the planet to reach its destination) and for the latter we have more than 10 years of observations of the cronian system, in spite of having more targets (ring system and moons). Greater challenges were met as the rings block the equatorial region, including its known powerful jet in most images and a good enough resolution to track the winds in the north polar region of Saturn was also something to look out for.

Data Volume	Image pairs	Filters	Date (yyyy-mm-dd)	Time Int.	Latitude Range
2003	N1464579843_1 N1464617946_1	CL1;MT3	2004-05-30	10h35m	90°S - 20°N
2003	N1464579932_1 N1464617946_1	CL1;MT3	2004-05-30	10h34m	90°S - 0°N
2006	N1473176820_1 N1473214620_1	CL1;MT3	2004-09-06	10h30m	90°S - 20°N
2089	W1774190216_1 W1774225676_1	CB2;CL2	2014-03-22	9h51m	20°S - 90°N
2090	W1775233235_1 W1775270196_1	CB2;CL2	2014-04-03	10h16m	0°N - 90°N
2090	W1775416100_1 W1775452922_1	CB2;CL2	2014-04-05	11h00m	10°S - 90°N
2091	N1789050032_1 N1789058198_1	CL1;CB3	2014-09-10	2h17m	70°N - 90°N

Table 3.4: List of observed image pairs from Cassini ISS data. Since several data volumes were available due to Cassini's extended period on the cronian system, we have more data volumes listed on this table. As for the Jupiter case, filter combinations were chosen based on the maximum contrast in order to better identify features for PICV2 to track. Great interest was also given to the north polar region, particularly the dynamics of the outer edges and inner regions of the hexagon.

From table 3.4 we notice the difference between some observations (almost 10 years apart). Along with different filters used to explore distinct feature in Saturn's atmosphere, this was required to fully capture a complete latitudinal profile on both hemispheres of saturn, even if at different seasons.

Chapter 4

Results

4.1 Venus

4.1.1 VEx - VMC

Given our projected images, more than 200 wind tracers were calculated on each pair. With the statistical line averaging of PICV2, 41 tracers were retrieved for the south hemisphere of Venus from both pairs at 365 nm.

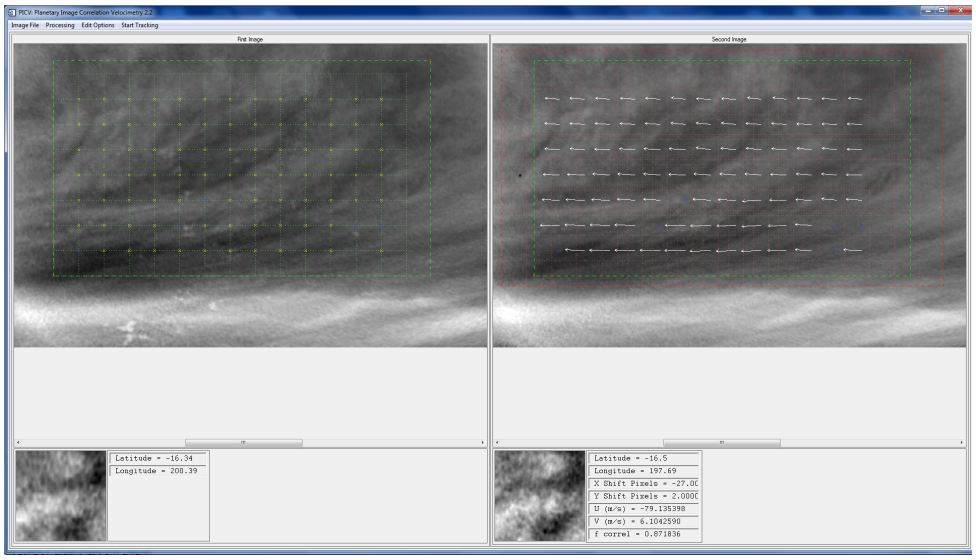

Figure 4.1.1: The wind tracers calculated by PICV2 on the V0031 orbit image pair. The same kind of tracers were retrieved on the other VMC orbit.

By cloud tracking on the different image pairs I was able to build the following plots (figure 4.1.2), showing the mean zonal wind flow on a latitude profile of the south hemisphere for both orbits.

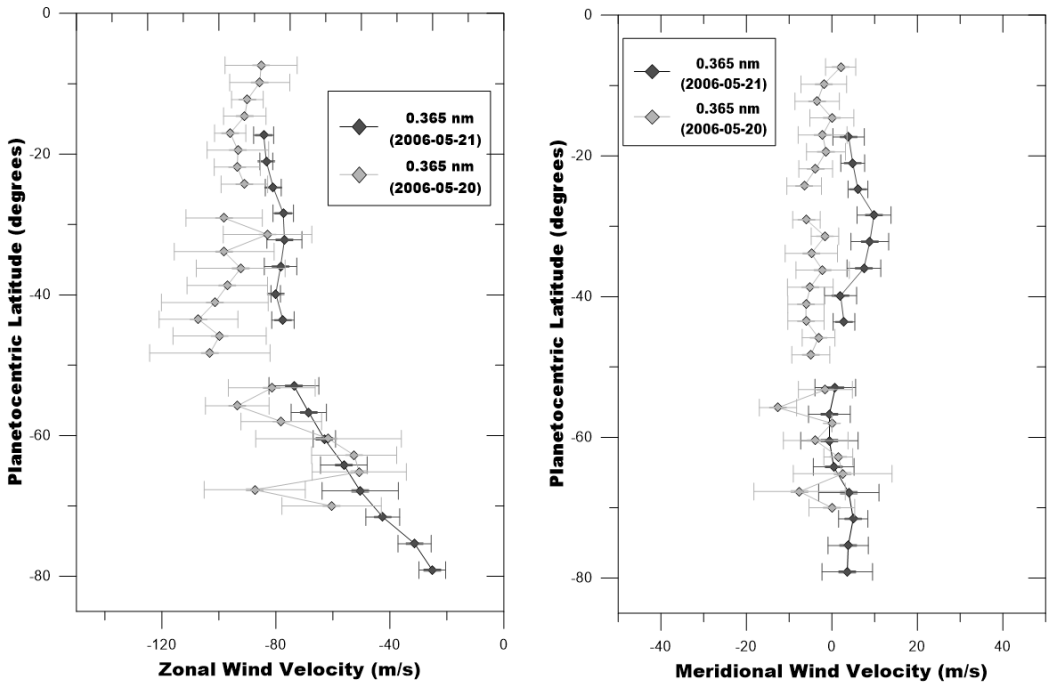

Figure 4.1.2: Zonal and meridional winds cloud tracked at 365 nm using VMC image orbits V0030 and V0031 as seen in table 3.2. These are the statistical averages calculated by PICV2 along an horizontal line when cloud tracking is performed. In the legend we can see that both data sets have the same wavelength and are 1 day apart.

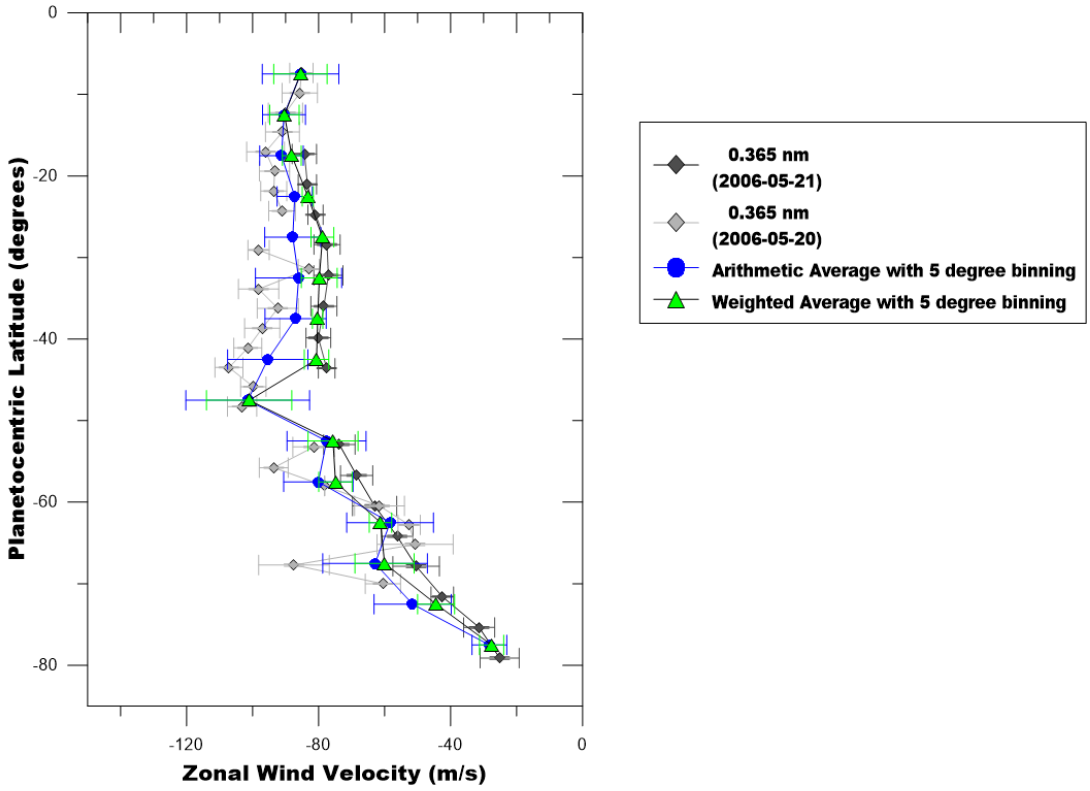

Figure 4.1.3: By performing a weighted average within a 5 degree binning we retrieve the mean zonal wind flow on the south hemisphere of Venus as captured by the UV filter of VMC at 365 nm (in green) . We included the arithmetic average (in blue) of the results for completion, even though the weighted average ones can be more accurate since they disregard outliers better.

From figure 4.1.2, regarding zonal winds, we note that in spite of having the same wavelength and each image pair being just a day apart there's substantial difference between both orbits, at least outside of our standard errors. The meridional winds measured by this software unfortunately do not have much significance as the zonal velocity component, since most often there's isn't enough resolution on our images to properly track vertical winds which are weaker and of similar magnitude of the error bars. For a more comprehensive understanding of our results, we performed a weighted average with a binning of 5 degrees from the original results.

According to figure 4.1.3 we have a steady zonal wind velocity from near equatorial regions to the mid latitudes where the velocity increases (at about 55°) and then drops as we move towards the south polar region.

On the subject of gravity waves, the data base was built to contain all this information for future use, so as to easily pinpoint images with atmospheric gravity waves for a more in-depth analysis of wave packet properties. In this data base, a single orbit was assigned for each excel sheet, which could contain from 50 to 300 images.

File Name	Image Number	VMC Channel	Gravity Waves Present?	Image Defective?
V2611_0000_UV2.jpg	0	UV	No	No
V2611_0001_VI2.jpg	1	VIS	No	No
V2611_0002_N12.jpg	2	NIR1	No	No
V2611_0003_N22.jpg	3	NIR2	No	No
V2611_0004_UV2.jpg	4	UV	No	No
V2611_0005_VI2.jpg	5	VIS	No	No
V2611_0006_N12.jpg	6	NIR1	No	No
V2611_0007_N22.jpg	7	NIR2	No	No
V2611_0008_UV2.jpg	8	UV	No	No
V2611_0009_VI2.jpg	9	VIS	No	No
V2611_0010_N12.jpg	10	NIR1	No	No
V2611_0011_N22.jpg	11	NIR2	No	No
V2611_0012_UV2.jpg	12	UV	No	No
V2611_0013_VI2.jpg	13	VIS	No	No
V2611_0014_N12.jpg	14	NIR1	No	No
V2611_0015_N22.jpg	15	NIR2	No	No
V2611_0016_UV2.jpg	16	UV	No	No
V2611_0017_VI2.jpg	17	VIS	No	No
V2611_0018_N12.jpg	18	NIR1	No	No
V2611_0019_N22.jpg	19	NIR2	No	No
V2611_0020_UV2.jpg	20	UV	No	No
V2611_0021_VI2.jpg	21	VIS	No	No
V2611_0022_N12.jpg	22	NIR1	No	No
V2611_0023_N22.jpg	23	NIR2	No	No
V2611_0024_UV2.jpg	24	UV	No	No
V2611_0025_VI2.jpg	25	VIS	No	No
V2611_0026_N12.jpg	26	NIR1	No	No
V2611_0027_N22.jpg	27	NIR2	No	No
V2611_0028_UV2.jpg	28	UV	No	No
V2611_0029_VI2.jpg	29	VIS	No	No
V2611_0030_N12.jpg	30	NIR1	No	No

Number of Images with Gravity Waves in Orbit	Number of Images with GW doubts in orbit	Number of Gravity Waves (Doubts included)
4	4	8

V2611_0042_N12.jpg	44	NIR1	No	Moderate
V2611_0042_N22.jpg	45	NIR2	No	Mild
V2611_0043_UV2.jpg	46	UV	No	No
V2611_0044_N12.jpg	47	NIR1	No	Mild
V2611_0045_N22.jpg	48	NIR2	No	No
V2611_0046_VI2.jpg	49	VIS	No	Mild
V2611_0047_UV2.jpg	50	UV	No	No
V2611_0048_N12.jpg	51	NIR1	No	Mild
V2611_0049_N22.jpg	52	NIR2	???	No
V2611_0050_VI2.jpg	53	VIS	???	Mild
V2611_0051_UV2.jpg	54	UV	Yes	No
V2611_0052_N12.jpg	55	NIR1	Yes	Mild
V2611_0053_N22.jpg	56	NIR2	???	No
V2611_0054_VI2.jpg	57	VIS	Yes	Mild
V2611_0055_UV2.jpg	58	UV	Yes	No
V2611_0056_N12.jpg	59	NIR1	No	Mild
V2611_0057_N22.jpg	60	NIR2	No	No
V2611_0058_VI2.jpg	61	VIS	???	Mild
V2611_0059_UV2.jpg	62	UV	No	Mild
V2611_0060_N12.jpg	63	NIR1	No	Moderate
V2611_0061_N22.jpg	64	NIR2	No	Moderate
V2611_0062_VI2.jpg	65	VIS	No	Mild
V2611_0063_UV2.jpg	66	UV	No	Mild
V2611_0064_N12.jpg	67	NIR1	No	Moderate
V2611_0065_N22.jpg	68	NIR2	No	Mild

Figure 4.1.4: A single sheet of the data base. This figure contains information for the VMC orbit 2611 and is cut in two parts of the sheet: the heading and its organization; and a small section which illustrates images that have confirmations of waves (green shading) and doubts (yellow shading). For each image we have the name of the image file, a number associated with it (starting in 0), the filter used for the image, the information regarding existence of gravity waves in the image and image defection classification.

A generous contribution was provided by a bachelor's student (Melissa Serra), who helped in the detection of gravity waves in some of these orbits. More than 63,000 VMC images were analysed, comprised in approximately 300 orbits. On average, there are close to 3 images with confirmed detections of atmospheric gravity waves per orbit and a total of 579 images were classified as doubtful for further study. In total, there are more than 870 VMC images with confirmed atmospheric gravity waves detected which will be used for further characterisation and there are still more than 200,000 VMC images to analyse. Hence we expect even more data to measure wave properties from.

4.1.2 VEx - VIRTIS

During observations with this instrument, it was noticed that some images provided better wind tracers but also that some images covered similar latitudinal regions, thus we will only present here the most pertinent results, both for the south hemisphere zonal wind profile in the visible and IR spectra and some polar data for high latitudes and the south polar vortex.

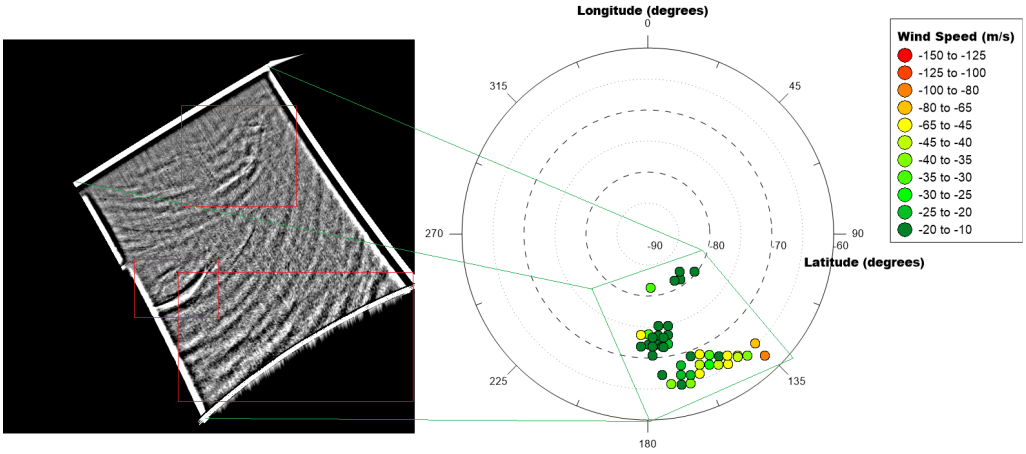

Figure 4.1.5: Wind velocity measurements in high latitudinal region of Venus at 540 nm, captured with the VIRTIS instrument on VEx orbit 2936 (4^{th} of May, 2014). On the left is a cropped section of the polar projected image, marking the cloud features from which wind tracers were retrieved. Errors associated with these tracers are on the order of 10 m/s.

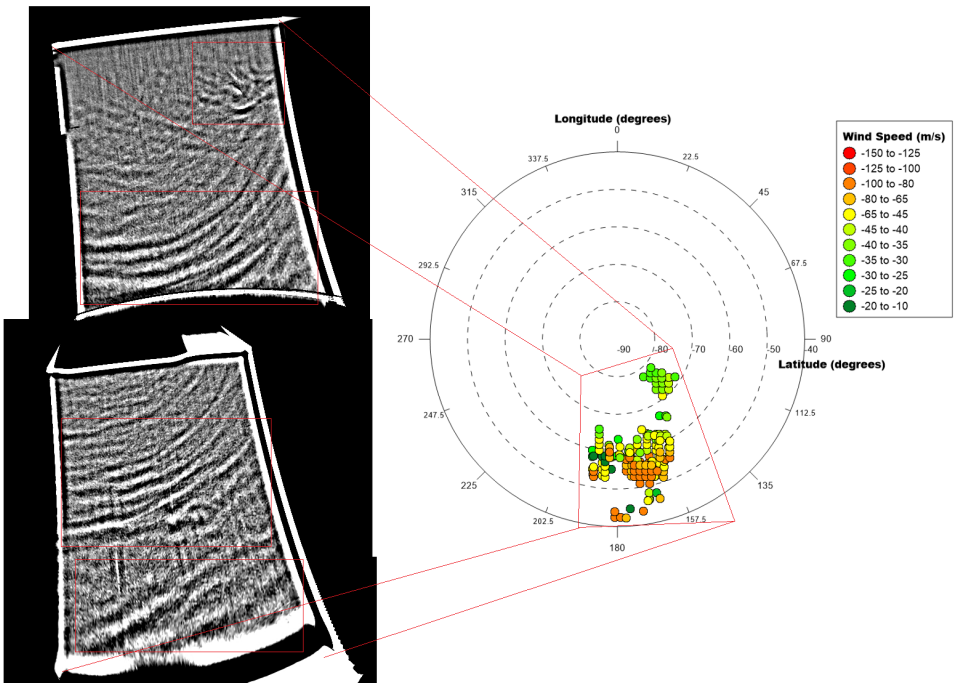

Figure 4.1.6: Wind velocity measurements on high-mid latitudes in south hemisphere of Venus at 543 nm, captured with the VIRTIS instrument on VEx orbit 2944 (12^{th} of May, 2014). To build this plot, data from different image pairs were used which enabled the capture of wind tracers at lower latitudes (bottom-left image) and since the time difference between both pairs is only 2 hours we expect a similar velocity pattern on both pairs. Errors associated with these tracers are on the order of 10 m/s.

Even though we could only cover a small section of the south hemisphere of Venus, these polar plots allow us to know which features are being measured and how their zonal wind flow is relatable as each point on this plot is a calculated wind tracer.

Finding appropriate images from which good tracers could be retrieved with PICV2 on mid-low latitudes on Venus for both the cloud tops (UV/Visible) and lower cloud deck (IR) was a challenging task and our results represent a wider collection of data where different image pairs are months apart. This is also useful to properly characterise the average zonal wind flow on Venus in an attempt to obtain the general average circulation of its south hemisphere.

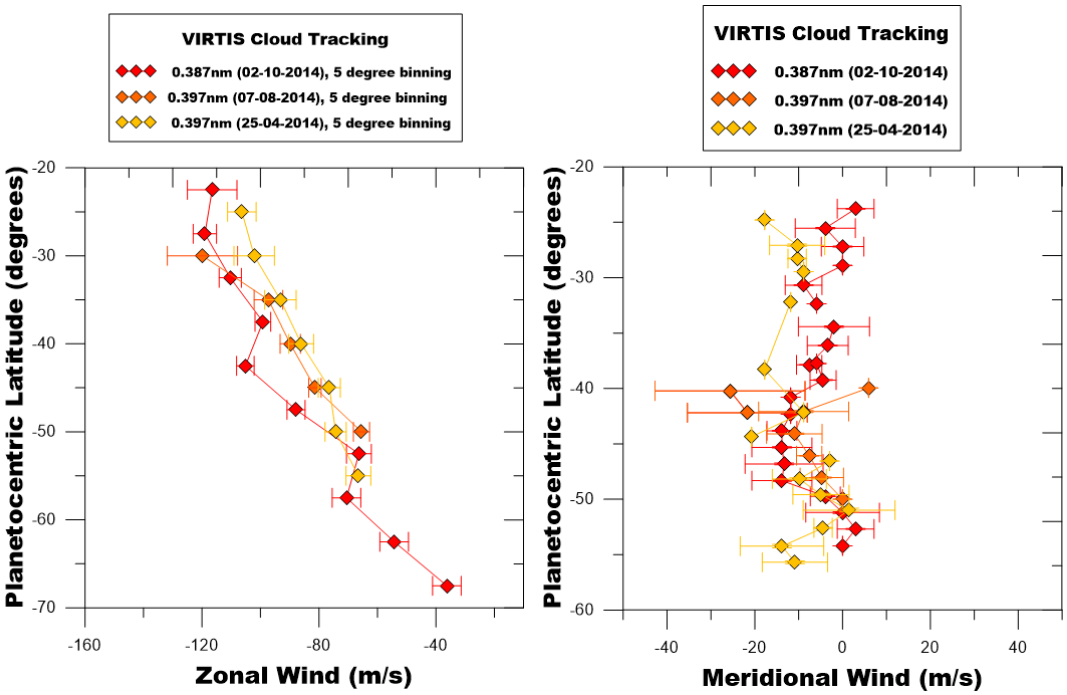

Figure 4.1.7: This graphic is the combination of the averaged zonal wind and meridional wind on the south hemisphere of Venus along three diferent image pairs (from VEx orbits 2927, 3034 and 3094), separated by several months (illustrated in the figure's legend) in the near UV range.

Though the weighted average and 5 degree binning significantly improved the quality of these results, the zonal winds measured between $45°S - 55°S$ are uncommonly low even though Venus' cloud tops are subject to substantial variability. Once again, the meridional winds obtained are mostly scattered as we are limited by resolution and these winds are much weaker than the zonal velocity component.

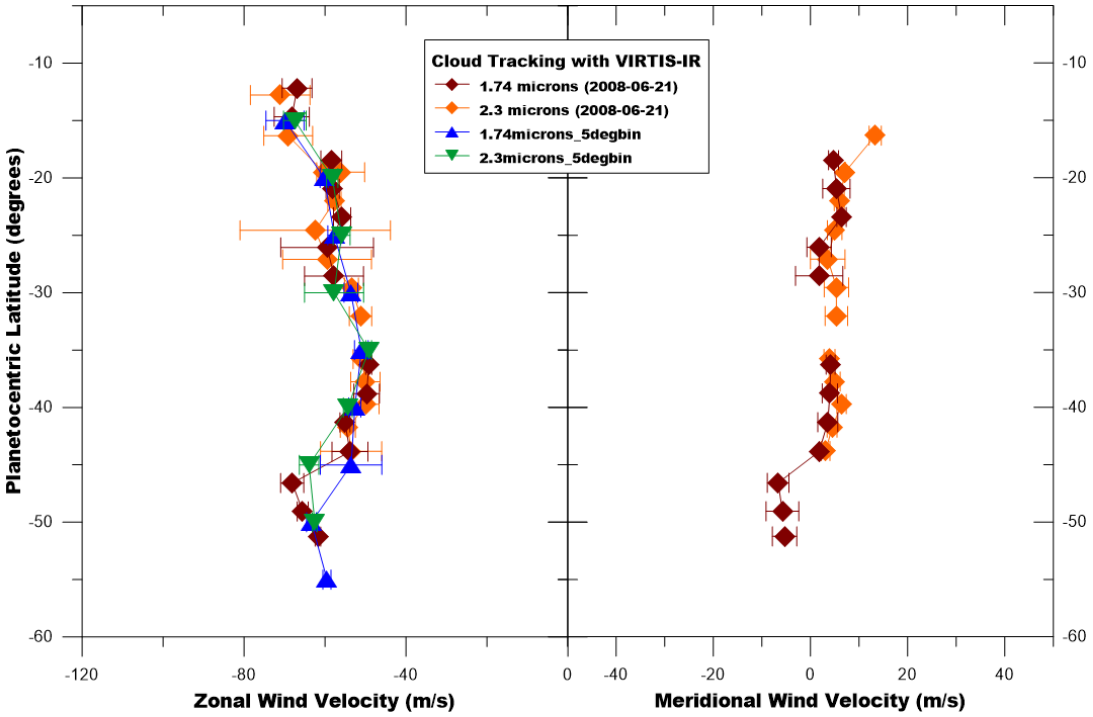

Figure 4.1.8: Zonal and Meridional wind velocity results from VIRTIS-IR images at 1.74 and 2.3 μm which allows visualization of the lower cloud deck ($\approx$ 48 km of altitude). Cloud tracking was performed on both wavelengths in the same image to get glimpse at how the winds may vary in the lower cloud deck.

As we can see from figure 4.1.8, the zonal wind flow is reasonably steady at the observed latitudinal region and is, in general, lower than on the cloud tops as expected.

We also took an interest on the south polar vortex of Venus and using the same cloud tracking method we retrieved wind velocities from this highly dynamical region (see figure 1.1.4). In order to grasp this variability, both in shape and dynamics, I choose two image pairs with a clear view of the south pole, approximately 20 hours apart.

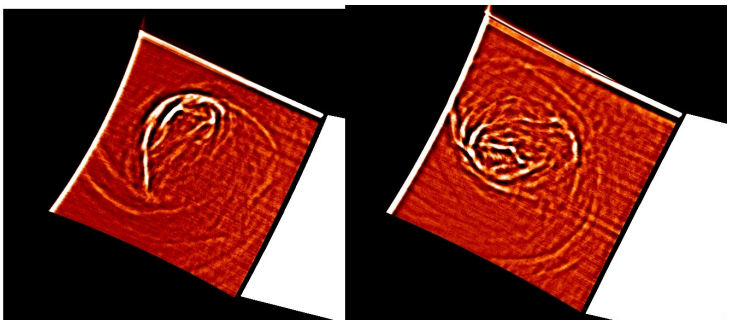

Figure 4.1.9: South Pole Vortex as captured by the VIRTIS instrument at approximately 3.7 μm, during VEx orbits 473 and 474 (6^{th} and 7^{th} of August, 2007). Both images are from different image pairs (20 hours apart) and were later used for cloud tracking with PICV2.

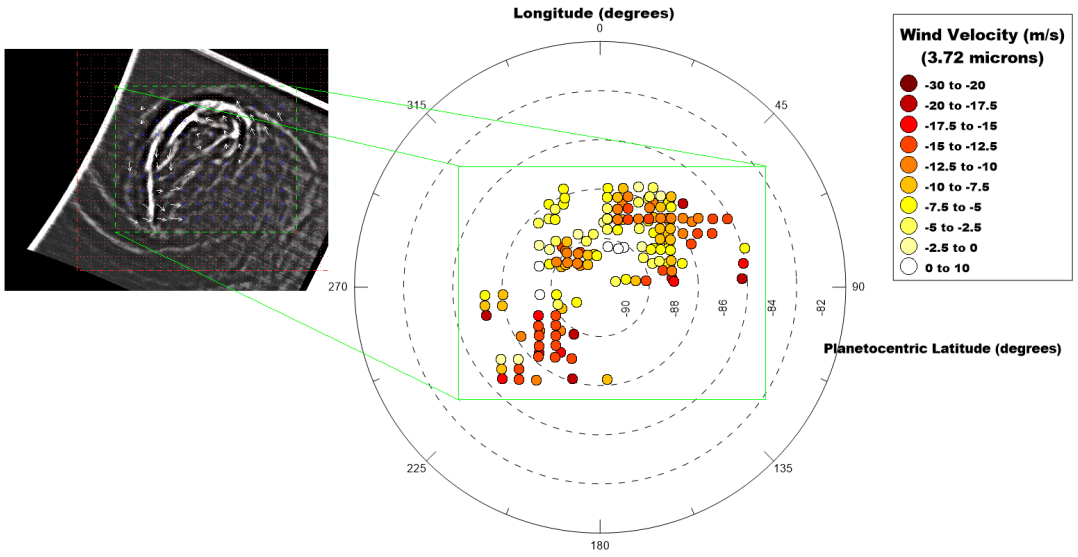

Figure 4.1.10: Wind velocity measurements of the south polar vortex of Venus on the 6^{th} of August of 2007. On the left we see one of the images from the pair with exemplar wind tracers which are used to build polar graphics like the one shown here. Errors associated with these tracers are on the order of 10 m/s.

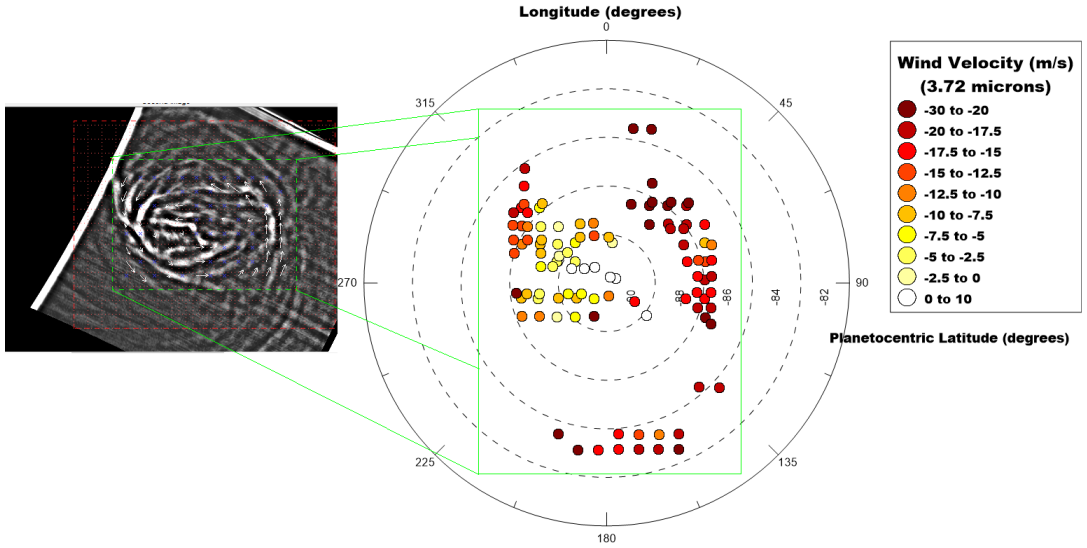

Figure 4.1.11: Wind velocity measurements of the south polar vortex of Venus on the 7^{th} of August of 2007. On the left we see one of the images from the pair with exemplar wind tracers which are used to build polar graphics like the one showed here. Errors associated with these tracers are on the order of 10 m/s.

From figures 4.1.10 and 4.1.11 we can see how vortex shapes change almost on a daily basis, which is relatable to dynamical variation recorded by the wind tracers measured here. However the wind speeds of most of these features aren't very strong, at least when compared to zonal wind flow at low-mid latitudes, where the faster winds (according to the results in 4.1.8) where close to 60 m/s.

From the systematic search for atmospheric gravity waves on our window of observations (August of 2007) 46 images with waves were identified and even more images require further confirmation. All this information is provided, as for VMC images, on an excel sheet, though some minor modifications had to be made due to our use of distinct instruments.

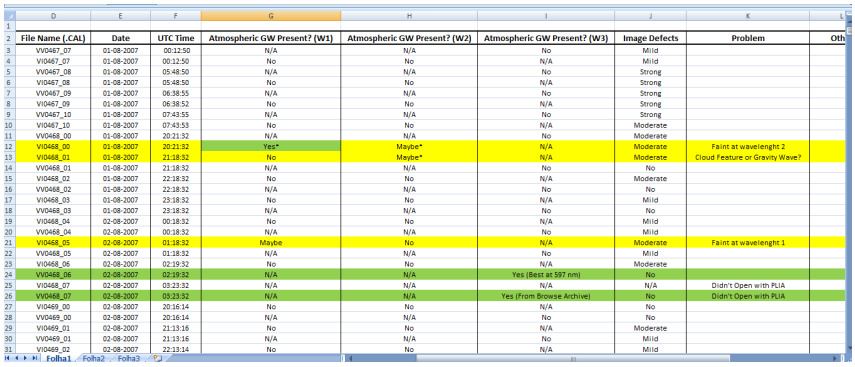

File Name (.CAL)	Date	UTC Time	Atmospheric GW Present? (W1)	Atmospheric GW Present? (W2)	Atmospheric GW Present? (W3)	Image Defects	Problem	Oth
VV0467_07	01-08-2007	00:12:50	N/A	N/A	No	Mild		
VI0467_07	01-08-2007	00:12:50	No	No	N/A	Mild		
VV0467_08	01-08-2007	05:48:50	N/A	N/A	No	Strong		
VI0467_08	01-08-2007	05:48:50	No	No	N/A	Strong		
VV0467_09	01-08-2007	06:38:55	N/A	N/A	No	Strong		
VI0467_09	01-08-2007	06:38:52	No	No	N/A	Strong		
VV0467_10	01-08-2007	07:43:55	N/A	N/A	No	Strong		
VI0467_10	01-08-2007	07:43:53	No	No	N/A	Moderate		
VV0468_00	01-08-2007	20:21:32	N/A	N/A	No	Moderate		
VI0468_00	01-08-2007	20:21:32	Yes*	Maybe*	N/A	Moderate	Faint at wavelenght 2	
VI0468_01	01-08-2007	21:18:32	No	Maybe*	N/A	Moderate	Cloud Feature or Gravity Wave?	
VV0468_01	01-08-2007	21:18:32	N/A	N/A	No	No		
VI0468_02	01-08-2007	22:18:32	No	No	N/A	Moderate		
VV0468_02	01-08-2007	22:18:32	N/A	N/A	No	No		
VI0468_03	01-08-2007	23:18:32	No	No	N/A	Mild		
VV0468_03	01-08-2007	23:18:32	N/A	N/A	No	No		
VI0468_04	02-08-2007	00:18:32	No	No	N/A	Mild		
VV0468_04	02-08-2007	00:18:32	N/A	N/A	No	Mild		
VI0468_05	02-08-2007	01:18:32	Maybe	No	N/A	Moderate	Faint at wavelenght 1	
VV0468_05	02-08-2007	01:18:32	N/A	N/A	No	Mild		
VI0468_06	02-08-2007	02:19:32	No	No	N/A	Moderate		
VV0468_06	02-08-2007	02:19:32	N/A	N/A	Yes (Best at 597 nm)	No		
VI0468_07	02-08-2007	03:23:32	N/A	N/A	N/A	N/A	Didn't Open with PLIA	
VV0468_07	02-08-2007	03:23:32	N/A	N/A	Yes (From Browse Archive)	No	Didn't Open with PLIA	
VI0469_00	02-08-2007	20:16:14	No	No	N/A	No		
VV0469_00	02-08-2007	20:16:14	N/A	N/A	No	No		
VI0469_01	02-08-2007	21:13:16	No	No	N/A	Moderate		
VV0469_01	02-08-2007	21:13:16	N/A	N/A	No	Mild		
VI0469_02	02-08-2007	22:13:14	No	No	N/A	Mild		

Figure 4.1.12: The header section of the file where information on the detection of atmospheric gravity waves with VIRTIS was stored. The columns from left to right: The file name lists the name of image file observed (.CAL refers to calibrated images); Date and time of observation; three target wavelength ranges on which gravity waves were observed (1.74 μm, 2.2-2.3 μm and within 365-800 nm respectively); a column for image defects; a column dedicated to any problems regarding wave identification, namely the source for doubts in detection. Colour and shading have the same meaning as in the VMC data base.

VEx image file	Date (yyyy-mm-dd)	Latitude	Longitude	Measured Wavelength (km)
VV0468_06	2007-08-02	53°S	82°	142
VI0471_01	2007-08-04	76°S	126°	338
VI0471_01	2007-08-04	75°S	100°	257
VI0472_05	2007-08-06	63°S	90°	89
VV0476_00	2007-08-09	67°S	81°	177
VV0476_00	2007-08-09	67°S	85°	202
VV0477_03	2007-08-10	71°S	143°	220
VV0477_03	2007-08-10	70°S	147°	121
VV0477_07	2007-08-10	70°S	105°	91
VV0477_07	2007-08-10	71°S	104°	192
VI0478_08	2007-08-11	77°S	91°	711
VI0478_08	2007-08-11	75°S	99°	543
VI0478_17	2007-08-11	71°S	92°	553
VI0478_17	2007-08-11	71°S	98°	357
VI0478_17	2007-08-11	70°S	104°	267
VV0478_20	2007-08-11	72°S	95°	519
VV0478_20	2007-08-11	71°S	101°	500
VI0478_24	2007-08-11	78°S	122°	713
VI0478_24	2007-08-11	77°S	113°	564
VI0479_11	2007-08-12	76°S	61°	360
VI0479_11	2007-08-12	76°S	55°	415

Table 4.1: Preliminary results on the selected VIRTIS images which showed the most prominent wave features for wavelength measurement. The latitudes and longitudes above are not precise since gravity waves are extended features.

As these images were navigated, we proceeded with preliminary characterisation of these features, namely wavelength and general phase velocity. Since these are only first results on this subject we selected the best images with waves for characterisation, whose results are presented in figure 4.1.
As for phase velocity measurements, I selected the best wave candidate which was in image VI0471_1 in the 2.2-2.3 μm range since several layers of the data cube were stacked to reduce noise. After recording several data points as seen on the right image of figure 2.3.9, I took the average value, since we are looking at the same wave-train and the general phase velocity computed was 105.04 m/s.

4.2 Jupiter

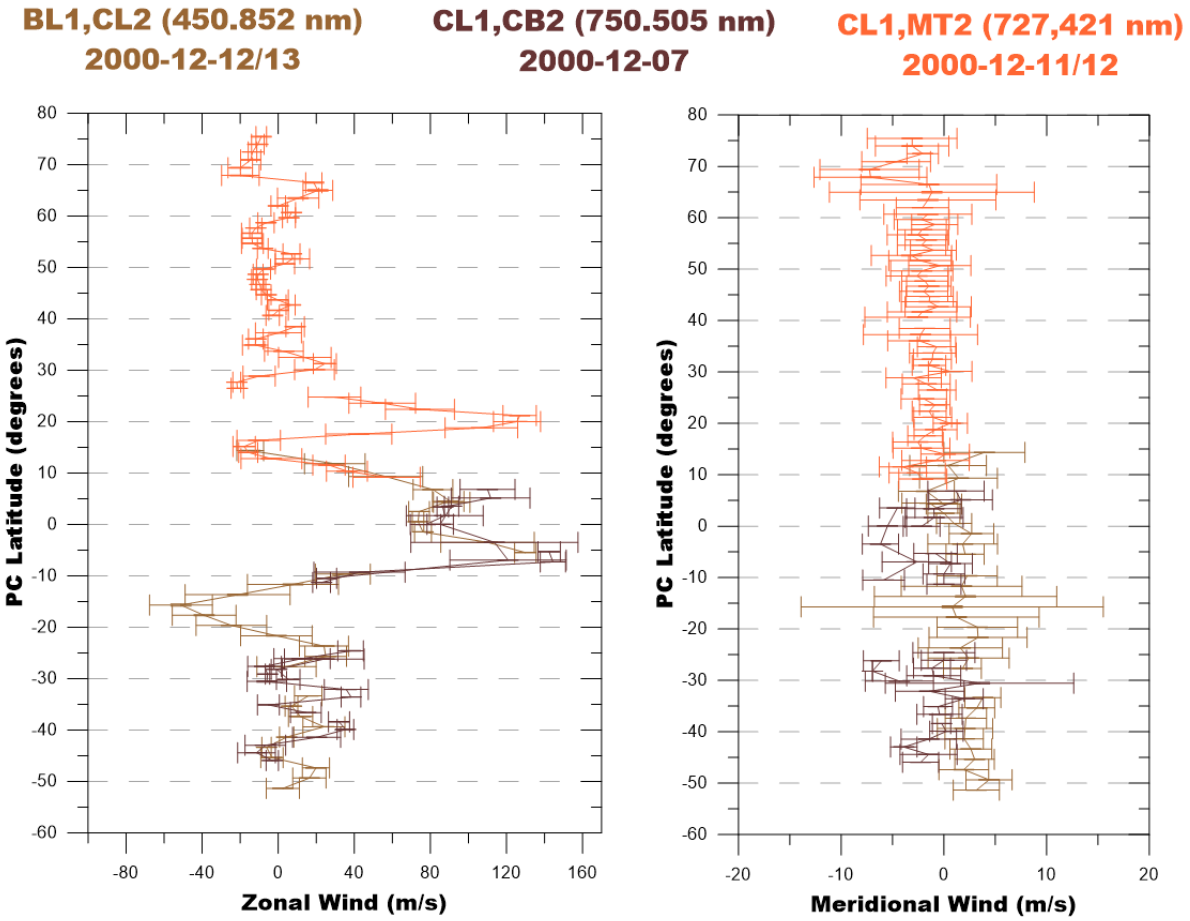

Figure 4.2.1: My cloud tracking results on Jupiter with images from the ISS camera on board Cassini. On the left we have a latitude profile of the east-west wind flow speed of the planet, approximately in the 0.7 bar level of the atmosphere (layer of the visible cloud features we can see in most visible light images of Jupiter). On the right, a profile of the meridional wind, though again the scatter, compared to the values is too great for us to rely on these measurements.

Gathering wind tracers through cloud tracking for Jupiter was a very different challenge than for Venus. Where on Venus we were greatly increasing the contrast and hunting for useful features to track, in Jupiter, atmospheric dynamical movement is easily observable at visible wavelengths and the motion of the clouds, though tracked with ease, is complex and often crowded with cloud features moving in different directions.

Despite these difficulties, Cassini ISS images allowed us to perform cloud tracking on almost all the latitudinal range of the planet, producing a zonal wind profile of approximately the entire planet (see figure 4.2.1).

To gather good wind tracers for these measurements, I had to use three different images pairs that covered various latitudinal ranges (referenced in table 3.3). The combination of filters chosen, offered the highest contrast possible in order to extract wind tracers, with also an interest in probing different atmospheric features in greater detail. The large error bars on the meridional wind profile on mid latitudes in the south hemisphere are influenced by the presence of the GRS storm system in the images used.

Originally, I intended to capture the wind velocity profile of the GRS at very different wavelengths, for an in depth study of the dynamics of storm system. However most of the close-up images of this feature were not navigated with enough precision to capture the motion's fine details in this highly convoluted system. The reason for this is that the adjustment of the navigation grid illustrated in figure 2.1.6 requires the presence of the limb in the image, and close up views of the GRS often didn't allow the visualisation of the limb for navigation corrections, which is enough to misplace the storm system by a few pixels between both images in the pairs, producing inaccurate cloud tracking results.

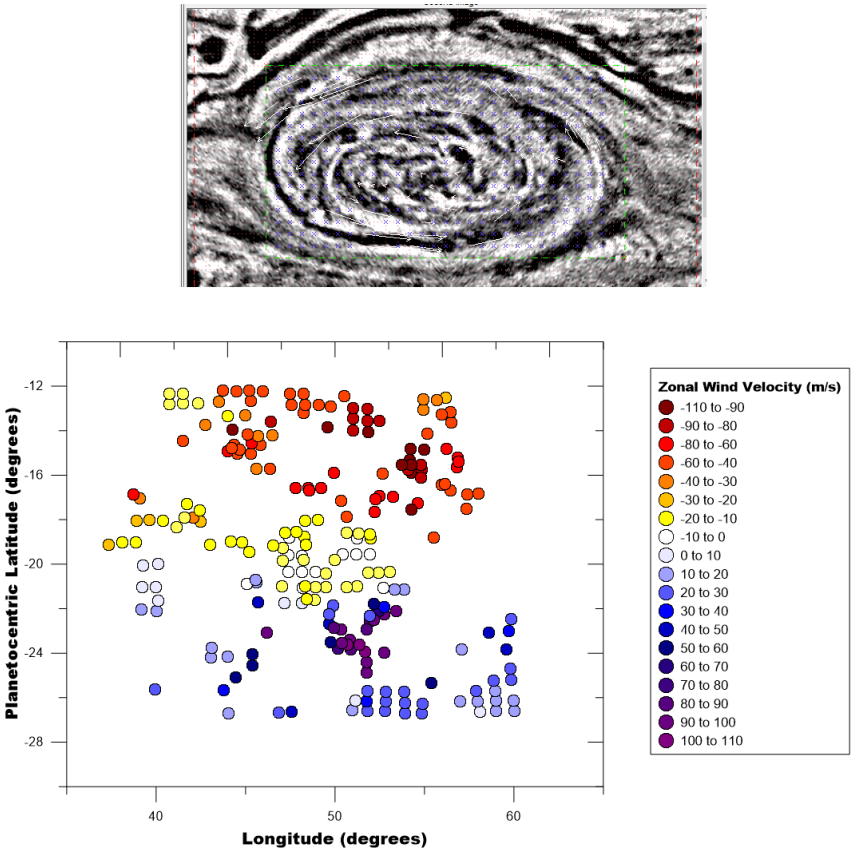

Figure 4.2.2: Zonal velocity component of the winds near and within the Great Red Spot storm system on Jupiter. The image is a cropped section of the images used for the latitudinal profile of the winds that contained this feature, at 750 nm on the 7° of December of 2000. This is a similar representation of the wind tracer results as with VIRTIS results for high-latitude and polar winds on Venus (figures 4.1.5,4.1.64.1.104.1.11). Errors associated with these tracers are on the order of 10 m/s.

The wind velocity pattern seen in figure 4.2.2 clearly shows the anticyclonic behaviour of the

storm system as well as the decreased wind speed on the core region of the storm.

4.3 Saturn

The results on the latitudinal profile of the zonal winds of Saturn were gathered with five different image pairs, to catch the movement of visible cloud features (which were much more scarce than in Jupiter) at all possible latitudes. To increase the contrast to retrieve the wind tracers, I used mostly filters that highlighted the presence of methane on the saturnian atmosphere along with other near-infrared filters of Cassini's ISS camera.

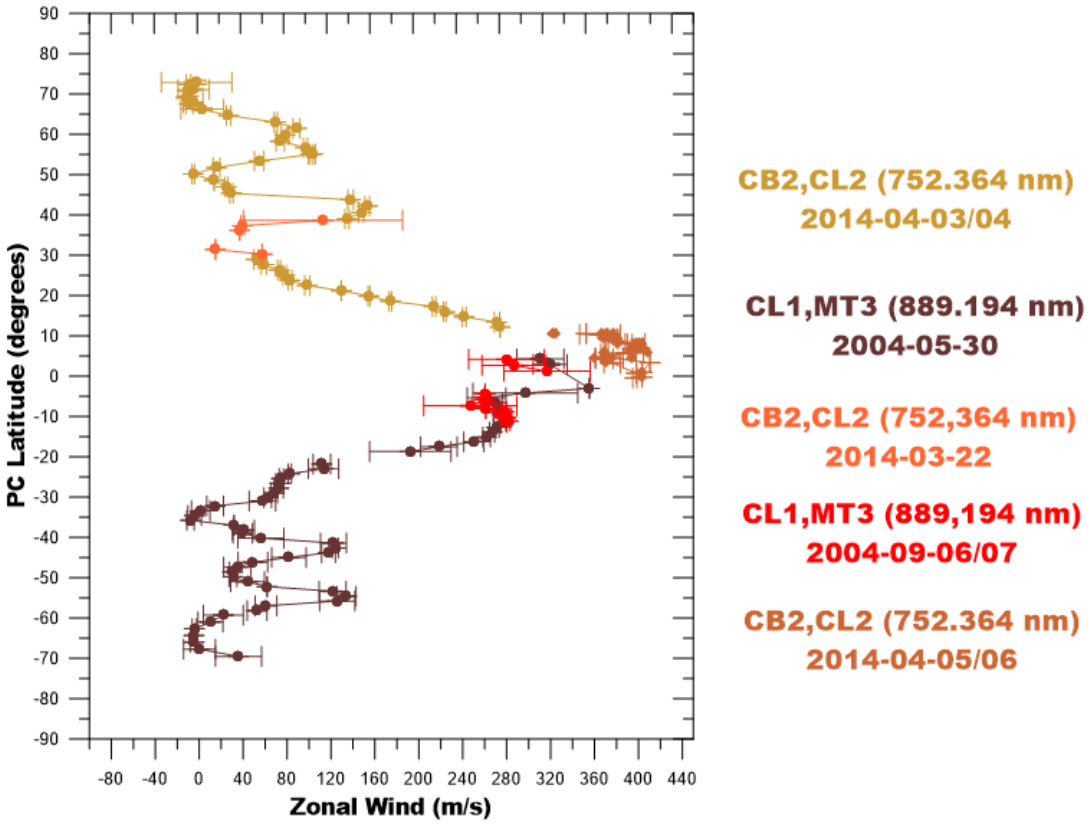

Figure 4.3.1: Zonal wind latitudinal profile of Saturn using several image pairs captured by Cassini/ISS camera in the near-infrared range. The different colour of this plot refers to data retrieved from each image pair, with filters used (wavelength) and the date of observation on the right side. The powerful equatorial jet stands out with wind speeds over 400 m/s.

Great interest was also taken on the hexagon structure in the north polar region, and wind velocities were retrieved for both the hexagon's outer edges and vicinities as well as near the north pole.

Note that in figure 4.3.3 the blue point on the bottom left area of the graphic refers to the cropped feature on the left side of figure 4.3.3 whose revolution was on the opposite direction of the general circulation inside the hexagon. Unfortunately our data didn't allow more accurate wind tracers to be calculated for this feature for a more comprehensive understanding of its dynamics.

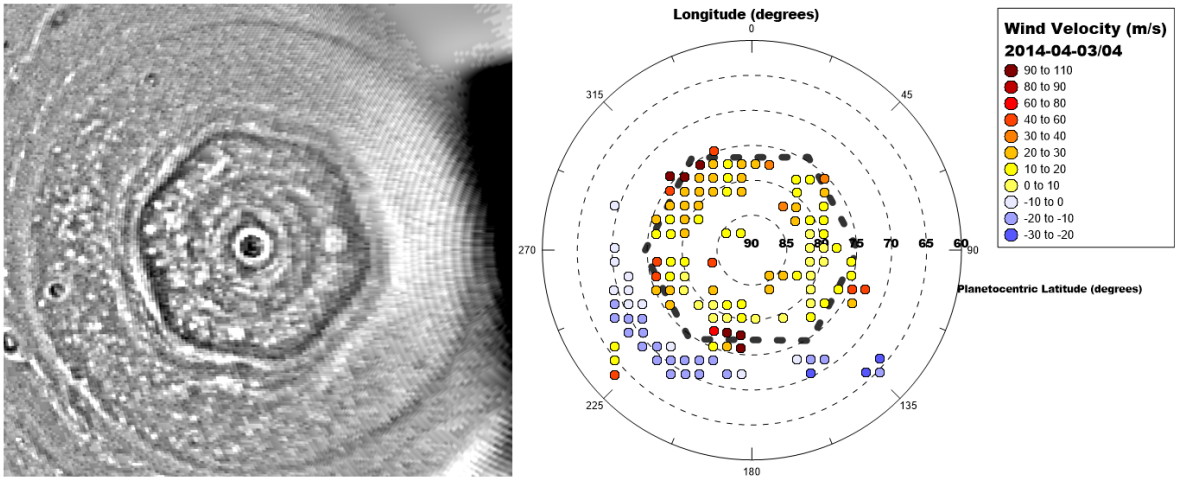

Figure 4.3.2: Wind velocity results on the north polar region of Saturn, taken between the 3^{rd} and 4^{th} of April, 2014 at 752 nm. On the left we have one of the images from the pair on which these results were obtained. Though our image resolution is limited in this case, we can see that the winds flow in different directions, inside and outside the hexagon's outline (which is the dashed line in the plot with the vertices in the approximate latitude levels of the hexagon's mean position). Errors associated with these tracers are on the order of 10 m/s.

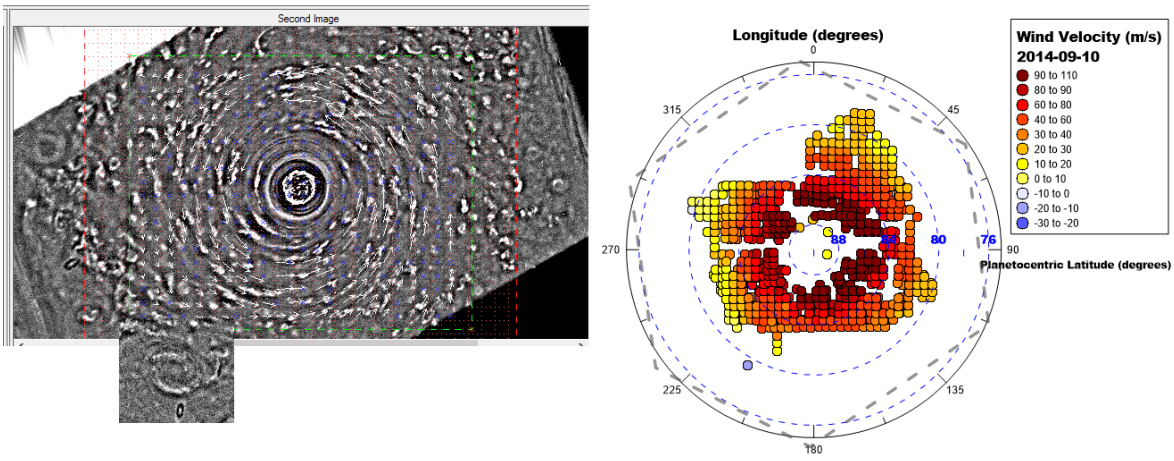

Figure 4.3.3: Wind velocity measurements from cloud tracking on the close vicinity of the north pole of Saturn, on the 10^{th} of September, 2014. This plot also includes an outline of the approximate position of the hexagon's vertices. On the right we have north pole image with wind tracers which were used to build the graphic on the left, along with another cropped section of a small feature inside the hexagon. Errors associated with these tracers are on the order of 10 m/s.

Chapter 5

Discussion

5.1 Venus

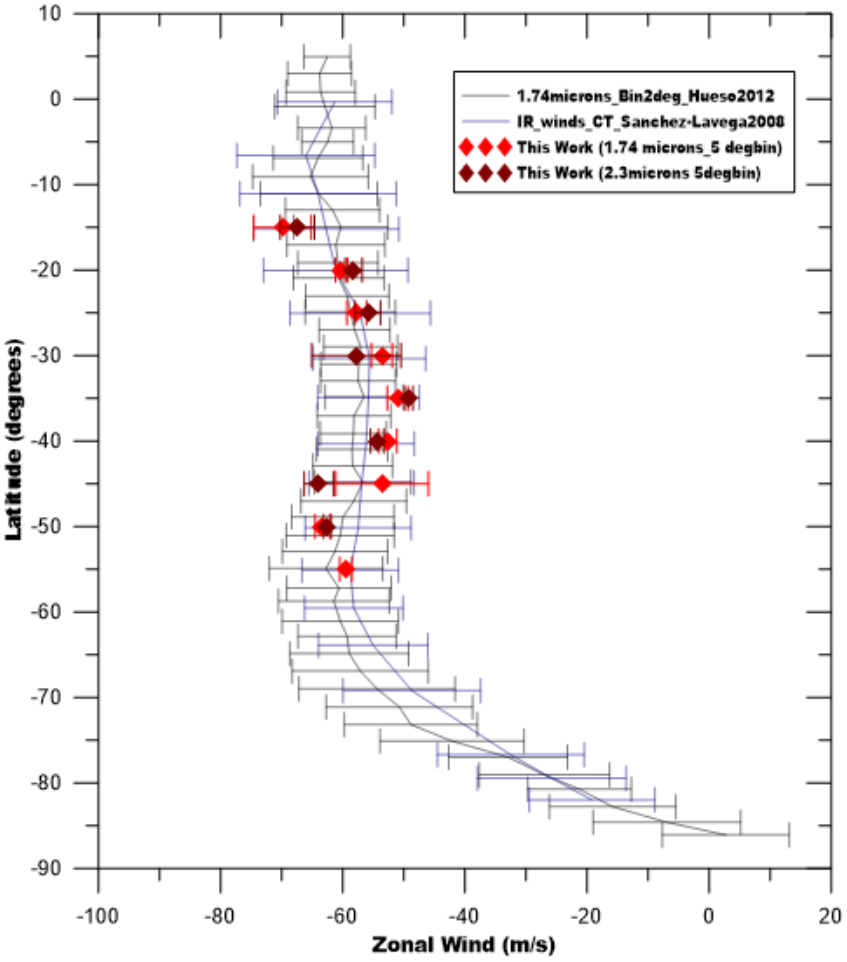

Figure 5.1.1: Latitudinal profile of Venus' zonal winds on the lower cloud deck (44-48 km). The black solid line are the results from (Hueso, R. et al., 2012) that have been averaged in 2 degree bins and the blue solid line are the results from (Sanchez-Lavega, A., et al., 2008), both being from 1.74 μm data. Errors bars from this work are smaller due to the weighted averaging process.

Venus' massive atmosphere has a zonal wind profile that changes with depth as we track cloud features in different layers of the atmosphere, more precisely at 44-48 km of altitude for our 1.74 and 2.3 μm images and at 66-72 km of altitude for our UV data (Hueso, R. et al., 2012). As previously mentioned, browsing the archive of VIRTIS data for appropriate image pairs on which cloud tracking could be optimised was quite challenging and the results presented are open to improvement by using more and distinct image pairs.

Figure 5.1.1 shows a satisfactory agreement between ours and previous results, even if we only were able to perform cloud tracking in a limited latitudinal range. We can also acknowledge that both 1.74 μm and 2.3 μm results from this work, bear similar values as these wavelengths target the lower cloud at near altitude levels and wind shear within the lower cloud deck is apparently not substantial.

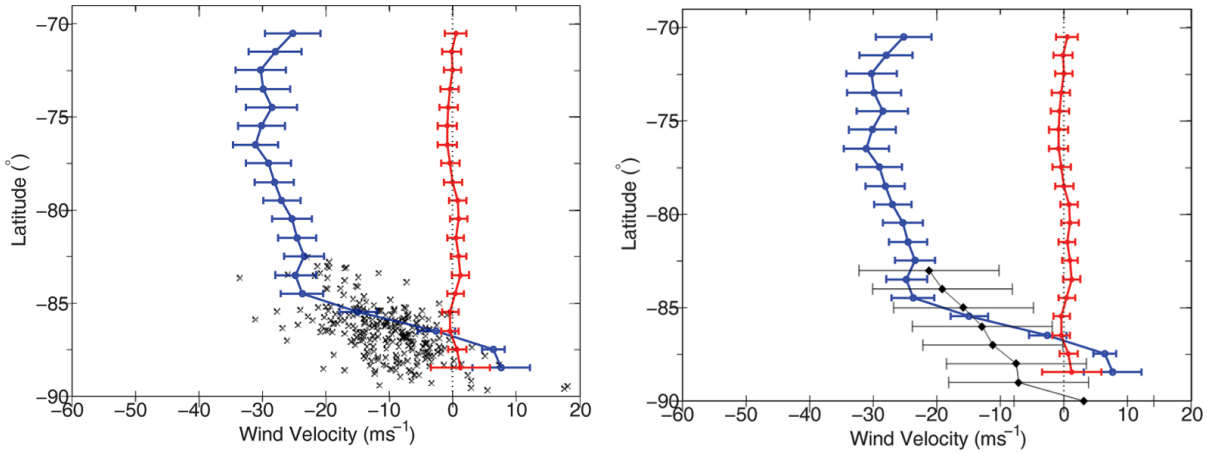

Figure 5.1.2: Zonal wind profiles of the south polar region at the upper cloud level (∼65 km) observed at 3.7 μm (this work, black) and at 3.8-5 μm (Luz et al., 2011), red and meridional wind in blue). For an easier viewing I separated the plots where I show all my data points on the south polar vortex (already seen in 4.1.10, 4.1.11) on the left and then weighted averaged them on the right (the error bars correspond to standard individual errors of cloud tracking on Venus). Results from (Luz et al., 2011) show considerably smaller error bars due to a much larger data sample of the pole than in this work.

The first objective of cloud tracking in the south polar vortex of Venus was to show its high variability within short time periods (less than 24 hours) both in terms of shape and dynamics. Comparing zonal wind results (black) from this work with (Luz et al., 2011) (red) revealed some agreement between ours and previous results. Since this structure is highly variable and our results come from much less data than results from (Luz et al., 2011), the discrepancy between them is somewhat expected. They also used 5 μm data which shows the upper cloud along with some thermal emission which could also lead to some differences between results. As in (Luz et al., 2011), our data also shows prograde winds at latitudes above 85°S which is possibly a consequence of the misalignment between the vortex center (visible in IR observations) and the planet's rotational axis.

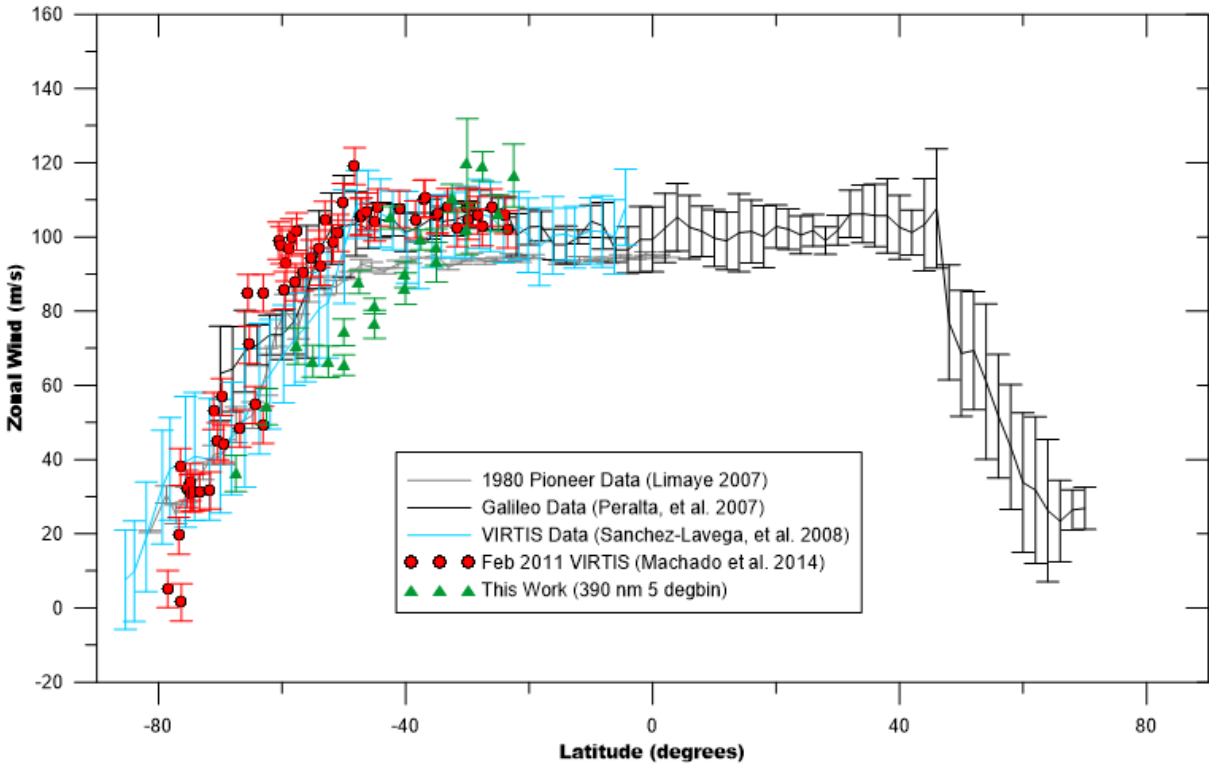

Figure 5.1.3: Latitudinal profile of Venus' zonal winds at the upper clouds (66-72 km). The grey solid line are results from Pioneer measurements performed in 1980 by (Limaye, S.S., 2007), the solid black line are results from Galileo data in (Peralta, J., et al., 2007), the blue line corresponds to results presented in (Sanchez-Lavega, A., et al., 2008) and the red data are the cloud tracking results with VIRTIS from (Machado, P. et al., 2014). All these results, including this work were gathered at wavelengths within 380-420 nm which corresponds to near UV and violet, where contrasting features in the upper clouds of Venus are observable. Results from this work already showed in figure 4.1.7 are represented as the green data in this plot.

We can see from figure 5.1.3 what I already mentioned regarding our IR cloud tracking results close to 40°, which stray considerably from standard cloud top zonal wind results. Typically, such values could result from wind variability on the cloud tops which is quite frequent, however due to the fact that our measurements were performed in three different image pairs separated by several months (see table 3.1) it is unlikely that all three show such dynamical variations from the mean zonal wind flow obtained in previous results. Some of these image pairs could have not been properly navigated or poorly tracked since image aberrations and bad lines are common occurrences in VIRTIS images which could affect measurements even though, our cloud tracking method as us supervise each tracer. However, our results are fairly consistent at higher and lower latitudes with previous measurements, well within their error bars. More cloud tracking on different image pairs targeting those latitudes will be another task for the future to ascertain if we retrieved bad tracers due to poor image quality in those region or we are witnessing true variability.

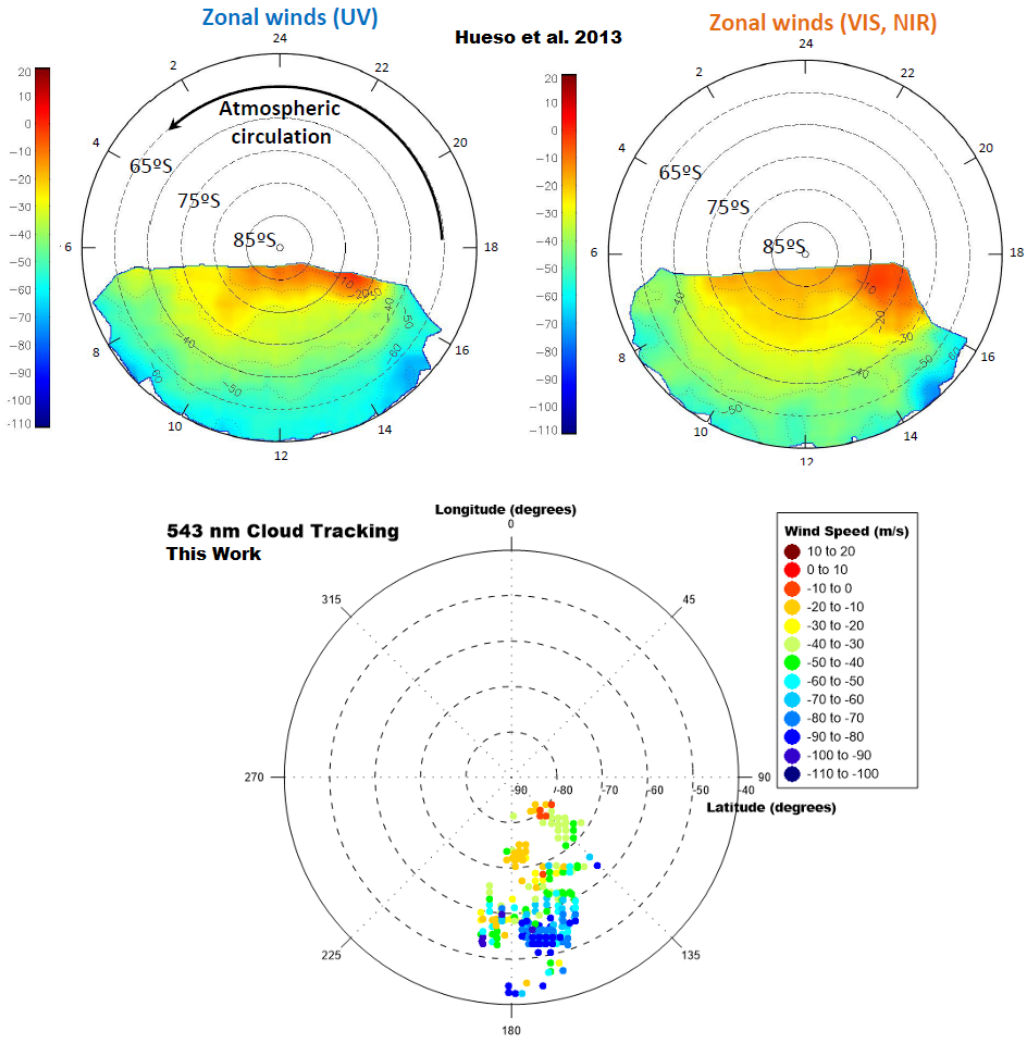

Figure 5.1.4: Colour mapped cloud tracked winds at high latitudes on Venus with VIRTIS at UV, visible and near-IR wavelengths from (Hueso, R. et al., 2013) (top) and the results from this work at visible wavelengths (540 nm) (bottom). Our results show individual wind tracers which are the combined results from figures 4.1.5, 4.1.6 with a similar colour scale for the winds.

Looking closely at figure 5.1.4, results from (Hueso, R. et al., 2013) have the zonal winds vs local time which can be related with longitude on the dayside of Venus. Though we were not able to average the zonal winds over an extended region beyond the traced features, decreasing retrograde wind motion towards the poles is present in our results, consistent with results from (Hueso, R. et al., 2013).

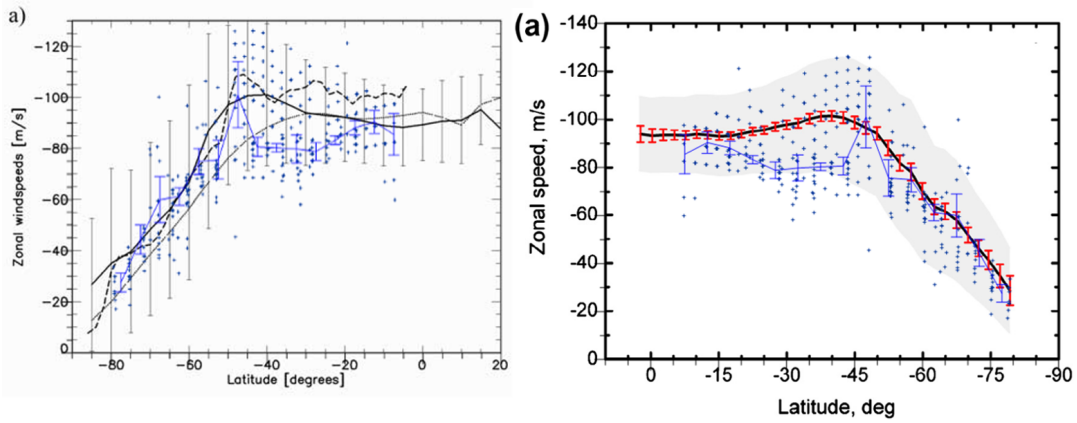

Figure 5.1.5: (left) VMC cloud tracking results comparison with (Moissl, R. et al., 2009). This plot also shows zonal wind speed profiles from VIRTIS (dashed line)(Sanchez-Lavega, A., et al., 2008) and the solid and dotted lines are from VMC cloud tracking with different routines; (right) VMC cloud tracking results comparison with (Khatuntsev, I.V., et al., 2013). The red error bars are the 99.9999% confidence interval based on the standard deviation of the weighted mean, while the shadowed area represents the standard deviation. In both plots, we have the results from this work in blue. The plus signs are the data point results for both image pairs observed (see table 3.2) and the solid blue line is the weighted average of the results from both image pairs.

Recalling the results presented in figure 4.1.3 we note that weighted calculation pushes the values towards the measurements with smaller errors (2006-05-21 VMC results from this work). However, according to figure 5.1.5 it seems that the results from cloud tracked winds in 2006-05-20 are more consistent with previous VMC results north of 45°S. In spite of this deviation, it's worth noticing that most VMC measurements to date suffer from large error bars due to navigation problems associated with VMC images which is observable in figure 5.1.5 and our results fall inside the standard deviations of previous measurements with VMC, helped by the fact that these images were navigated accurately by Javier Peralta and Ricardo Hueso. As in the case of VIRTIS results, these can also be subject to wind variability on the cloud tops, contributing to more differences between our measurements and the ones in (Moissl, R. et al., 2009) and in (Khatuntsev, I.V., et al., 2013).

5.2 Jupiter

The zonal wind profile retrieved from global Jupiter images (from table 3.3) shows the expected outline, illustrating the opposite directions in which the wind flows on Jupiter's belts and zones (zones rotate in the same direction has the planet, having positive zonal wind velocity while belts rotate on the opposite direction, having negative velocity).

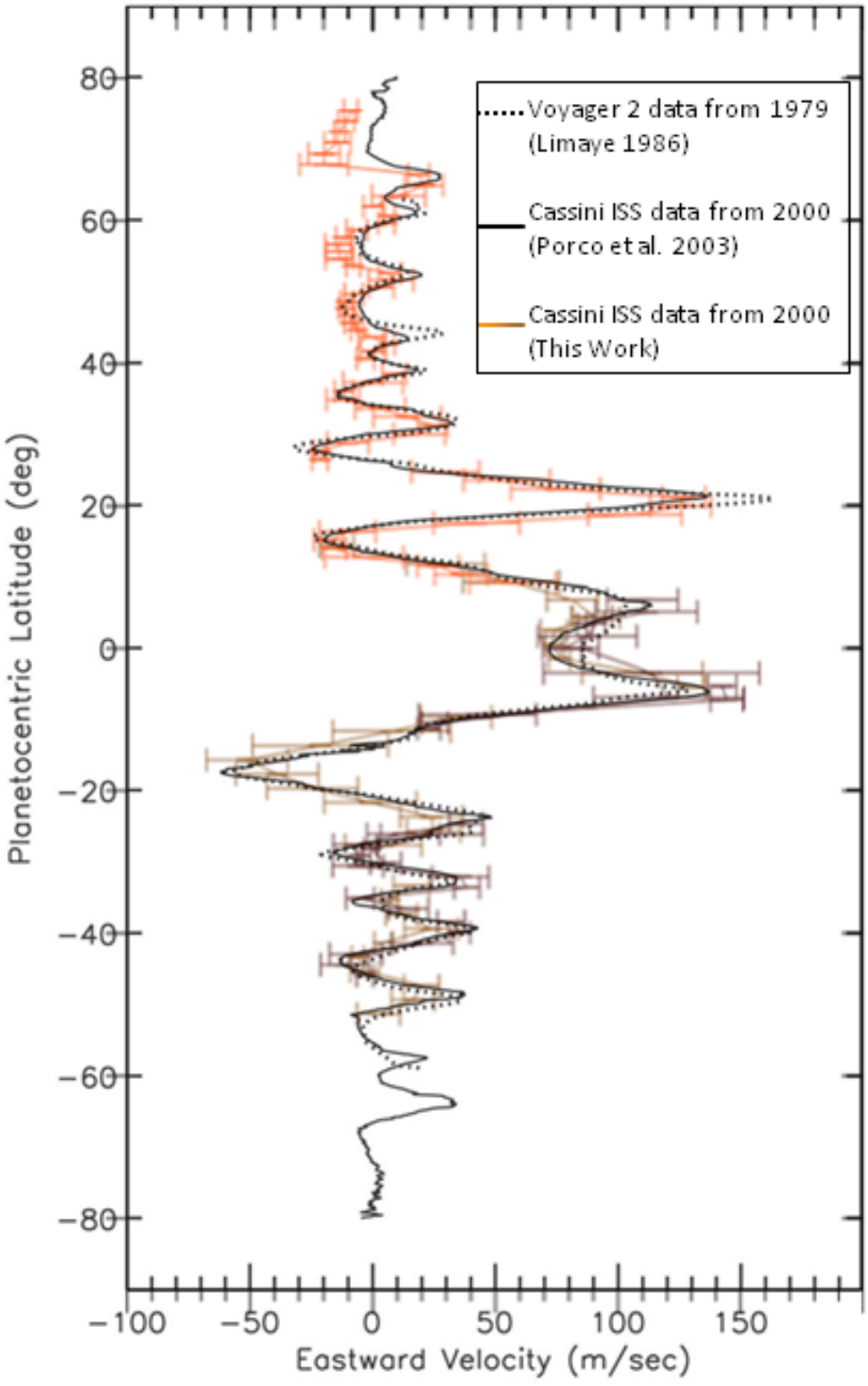

Figure 5.2.1: These are the results of the zonal wind latitudinal profile in 1979, 2000 and the results from this work. The dashed black line is from Voyager in (Limaye, S.S., 1986), the solid black line is from Cassini in (Porco, C., et al., 2003) and the coloured lines are the results from this work, also in figure 4.2.1.

With cloud tracking, we were able to retrieve the standout jet in the equatorial region with winds reaching 150 m/s and the results of this work, as observable in figure 5.2.1, show a close relation with other Cassini data, well within most error bars, proving how efficient this software can be when properly handled. Only upwards 60°N this work and the results from (Porco, C., et al., 2003) seem to differ slightly. As that area is highly turbulent and is full of small vortices and other features, it might be a source of this deviation.

The wind velocities retrieved from the GRS in Cassini ISS images of Jupiter on December 2000, despite clearly showing the anticyclonic behaviour of the storm, are not consistent on the outer edges of the storm with other data on the GRS from the same year, albeit from a different spacecraft (Galileo)((Simon-Miller, A.A., et al., 2002)). However this is a highly dynamical storm system, and wind variability of this magnitude is a possibility. Thus, continued data retrieval on the GRS is fairly important for a deep understanding of its evolution.

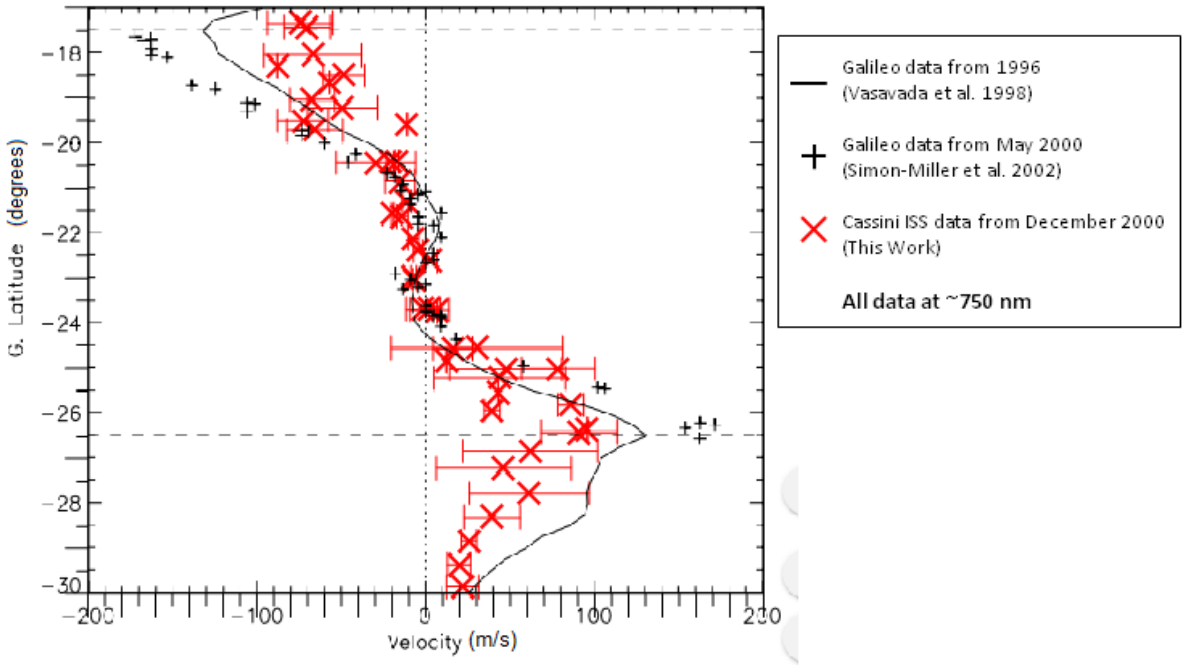

Figure 5.2.2: Planetographic latitude vs wind velocity in the Great Red Spot storm system. The solid black line represents the average of east-west winds in 0.25° latitude bins from Galileo 1996 data ((Vasavada, A.R., et al., 1998)), black data points are the Galileo data from May 2000 measurements in (Simon-Miller, A.A., et al., 2002) and the red data comes from this work with Cassini images of the GRS in December 2000. The dashed lines indicate the high velocity core size and the intersection of the dotted line with the profiles indicates the quiescent core region. All data was gathered from images at ~750 nm.

From figure 5.2.2, results from this work are not consistent, respecting the 2000 Galileo data from (Simon-Miller, A.A., et al., 2002) and also don't reach similar velocity values as in (Vasavada, A.R., et al., 1998) from 1996 data, both as we move away from the core region of the storm. Even though Cassini is technologically superior to Galileo, the fact that its path along Jupiter took it further from the planet than the Galileo probe ever was from Jupiter during its mission time, resulted in overall less resolution than Galileo images for this kind of local features which increases the size of error bars for our methods since cloud tracking becomes more difficult to perform as it relies on the visibility of the displacement of cloud features.

The three plots show some relative agreement near the quiescent core region however, cloud

features and structure are hard to distinguish on this region, which despite the weakness of the winds, could be a significant source of error for cloud tracking.

The dynamics of the GRS vary over time and this is shown by the substantial increase in wind velocity for the outer edges of the storm system between 1996 and 2000. A similar variation is seen in the results from this work, however the time span between 2000 Galileo data and late 2000 Cassini is not as great as the 4 years span of the outer two data sets. Hence, the same kind of dynamical variations on the storm's outer edges is unlikely.

5.3 Saturn

Though presenting a blander appearance than its cousin, cloud tracking on Saturn's visible cloud level was possible and we were able to retrieve the powerful equatorial eastward jet.

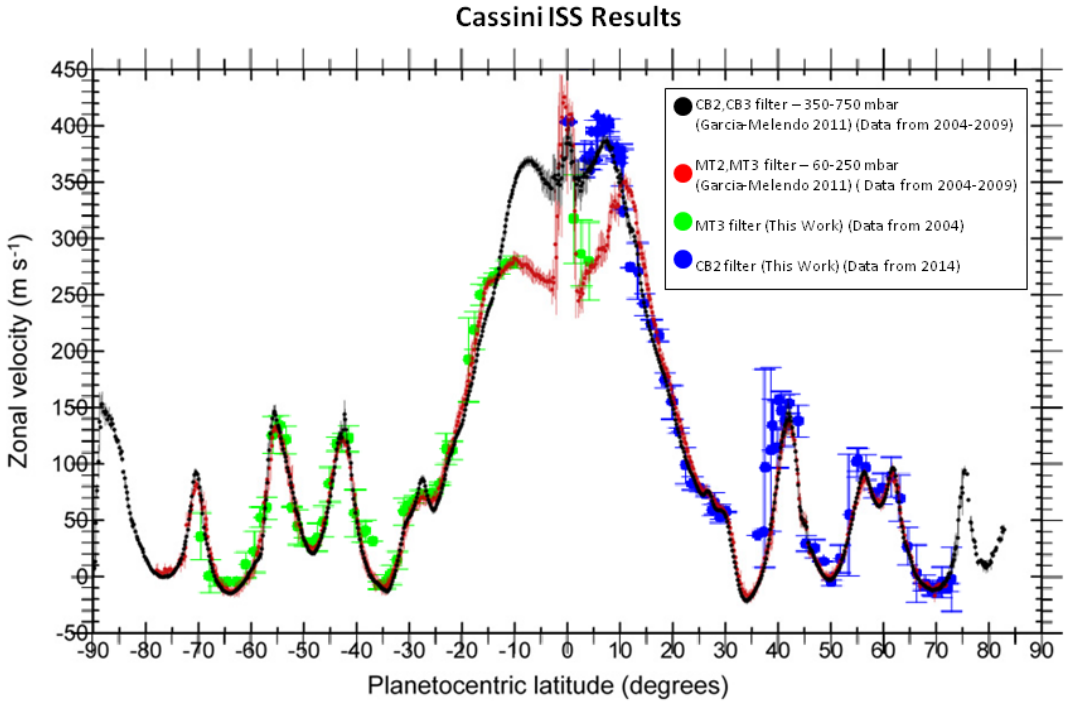

Figure 5.3.1: The results from (Garcia-Melendo et al., 2011) and comparison with saturn's latitudinal profile of the zonal winds of Saturn from this work. The black and red plot correspond to data from (Garcia-Melendo et al., 2011) where the black data was taken from images with CB2,CB3 filters (350-750 mbar) and the red data taken with MT2, MT3 filters (60-250 mbar). The green and blue data points refer to this work's results with MT3 and CB2 filter respectively.

The results presented from (Garcia-Melendo et al., 2011) in figure 5.3.1 come from measurements performed between September 2004 and January 2009 whereas our results range from May-September 2004 (green data) and March-April 2014 (blue data). Both results show consistency regarding the same filters independently of the time interval between them which for the CB

filters data is quite large ($\sim$ 5 years), supporting current theory that in the cloud level (350-750 mbar level) there's not much zonal wind speed variability despite the changing cronian season. The large difference on wind velocity near the equatorial region for CB and MT data sets (black and red) illustrates the effects of vertical wind shear (Garcia-Melendo et al., 2011), which is also captured by our own results.

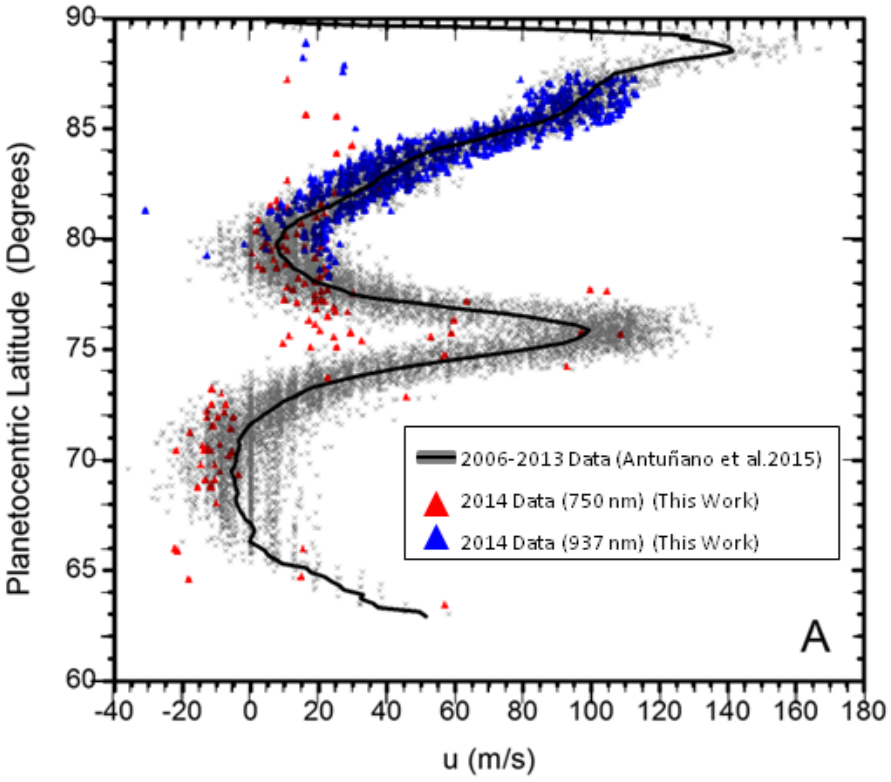

Figure 5.3.2: North polar region zonal winds of Saturn at cloud level. The grey data and black solid line are from (Antunano, A. et al., 2015) and red and blue data are from this work with different filters (red data at 750 nm while blue data at 937 nm). These are the same results as in figures 4.3.2 and 4.3.3.

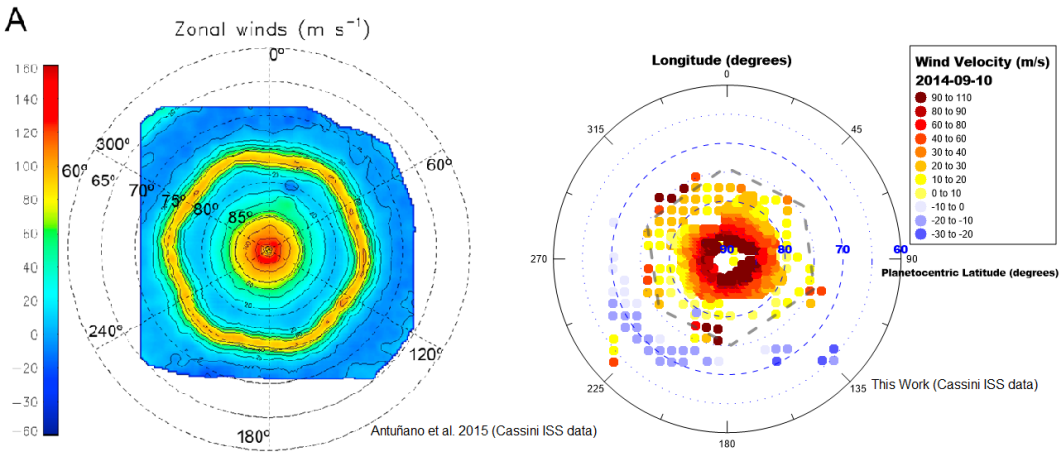

Figure 5.3.3: On the left, a contour polar plot of the zonal wind field on saturn's north polar region from (Antunano, A. et al., 2015) and on the right the results from this work, where results presented in figures 4.3.2 and 4.3.3 were grouped together. On the right plot, the outline represents an approximate location of the latitudinal region of the hexagon.

The black line in figure 5.3.2 is an average over the grey data points that were gathered in (Antunano, A. et al., 2015). For the purpose of this work, a complete view of the hexagon and its surroundings was only possible at great distances with the appropriate time interval between images to perform cloud tracking, hence the red data suffers from poor resolution which is showed by some deviation from (Antunano, A. et al., 2015) results. However, the blue data which was retrieved from an image pair with a close-up view of the north pole with greater resolution, shows that the majority of the data lies in good agreement with (Antunano, A. et al., 2015). The first velocity peak in this plot (close to 75°) corresponds to the strained clouds on the outline of the hexagon which rotates eastwards and has remained stable since it was discovered in 1980 by Voyager 1. The second peak relates to the powerful vortex in Saturn which also mirrors the south polar vortex velocity field (Antunano, A. et al., 2015). The same relations are also illustrated in figure 5.3.3 but it is clear that more data is needed for regions farther from the pole (hexagon and vicinity).

Chapter 6

Conclusions

By using PICV2, we were able to obtain results generally consistent with previous observations and models while also capable of capturing some degree of variability within the different atmospheric conditions on each target. Along with other tools from PLIA, the supervised correlation algorithm for cloud tracking is presently one of the best in the world. There is another algorithm which allows completely manual cloud tracking results and is producing promising results (just with ground-based measurements), which is a case for future work.

The detection and study of atmospheric gravity waves is a quite recent endeavour since high resolution images of planets' atmosphere are needed to fully observe and characterise the waves. With Venus Express data for Venus and Cassini data for Jupiter and Saturn there are still some difficulties in terms of image quality and resolution. This thesis is only a first step towards this field of research and as previously mentioned, there are still copious amounts of data to analyse for this matter which may lead to interesting results since the role of atmospheric waves on the dynamics of planets' atmospheres is not fully understood for most solar system objects.

Hyperspectral data like that of the VIRTIS instrument, has proven to be most useful since it allows cloud tracking to be performed in several layers of the atmosphere, giving us an almost 3D perspective of the atmosphere dynamics in Venus. Similar instruments like VIMS onboard Cassini also support, to some extent, this kind of sounding and future missions to various planetary targets will carry onboard instruments with heritage from VIRTIS on *Venus Express*. Cassini/ISS imaging also enabled us, through the use of different filters, to probe several layers of the atmosphere on the giants, even if to a lesser extent than with VIRTIS observations. Some of the cloud tracking results from this thesis will be refined for comparative studies with other techniques to study several layers of Saturn's upper atmosphere using Cassini/ISS data as well.

Ever since the SPICE training class in September 2016, I have invested some time learning more about this system, which will be a very useful tool for image navigation in the future. Though all basic lessons have been completed, and I'm acquainted with basic SPICE functionalities, there's always room for improvement and using this tool to navigate images from scratch, both for cloud tracking and atmospheric wave characterisation purposes is another exciting adventure which, on the long run, will help our planetary science group in many ways.

Bibliography

Alexander, M.J., Holton, J.R, On the spectrum of vertically propagating gravity waves generated by a transient heat source, European Geosciences Union, 2004.

Antunano, A., del Río-Gaztelurrutia, T., Sánchez-Lavega, A., Hueso, R., Dynamics of Saturn's polar regions, Journal of Geophysical Research: Planets, 10.1002/2014JE004709, 2015.

Archinal, B.A., Caplinger, M., Mars, the Meridian, and Mert: The Quest for Martian Longitude, American Geophysical Uniun, Fall Meeting 2002, 2002.

Atreya, S.K., Mahaffy, P.R., Niemann, H.B., Wong, M.H., Owen, T.C., Composition and origin of the atmosphere of Jupiter - an update, and implications for the extrasolar giant planets, Planetary and Space Science 51 105-112, 2003.

Atreya, S.K., Crida, A., Guillot, T., Lunine, J.I., Madhusudhan, N., Mousis, O., The Origin and Evolution of Saturn, with exoplanet perspective, to be published by Cambridge University Press, 2016.

Bougher, S., Hunten, D. and Philips, R., Upper Atmosphere Dynamics, Global Circulation and Gravity Waves, Venus II: Geology, Geophysics, Atmosphere, and Solar Wind Environment, University of Arizona Press, Tucson, AZ, Bougher S.W, Hunten D.M. and Phillips R.J., Eds., p. 259-291, 1997.

Belton, M.J.S., Klaasen, K.P., Clary, M.C., et al. The Galileo solid-state imaging experiment. Space Sci. Rev. 60, 413-455, 1992.

Cassini Spacecraft and instruments web page.
https://saturn.jpl.nasa.gov/mission/spacecraft/cassini-orbiter/

Cassini's Mission Fact Sheet.
https://www.jpl.nasa.gov/news/fact_sheets/cassini.pdf

Committe on Data Management and Computation, Space Science Board, Assembly of Mathematical and Physical Processes, National Research Council, Data Management and Coputation; Volume 1 - Issues and Recommendations, National Academy Press, 1982.

Drossart, P., Piccioni, G., Adriani, A., et al. Scientific goals for the observation of Venus by VIRTIS on ESA/Venus Express mission. Planet. Space Sci. 55, 1653-1672, 2007.

Esposito, L. W., Knollenberg, R., Marov, M., Toon, O. and Turco, R., The clouds and hazes of Venus, in Venus, edited by D.M. Hunten, L. Colin, T.M. Donahue, and V.I. Moroz, pp. 484-564, University of Arizona Press, Tucson, 1983.

Fox, J.L., Bougher, S.W, Structure, Luminosity and Dynamics of the Venus Thermosphere, Kluwer Academic Publishers, Space Science Reviews 55: 357-489, 1991.

Fletcher, L.N., Achterberg, R.K., Greathouse, T.K., Orton, G.S., Conrath, B.J., Simon-Miller, A.A., Teanby, N., Guerlet, S., Irwin, P.G.J, Flasar, F.M., Seasonal change on Saturn from Cassini/CIRS observations, 2004-2009, Icarus 208 337-352, 2010.

Fletcher, L.N., Irwin, P.G.J., Sinclair, J.A., Orton, G.S., Giles, R.S., Hurley, J., Gorius, N., Achterberg, R.K., Hesman, B.E., Bjoraker, G.L., Seasonal Evolution of Saturn's Polar Temperatures and Composition, arXiv:1412.6416v1, 2014.

Garate-Lopez, I., Hueso, R., Sanchez-Lavega, A., Peralta, J., Piccioni, G., Drossart, P., A chaotic long-lived vortex at the southern pole of Venus, Nature Geoscience 6, 254-25, 2013.

García-Melendo, E., Pérez-Hoyos, S., Sánchez-Lavega, A., Hueso, R., Saturn's zonal wind profile in 2004-2009 from Cassini ISS images and its long-term variability, Icarus 215, pg. 62-74, 2011.

Greenbelt Md., Kieffer, H., Proceedings of the Planetary Data Workshop, USGS Astrogeology Branch, NASA Conference Publication 2343 (Parts 1 and 2), 1983.

Grinspoon, D.H., Venus Revealed: A New Look Below the Clouds of Our Mysterious Twin Planet (Helix Books, Perseus Publishing, Cambridge, Massachusetts, 1997.

Guillot, T., A Comparison of the Interiors of Jupiter and Saturn, Nantes Symposium special issue, 1999.

Guillot, T., Gautier, D., Giant Planets, Treatise on Geophysics, 2nd edition 00 1-42, 2015

Hueso, R., Legarreta, J., Rojas, J.F., Peralta, J., Pérez-Hoyos, S., del Río-Gaztelurrutia, T., Sánchez-Lavega, A., The Planetary Laboratory for Image Analysis (PLIA), Advances in Space Research 46, 1120-1138, 2010.

Hueso, R., Peralta, J., Sánchez-Lavega, A., Assessing the long-term variability of Venus winds at cloud level from VIRTIS-Venus Express, Icarus 217, pg 585-598, 2012.

Hueso, R., Bandos, T.V., Garate-Lopez, I., Peralta, J., Sánchez-Lavega, A., Measurements of Venus winds from ultraviolet, visible and near infrared images with VIRTIS on Venus Express, International Venus Workshop, Catania, 12^{th} June 2013.

Irwin, P., Giant Planets of our Solar System - Atmospheres, Composition and Structure, Springer, Praxis Publishing - Second Edition, 2009.

Ingersoll, A., Dowling, T., Gierasch, P., Orton, G., Read, P., Sánchez-Lavega, A., Showman, A., Simon-Miller, A., Vasavada, A., Dynamics of Jupiter's Atmosphere, Cambridge University Press - 2004.

Khatuntsev, I.V., Patsaeva, M.V., Titov, D.V., Ignatiev, N.I., Turin, A.V., Limaye, S.S., Markiewicz, W.J., Almeida, M., Roatsch, Th., Moissl, R., Cloud level winds from Venus Express Monitoring Camera imaging, Icarus 226, pg. 140-158, 2013.

Knollenberg, R. G.; Hunten, D. M., The microphysics of the clouds of Venus - Results of the Pioneer Venus particle size spectrometer experiment, Journal of Geophysical Research, vol. 85, p. 8039-8058, 12/1980.

Knowles, B., Cassini Imaging Science Subsystem (ISS) Data User's Guide, Cassini Imaging Central Laboratory for Operations (CICLOPS), Space Science Institute, 2016.

Limaye, S.S., Jupiter: New estimates of the mean zonal flow at the cloud level, Icarus 65, pg. 335-352, 1986.

Limaye, S.S., Venus atmospheric circulation: Known and unknown, Journal of Geophysical Research, vol. 112, E04S09, 2007.

Luz, D. et al. Venus's Southern Polar Vortex Reveals Precessing Circulation, Science, volume 332, p. 577-580, 2011.

Machado, P., Dynamics of Venus' Atmosphere - Characterisation of its Global Circulation with Doppler velocimetry, Scholars' Press - 2013.

Machado, P., Widemann, T., Luz, D., Peralta, J., Wind circulation regimes at Venus' cloud tops: Ground-based Doppler velocimetry using CFHT/ESPaDOnS and comparison with simultaneous cloud tracking measurements using VEx/VIRTIS in February 2011, Icarus 243, pg. 249-263, 2014.

Markiewicz, W.J., Titov, D.V., Ignatiev, N., Keller, H.U., Crisp, D., Limaye, S.S., et al, Venus Monitoring Camera for Venus Express, Planetary and Space Science 55 1701-1711, 2007

Moissl, R., Khatuntsev, I., Limaye, S.S., Titov, D.V., Marikiewicz, W.J., Ignatiev, N.I., Roatsch, T., Matz, K.D., Jaumann, R., Almeida, M., Portyankina, G., Behnke, T., Hviid, S.F., Venus cloud top winds from tracking UV features in Venus Monitoring Camera images, Journal of Geophysical Research, vol. 114, E00B31, 2009.

Moses, J., Bézard, B., Lellouch, E., Gladstone, G.R., Feuchtgruber, H., Allen, M., Photochemistry of Saturn's Atmosphere. I. Hydrocarbon Chemistry and Comparisons with ISO Observations, Icarus, Volume 143, Issue 2, pp. 244-298 - 2000.

Ortiz, J. L., G. S. Orton, A. J. Friedson, S. T. Stewart, B. M. Fisher, and J. R. Spencer, Evolution and persistence of 5-μm hotspots at the Galileo probe entry latitude, J. Geophys. Res, 1998.

Parisi, M., Galanti, E., Finocchiaro, S., Iess, L., Kaspi, Y., Probing the depth of Jupiter's Great Red Spot with Juno gravity experiment – Icarus 267 (2016), 232-242 - Elsevier, 2015.

Pater, I., Lissauer, J., Planetary Sciences, Cambridge University Press - 2007.

Peralta, J., Hueso, R., Sánchez-Lavega, A., A reanalysis of Venus winds at two cloud levels from Galileo SSI images, Icarus 190, pg 469-477, 2007.

Peralta, J., Vientos, Turbulencia y Ondas en las Nubes de Venus, PhD Thesis, Departamento de Fisica Aplicada I, Universidad del Pais Vasco - Euskal Herriko Unibertsitatea, 2008.

Peralta, J., Hueso, R., Sánchez-Lavega, A., Piccioni, G., Lanciano, O., Drossart, P., Characterization of mesoscale gravity waves in the upper and lower clouds of Venus from VEX-VIRTIS images, Journal of Geophysical Research, vol. 113, 2008.

Piccialli, A., Titov, D.V., Sanchez-Lavega, A., Peralta, J., Shalygina, O., Markiewicz, W.J., Svedhem, H., High latitude gravity waves at the Venus cloud tops as observed by the Venus Monitoring Camera on board Venus Express, Icarus 227 94-111, 2014.

Poincaré, H., Sur la precession des corps deformables, Bull. Astron. 20, 321-356, 1910.

Porco, C., West, R.A., McEwen, A., Del Genio, A.D., Ingersoll, A.P., Thomas, P., Squyres, S., Dones, I., Murray, C.D., Johnson, T.V., Burns, J.A., Brahic, A., Neukum, G., Veverka, J., Barbara, J.M., Denk, T., Evans, M., Ferrier, J.J., Geissler, P., Helfenstein, P., Roatsch, T., Throop, H., Tiscareno, M., Vasavada, A.R., Cassini imaging science of Jupiter's atmosphere, satellites, and rings, Science 299, pg. 1541-1547, 2003.

Porco, C.C., West, R.A., Squires, S., et al. Cassini imaging science: instrument characteristics and anticipated scientific investigations at Saturn. Space Sci. Rev. 115, 363-497, 2004.

Rybicki, G.B., Lightman, A.P., Radiative Processes in Astrophysics, Wiley-VCH, 2004.

Gonçalves, R., Dynamics of Venus' Atmosphere: wind characterization with Doppler velocimetry (Master's Thesis - Physics Department, Faculty of Sciences of the University of Lisbon - 2016)

Sánchez-Lavega, A., Hueso, R., Piccioni, G., Drossart, P., Peralta, J., Pérez-Hoyos, S., Wilson, C.F., Taylor, F.W., Baines, K.H., Luz, D., Erard, D., Lebonnois, S., Variable winds on Venus mapped in three dimensions, Geophysical research letters, vol. 35, L13204, 2008.

Sanchez-Lavega, A., An introduction to Planetary Atmospheres, CRC Press, Taylor and Francis, 2011.

Sayanagi, K.M., Baines, K.H., Dyudina, U.A., Fletcher, L.N., Sánchez-Lavega, A., West, R.A., Saturn's Polar Atmosphere, arXiv:1609.09626v2, 2016.

Seiff, A., Kirk, D.B., Knight, T., Young, R., Mihalov, J., Young, L., Milos, F., Schubert, G., Blanchard, R., Atkinson, D., Thermal structure of Jupiter's atmosphere near the edge of a 5-*mu*m hot spot in the north equatorial belt, Journal of Geophysical Research, Volume 103, Issue E10, p. 22857-22890, 1998.

Simon-Miller, A.A., Gierasch, P.J., Beebe, R.F., Conrath, B., Flasar, F.M, Achterberg, R.K., Cassini CIRS Team, New observational results concerning Jupiter's Great Red Spot, Icarus 158, pg.249-266, 2002.

Svedhem, H.; Titov, D.; Taylor, F.; Witasse O., Venus as a more Earth-like planet, *Nature*, volume 450, p. 629-632, 2007.

Taylor, F., McCleese, D., Elson, L., Martonchik, J., Diner, D., Houghton, J., Delderfield, J., Schofield, J., Bradley, S., Infrared remote sensing of the atmosphere of Venus from the Pioneer 12 Orbiter, Space research. Volume 20 - Proceedings of the Open Meetings of the Working Groups on Physical Sciences, Bangalore, India, May 29-June 9, 1979. Oxford and Elmsford, N.Y., Pergamon Press, p. 227-230, 1980.

Terrile, R. J. and J. A. Westphal, The vertical cloud structure of Jupiter from 5 μm measurements, Icarus 30, 274-281, 1977.

Vasavada, A.R., Ingersoll, A.P., et al, Galileo Imaging of Jupiter's Atmosphere: The Great Red Spot, Equatorial Region, and White Ovals, Icarus 135, pg. 265-275, 1998.

Vidmachenko, A.P., Seasons on Saturn. 1. Changes in reflecting characteristics of the atmosphere at 1964-2012, Astronomical School's Report, ISSN 1607-2855, Vol. 11, No.1, 2015.

Vidmachenko, A.P., Seasons on Saturn. II. Influence of solar activity on variation of methane absorption, Astronomical School's Report, ISSN 1607-2855, Vol. 11, No.1, 2015.

Yelle, R.V., Miller, S., Jupiter's Thermosphere and Ionosphere, Cambridge University Press - 2004.

Chapter 7

Appendix

7.1 Instrument Specific Parameters

7.1.1 Cassini - ISS

Filter	Numerical Name (NAC)	Numerical Name (WAC)	Science Justification
UV1	258W	-	Aerosols
UV2	298W	-	Aerosols, broad-band color
UV3	338W	-	Aerosols, broad-band color, polarization
VIO	-	420SP	Broad-band color
BL2	440W	-	Medium-band color, polarization
BL1	451W	460W	Broad-band color
GRN	568W	567W	Broad-band color
MT1	619N	-	Methane band, vertical sounding
CB1	635N	-	Two-lobed continuum for MT1
RED	650W	648W	Broad-band color
HAL	656N	656W	H-α/lightning
MT2	727N	-	Methane band, vertical sounding
CB2	750N	752N	Continuum for MT2
IR1	752W	742W	Broad-band color
IR2	862W	853W	Broad-band color, ring absorption band
MT3	889N	890N	Methane band, vertical sounding
CB3	938N	939N	Continuum for MT3, see through Titan haze
IR3	930W	918W	Broad-band color
IR4	1002LP	1001LP	Broad-band color
IR5	-	1028LP	Broad-band color
CL1	611W	635W	High sensivity, combine with filter wheel 2 filters
CL2	611W	635W	High sensivity, combine with filter wheel 1 filters
P0	617W	-	Visible polarization, 0 deg
P60	617W	-	Visible polarization, 60 deg
P120	617W	-	Visible polarization, 120 deg
IRP0	-	705W	IR polarization, 0 deg; see through Titan haze
IRP90	-	705W	IR polarization, 90 deg; see through Titan haze

Table 7.1: ISS filter names and their science justification. From (Knowles, B., 2016).

Camera	Filter 1	Filter 2	Central Wavelength (nm)	Bandpass FWHM (nm)	Effective Wavelenght (nm)
NAC	CL1	CL2	610.675	340.056	651.057
NAC	CL1	GRN	568.134	113.019	569.236
NAC	CL1	UV3	338.284	68.0616	343.136
NAC	CL1	BL2	439.923	29.4692	440.980
NAC	CL1	MT2	727.421	4.11240	727.415
NAC	CL1	CB2	750.505	10.0129	750.495
NAC	CL1	MT3	889.194	10.4720	889.196
NAC	CL1	CB3	937.964	9.54761	937.928
NAC	CL1	MT1	618.945	3.68940	618.949
NAC	CL1	CB1	619.381	9.99526	619.292
NAC	CL1	IR3	929.763	66.9995	928.304
NAC	CL1	IR1	751.894	152.929	750.048
NAC	RED	CL2	650.086	149.998	648.879
NAC	RED	GRN	601.032	51.9801	600.959
NAC	RED	MT2	726.633	2.33906	726.624
NAC	RED	CB2	744.255	4.22393	743.912
NAC	RED	MT1	618.911	3.69858	618.922
NAC	RED	CB1	619.568	9.07488	619.481
NAC	RED	IR3	695.435	2.04887	695.040
NAC	RED	IR1	701.900	44.9603	701.692
NAC	BL1	CL2	450.851	102.996	455.471
NAC	BL1	GRN	497.445	5.00811	497.435
NAC	BL1	UV3	386.571	14.0295	389.220
NAC	BL1	BL2	440.035	29.6733	441.077
NAC	UV2	CL2	297.880	59.9535	306.477
NAC	UV2	UV3	315.623	28.9282	317.607
NAC	UV1	CL2	258.098	37.9542	266.321
NAC	UV1	UV3	350.697	9.07263	353.878
NAC	HAL	CL2	655.663	9.26470	655.621
NAC	HAL	GRN	648.028	5.58862	647.808
NAC	HAL	CB1	650.567	2.73589	650.466
NAC	HAL	IR1	663.476	5.25757	663.431
NAC	IR4	CL2	1002.40	35.9966	1001.91
NAC	IR4	IR3	996.723	36.0700	996.460
NAC	IR2	CL2	861.962	97.0431	861.066
NAC	IR2	MT3	889.176	10.4655	889.176
NAC	IR2	CB3	933.657	3.71709	933.593
NAC	IR2	IR3	901.843	44.0356	901.630
NAC	IR2	IR1	827.438	28.0430	827.331
WAC	CL1	CL2	634.928	285.999	633.817
WAC	CL1	RED	648.422	150.025	647.239
WAC	CL1	GRN	567.126	123.999	568.214
WAC	CL1	BL1	460.418	62.2554	462.865
WAC	CL1	VIO	419.684	18.1825	419.822
WAC	CL1	HAL	656.401	9.96150	656.386
WAC	CL1	IR1	741.456	99.9735	739.826
WAC	IR3	CL2	917.841	45.3074	916.727
WAC	IR3	RED	690.604	3.04414	689.959
WAC	IR3	IR1	790.007	3.02556	783.722
WAC	IR4	CL2	1002.36	25.5330	1001.88
WAC	IR5	CL2	1034.49	19.4577	1033.87
WAC	CB3	CL2	938.532	9.95298	938.445
WAC	MT3	CL2	890.340	10.0116	890.332
WAC	CB2	CL2	752.364	10.0044	752.354
WAC	CB2	RED	747.602	4.07656	747.317
WAC	CB2	IR1	752.324	10.0026	752.314
WAC	MT2	CL2	728.452	4.00903	728.418
WAC	MT2	RED	727.517	2.05059	727.507
WAC	MT2	IR1	728.293	4.00906	728.284
WAC	IR2	CL2	853.258	54.8544	852.448
WAC	IR2	IR1	826.348	26.0795	826.255

Table 7.2: ISS filter bandpasses, with combinations used in observations. Effective wavelength is the central wavelength of the bandpass convolved with the solar spectrum. All values were derived from ground-based measurements of the CCD quantum efficiency and filter and optics transmission curves. From (Knowles, B., 2016).